A Study on High-Speed-Vision-Based Visible Light Communication System for Real-Time Video Streaming

(リアルタイムビデオストリーミングのための高速ビジョンベースの可視光通信システムに関する研究)

by

Atul Kumar Sharma

Graduate School of Engineering
Hiroshima University

October, 2021

Contents

List of Figures

List of Tables

Chapter 1

Introduction

Visible light communication (VLC) is becoming an alternative choice for next-generation wireless technology by offering low cost, unregulated bandwidth and ubiquitous infrastructures support. This technology is envisioned to be used in a wide range of applications both indoor as well as outdoor. This work investigates in detail, designs of an HFR projector-camera-based visible light communication (VLC) system for real-time broadband video streaming and a visual feedback-based synchronization algorithm which can be useful in applications such as VLC systems, autonomous vehicles, and surveillance applications. This chapter gives detail of motivation, objectives and original contributions. The thesis organization is presented at the end of the chapter.

1.1 Background

With the recent rapid advances in computer and image sensor technologies, many high frame rate (HFR) vision systems that can capture and process images simultaneously at thousands of frame per second have been developed [1–5]; many tracking algorithms, such as optical flow estimation [6, 7], cam-shift tracking [8], and feature-point tracking [9], have been accelerated by the parallel implementation of these algorithms on field programmable gate array (FPGA) and graphics processing unit. These HFR vision systems can have a large bandwidth that can simultaneously recognize high-speed phenomena, which are too fast to be recognized by the naked human eyes and standard video cameras operating at dozens of frames per second. Many vision-based dynamic sensing systems have been developed for the human-invisible dynamics of objects such as drone tracking [10, 11], motion-blur-free video shooting [12–15], vibration analysis [16, 17], and microscopic sensing [18–21]. In addition to these HFR vision systems that can capture the dynamic phenomena vibrating at hundreds or thousands of hertz, HFR projector systems based on the digital micro-mirror device (DMD) technology [22, 23] can project binary image patterns at thousands of frames per second or more; several types of HFR projector-camera systems [24–26] have been reported in various applications, such as structured light based 3D sensing [27–30] and simultaneous projection mapping [31–34]. If a real-time HFR vision system could function as a communication receiver to perfectly capture and encode the HFR-blinking high-space-resolution image patterns with real-time video processing at thousands of frames per second, which are too fast for human eyes to see, high-thorough visible light communication (VLC) could be realized for broadband video streaming by utilizing the high-resolution in mega-pixel order and high-frequency band in the kHz order in the HFR projection of an HFR projector.

1.2 Motivation and Research Objective

Development of VLC systems has numerous advantageous over RF system such as:

- Provides secured communication system.
- It supports larger bandwidth.
- Harmless for humans and other electronic devices
- Easy to integrate into the existing lighting infrastructure.
- It has low power consumption adn is used for both commuincation and illumination.
- Low modulation bandwidth of LEDs.
- Existing projectors are also a potential source of VLC system.
- Low cost installation (LEDs and photodiode).

However, there are several challenges hindering the development of VLC systems, and these challenges include:

- Low bandwidth of LEDs.
- Interference issues.
- Short coverage range.
- Challenges to integrate VLc system with wifi system.
- No communication if not in sight of light source.
- Beam dispersion.

The primary objective of this work was to stream a real time video using the VLC system. Figure 1.1 shows the conventional VLC systems used for communication where the simplest VLC system comprises a LED lamp and a photodiode. It has an advantage of high-speed data transmission but the interference of VLC signals from multiple LED lamps occurs as its disadvantage. To solve the interference problem, an image sensor is used as a receiver in such a VLC system. The LED lamp also has the disadvantage that it requires an array of LEDs to be used for sending more data which can be overcome by using projectors. The projectors can embed different data for each pixel and modulate the VLC signal giving an advantage over the LEDs array. The overall bandwidth of the VLC system can be increased if a high frame rate camera is used as a receiver and a high frame rate projector is used as a transmitter.

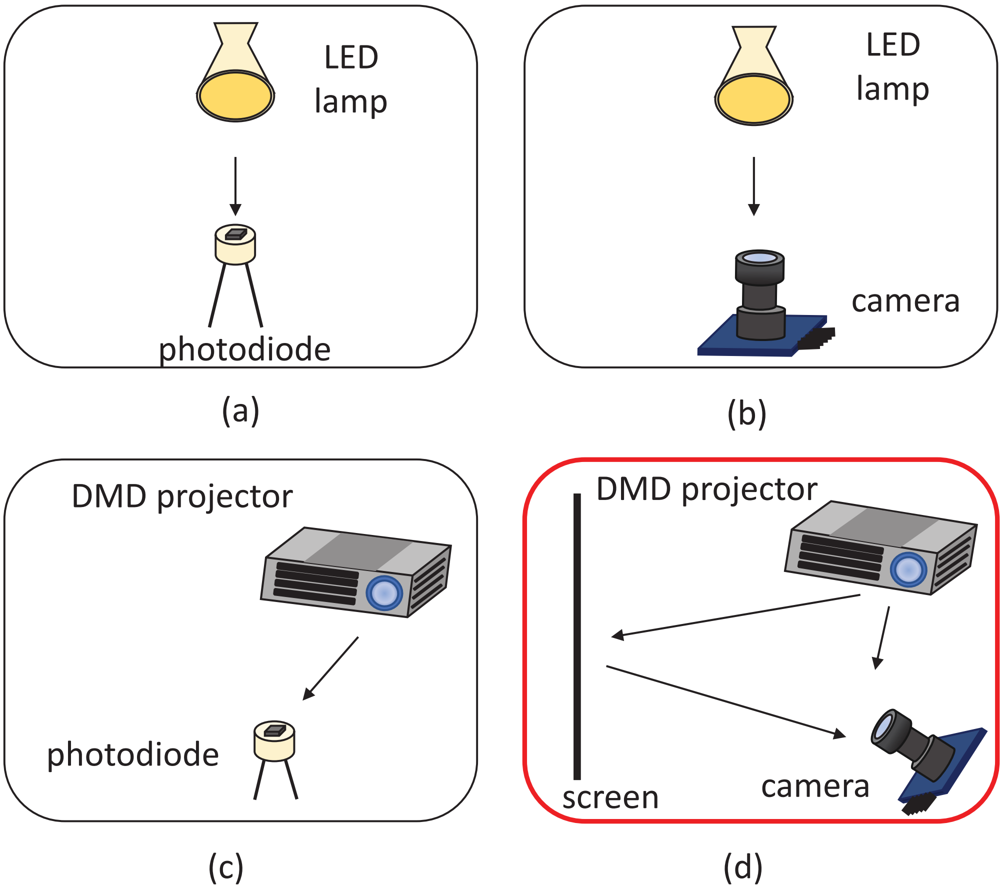

Figure 1.1: Types of transmitter and receiver used in a VLC system.

1.3 Research Contribution

In order to address the above-mentioned challenges and problems, novel advanced system architecture, interference mitigation scheme, resource management approach and robust design are explored and presented in this thesis. The major contributions of the thesis are summarized as follows

- This thesis first proposes an HFR-projector-camera-based VLC system for broadband video streaming, in which a projector and vision system function as an image transmitter and image receiver operating at thousands of frames per second, respectively. We implemented video encoding and decoding processes based on a camera-projector-based VLC protocol for real-time video streaming so that the pixel-wise high-throughput light patterns projected from the HFR projector can be maximally utilized without losing any information when the spatial resolution of the HFR vision system is similar to that of the projector.

- Designed, investigated and evaluated a novel method for synchronizing a high frame-rate (HFR) camera with an HFR projector using a visual feedback-based synchronization algorithm for streaming video sequences in real time on a visible-light communication (VLC)-based system. The frame rates of the camera and projector are equal, and their phases are synchronized. A visual feedback-based synchronization algorithm is used to mitigate the complexities and stabilization issues of wire-based triggering for long-distance systems.

1.4 Outline of Thesis

This thesis comprises of six chapters which is organized as follows:

In Chapter 1, briefly introduces the background, challenges and motivations of VLC based real time video streaming, and the summary of the major contributions is provided in this chapter, too.

In Chapter 2, summarizes the related works of VLC along with the problems in the conventional vision-based VLC system for broadband video streaming

In Chapter 3, the concept of the HFR-projector-camera-based VLC system are explained along with a description.

In Chapter 4, detailed explanation of the visual feedback-based synchronization algorithm is described in this chapter.

In Chapter 5,provides an evaluation of the performance of the synchronized system via experiments in real time at 60 fps with the HFR projector and camera.

Finally, Chapter 6, concludes the contributions of this study and discusses the futuristic improvements to achieve more robust results as well as the real-time implementation of video stabilization and mosaicking in various applications of the real-world.

Chapter 2

Related Works

2.1 Projector-based VLC applications

VLC has emerged as an alternative technique to accommodate the exponentially increasing demands of radio frequency-based wireless communication [35–38]. The visible light corresponds to a band of frequencies ranging between 400THz (750nm) and 800THz (375nm) and is used as a source in VLC systems for transmitting encoded information using air as a transporting medium and decoded using an appropriate photoreceiver. The intensity of the light source is modulated according to the input data at a high rate which is faster than the persistence of human vision. However, a sensitive photodiode or an image sensor is used to detect the embedded information by decoding the on-off behavior of the light emitting diode (LED) [39–44]. In a VLC system, the image sensor has an advantage over the photodiode; it can separate information spatially and temporally from the light source, whereas the photodiode-based systems are highly sensitive to light and inexpensive, but require additional equipment for setting up a system. With the ability of image sensors to capture light, a new type of optical wireless communication is introduced known as camera communication, where image sensors are used for sensing the light intensity emitted from a light source [45, 46]. Many potential applications of camera-based VLC systems include automotive systems [47–49], mobile phone-camera communications [50–52], indoor wireless communications [53–55], LED camera-based

VLC [56, 57], and image recognition and light signaling [58].

Image-sensors-based VLC systems have been developed to decode the information transmitted from different light sources, such as LEDs, display screens, and projectors. Various studies contributing to LED-camera based communication systems have been conducted, focusing on the rate of data transfer from the LED-to-camera and LED-based position location detection systems [59–63]. In addition, traffic signal LEDs are used for estimating the position of a vehicle using an in-vehicle camera and an LED-based VLC system [64–67]. The accuracy of LED-based systems depends on the number of LEDs used, focal length of the lens, pixel size, and frame rate of the camera receiver. To avoid the complexity of building an LED source circuit for transmission, a display screen or projector has been used as an alternative solution to increase the bit-rate transfer and overall speed of indoor-based VLC systems [68–71]. Display monitors and LCD panels modulate the screen intensities using different encoding techniques and are accordingly decoded using a camera at the receiver [72–75]. The data communication between a screen and a camera does not necessarily depend on the content of the screen, and it can be completely hidden from the user by integrating the information and content onto the screen, which further limits their application scenarios. The display screens and projectors with low frame rates make the communication systems slower and limited; this issue can be resolved by using HFR projectors that provide a high data transmission rate, in contrast to commercial projectors that support low frame rate projection and lack the controlling parameters.

2.2 Camera-based VLC applications

The major drawback of conventional cameras and the cameras integrated in smartphones and tablets is that they all operate at a low frame rate due to which the communication bandwidth of VLC systems becomes low, which can be overcome by using an HFR camera. Therefore, we propose a VLC system with an HFR projector and HFR camera that can provide a higher communication bandwidth and better performance, as well as minimize the loss of information. This research mainly focuses on the spatio-temporal information which is similar to transmitting spatial information such as quick response codes (QR codes) and bar-codes; however, for transmitting the temporal information, LED-to-camera communication is considered, which decodes the data temporally. The processing of data in real time involves challenges, and, hence, additional information is embedded with transmitted video sequences for proper decoding at the receiver side. Thus, the spatio-temporal information is transmitted using an HFR projector which is then decoded spatially and temporally by an HFR camera that can be used in our system for transmitting real-time videos using VLC.

Because camera synchronization is crucial to some applications, there are some in which the interpolation and prediction of the frames of unsynchronized cameras are used to synchronize the camera [76]. Alleviation of synchronization between the projector and camera can be achieved by using wired external triggers; however, in some applications, there is a need for synchronization without an external trigger, such as in a VLC system. Many industrial cameras are equipped with external trigger-signal ports in which the long wires may cause unstable synchronization owing to the distance between the projector and camera, whereas short wires may obtrude the constraints of spatial camera configurations. To mitigate these problems, some wireless synchronization applications have been used to display pattern sequences. Correspondingly, the camera achieves synchronization by adjusting its exposure time [77]. There have been studies in which geometric points were used for synchronization, but these require a sufficient number of corresponding points across images to carry out simultaneous geometric calibration and synchronization [78–81]. In some studies [82] and [83], existing wired standard buses (e.g., IEEE1394 and Ethernet) were used to send trigger signals to the camera for synchronization. Time synchronization is another method that uses Wi-Fi, with which the master subsystem provides connectivity and records video, while the slave subsystem provides low-power event detection via ZigBee connectivity [84]. In this system, a Wi-Fi mesh network is used to transmit video data, and a ZigBee network is used to define the network topology and synchronize multiple surveillance-camera systems. In [85], synchronization was achieved in two stages. During the first stage, the phones were synchronized to the clock of a leader device using the network time protocol (NTP); during the second stage, all client phone cameras captured a continuous stream that was phase-shifted to achieve better accuracy. The prominent drawback of wireless time synchronization is the nondeterminism of media access time [86]. Another study involved illumination-based intensity-modulated synchronization using a 1,000-fps camera with a phase-locked loop algorithm [87]. This algorithm is robust to background light and locks-in a high camera frame rate to the LED by adjusting the gain parameter to fit the brightness. However, all systems involving camera clock controls using visual feedback require an LED as the light source, or they must be controlled using a wire triggering device or NTP. The wired synchronization system has a higher accuracy, but it is unsuitable for an optical wireless communication system.

Chapter 3

HFR projector-camera-based VLC system

3.1 Concept of proposed VLC system

This study introduces an HFR-projector-camera-based system for streaming videos in real time using VLC. An overall block diagram of the proposed VLC system is shown in Figure 3.2, where an HFR projector can project the encoded stored color video sequences or universal serial bus (USB) camera videos into binary-modulated images that can be decoded using a monochrome HFR camera. To decode binary-modulated images effectively, additional information is appended to each binary image as a header block that contains the current image information such as the frame number, starting of a new image, and channel bit plane information. In addition, the system can eliminate any ambiguities associated with mismatched pixel alignment along the gradient between the HFR projector and HFR camera using gray-code encoding instead of pure-binary-code-based image projection. At the receiver, the frame rate of the monochrome HFR camera is set to be thrice that of the HFR projector considering the Nyquist sampling rate so that the original projected image can be retrieved without any loss. The monochrome HFR camera captures the binary images to reconstruct the original image and background subtraction is performed for every captured binary image to make the system more robust against different textured backgrounds. In addition, the content of the cumulatively projected HFR binary images is imperceptible to human eyes, which results in secure data transmission.

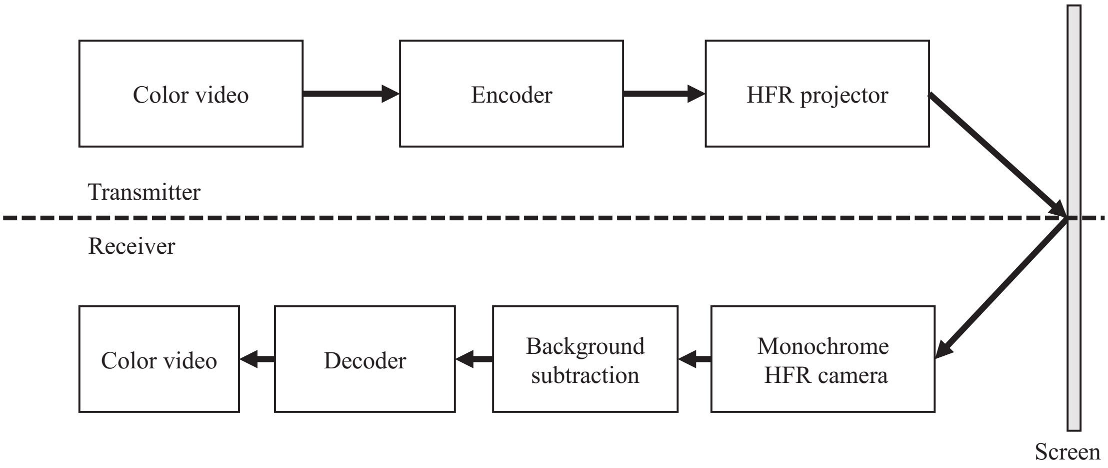

Figure 3.1

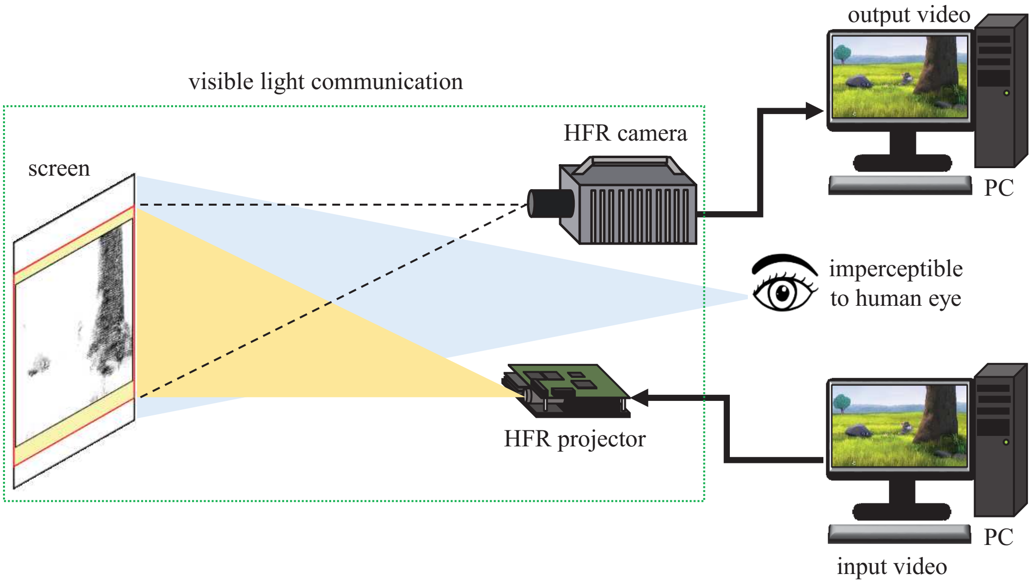

Figure 3.2: (a) Block diagram and (b) configuration of the proposed VLC system.

3.2 System Configuration

To transmit information in the visible range and establish a high-speed VLC communication, an HFR projector with the desired controlling parameters and high projection rate is required. This is achieved by using a digital light processing (DLP) LightCrafter 4500 HFR projector that provides a high projection rate of up to 4,000 fps. DLP LightCrafter 4500 is a projection system with a two-dimensional array of electrically addressable and mechanically tiltable micro-mirrors to represent each pixel, known as digital mirror devices (DMDs) that are widely used in consumer electronics [88–90]. The DLP projector does not modulate the emitted wavelength of the projected light to reproduce the color intensity instead it reproduces by modulating the exposure time of the mirrors over a specific operating refresh time based on the projected frame bit planes. This projector supports 1-bit to 8-bit images with a resolution of 912×1,140, and each pixel corresponds to a micro-mirror on the DMD. This feature helps in projecting data at the pixel level and transforms the image to be used for pixel-wise binary projection for the VLC system.

Dynamic changes related to HFR projection are imperceptible to human eyes and conventional cameras are unable to detect high-speed data or events. Therefore, to monitor high-speed phenomena continuously, we need HFR cameras to improve the shooting speed and performance. In this study, the proposed system consists of a monochrome HFR camera system that is an extension of Fastcam SA-X2 developed by Co. Photron and Hiroshima University; it provides a complementary metal oxide semiconductor (CMOS) sensor-based super high-speed vision platform that enables real-time image processing more than 10,000 fps against a megapixel image and global electronic shutter with excellent light sensitivity [4]. This camera is used as a receiver with an embedded external board that has an onboard FPGA for image processing; it produces output images with a resolution of 512×512 with a 12-bit dynamic range at 3,125 fps in real time. This HFR camera system provides high frame rate image capturing to meet the requirements of the proposed VLC system.

3.3 Transmitter Encoding System

The transmitter encoding system in the proposed VLC system has three stages: encoding image from pure-binary-code into gray-code, addition of header information and binary image or bit-plane projection, as shown in Figure 3.3. The input RGB video is initially encoded frame-by-frame into gray-code from a pure-binary-code, and additional information, such as the frame number, along with other necessary information, is appended to the current image in the form of header information, which is then fed to the HFR projector, where it is deconstructed into binary images for projection.

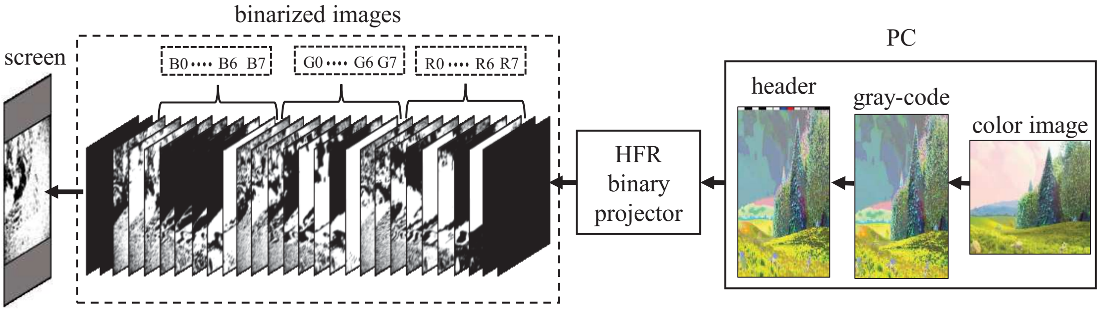

Figure 3.3: Transmitter.

3.3.1 Header Information

To decode the image and establish a communication link between the transmitter and receiver, additional information about the image is appended to the image in the form of blocks of pixels as header information. In the header, four blocks of pixels represent information about the current image, as shown in Figure 3.4, where the first block *S0*, whose all pixel values are set to a maximum value of 255 for an 8-bit pixel, is used for determining the start of a new image and software-based synchronization. The next five blocks of pixels (that is *F4, F3, F2, F1,* and *F0*) in the header represent a 5-bit frame number ranging from 0 to 31 which is assigned to each frame continuously. Thereafter 2-bit channel information is added using the *C1* and *C0* blocks to represent the red, green and blue channels of an image, whereas the last 3-bits (that is *B2, B1,* and *B0*) represent eight bit-planes of a single channel that will be used to determine any loss in the bit-plane in an RGB channel of the image. The last five blocks of pixels help in determining the sequence of binary images for reconstructing an image. Therefore, let $I_t(x, y)$ be the input image, which is combined with the header information of size $I_h(w, y)$ to form a combined image, $I_{rgb}(m, n)$, before passing it to the HFR projector for binary image projection, as expressed in Equation (3.1).

$$I_{rgb}(m, n) = I_t(x, y) + I_h(w, y) \tag{3.1}$$

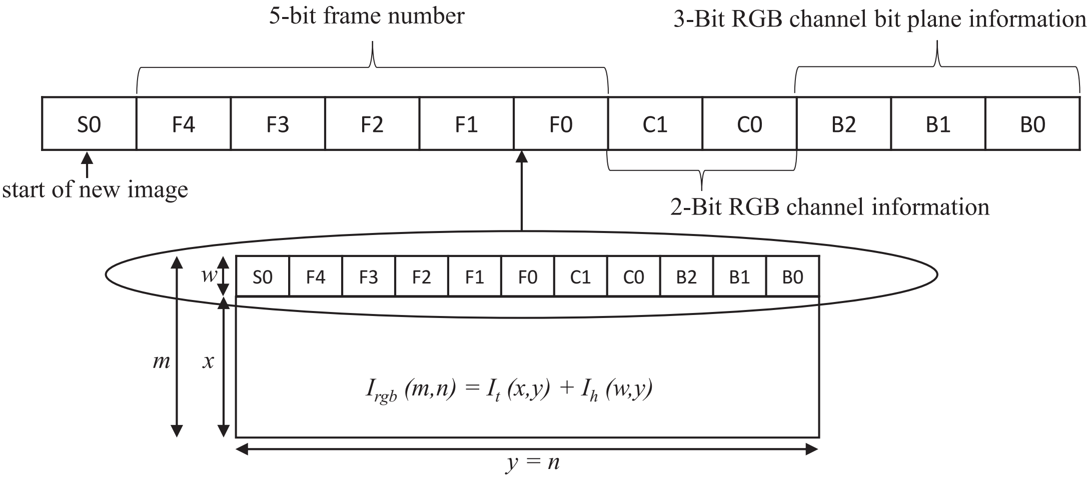
5-bit frame number
3-Bit RGB channel bit plane information
S0
F4
F3
F2
F1
F0
C1
C0
B2
B1
B0
start of new image
2-Bit RGB channel information
w
m
x
I_{rgb} (m,n) = I_t (x,y) + I_h (w,y)
y = n

Figure 3.4: Header information.

3.3.2 Projection Pattern

The spatio-temporal projection of binary images by an HFR projector is achieved by decomposing a given packed 24-bit RGB image into its equivalent twenty-four 1-bit binary images. The HFR projector supports $2^8 = 256$ intensity levels for an 8-bit channel and the decomposition of a 24-bit RGB color image is demonstrated in Figure 3.5, where $I_{rgb}(m, n)$ is a three-channel 24-bit color image that is split into three single-channel 8-bit images, $I_r(m, n)$, $I_g(m, n)$ and $I_b(m, n)$. The 8-bit single-channel image is converted into binary images by the HFR projector as eight 1-bit images, where $Br_t(m, n)$, $Bg_t(m, n)$ and $Bb_t(m, n)$ represents the t^{th} 1-bit image of the red, green, and blue channels, respectively; ”t” represents the bit-plane number ranging between 0 and 7 for an 8-bit

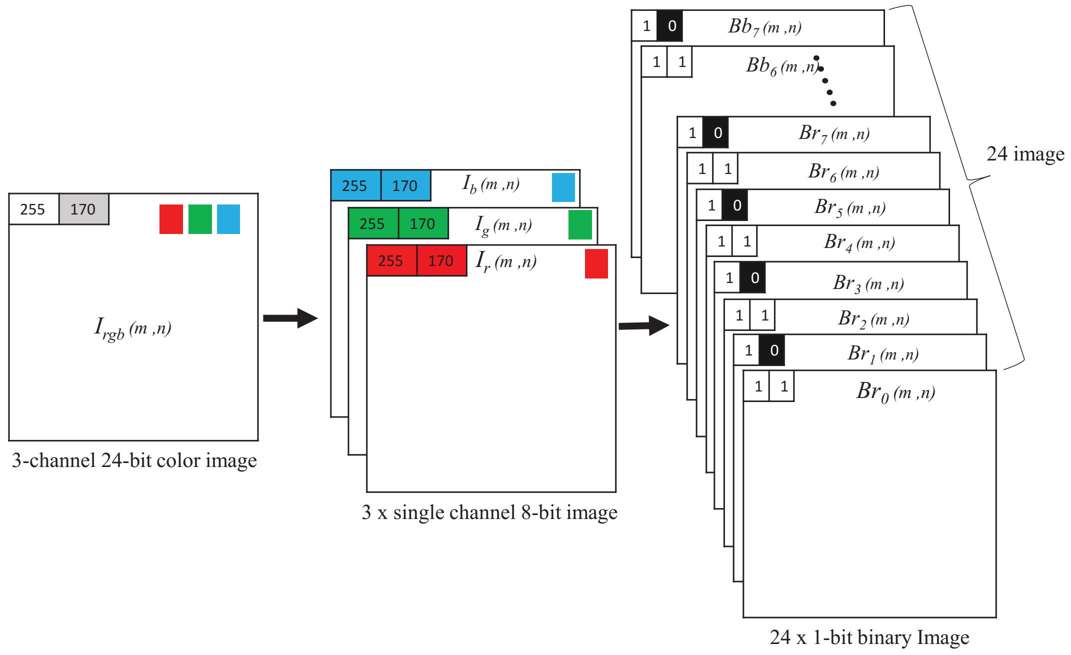

Figure 3.5

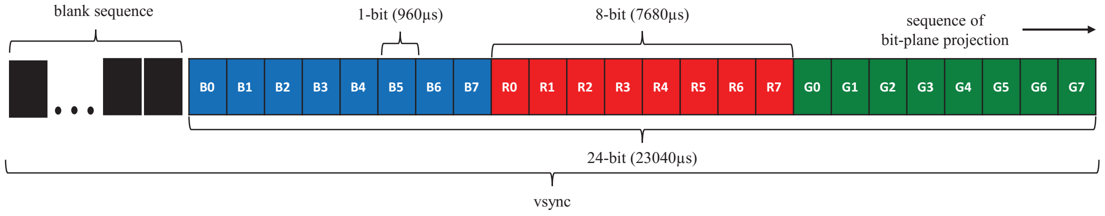

Figure 3.6

Figure 3.7: (a) Decomposition of an RGB image into binary bit-plane images and (b) bit-plane projection pattern for a single RGB image.

image. The projection sequence of binary images is defined by the users in the HFR projector controlling software, and the projection of a new image is triggered by vertical synchronization (*vsync*) signals. The pattern sequence for binary image projection is shown in Figure 3.6, where the total duration of exposure for all patterns should be less than or equal to the *vsync* duration. The HFR projector introduces a sequence of blank images when the duration of all projection patterns is not equal to *vsync*.

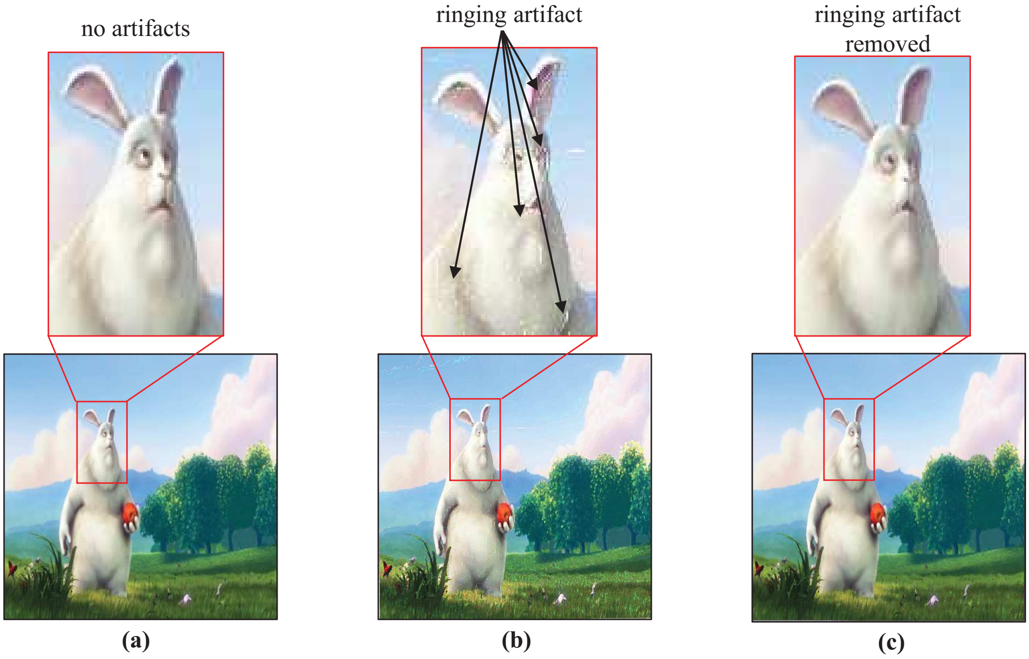

Figure 3.8: (a) Original image, (b) reconstructed image with pure-binary-code, (c) reconstructed image with gray-code.

3.3.3 Gray-Code Encoding

The image reconstructed with pure-binary-code has ambiguities along the gradients due to mismatched pixel alignment between the HFR projector and HFR camera which can be overcome by gray-code-based projection. The ambiguities observed in the images reconstructed using pure-binary-code includes ringing artifacts as shown in Figure 3.8, which can be reduced by gray-code-based image projection. Let $I_t(x,y)$ be the input RGB color image having three 8-bit channels as red $I_r(x,y)$, green $I_g(x,y)$ and blue $I_b(x,y)$ channel as expressed in Equation (3.2).

$$I_t(x,y) = \begin{bmatrix} I_r(x,y) \\ I_g(x,y) \\ I_b(x,y) \end{bmatrix}, \tag{3.2}$$

The pixel-value P of an input image can be represented by a sequence of binary values (b_{n-1}, ..., b_1, b_0) based on Equation (3.3). In an 8-bit image, each pixel is represented as eight 1-bit binary images where the higher bit-planes contain more significant visual information and the lower bit-plane shows more details. Using Equation (3.4), the gray-code representation of a binary pixel value P, is (g_{n-1}, ..., g_1, g_0), which is used to convert the pure-binary-code images of red $I_r(x, y)$, green $I_g(x, y)$, and blue $I_b(x, y)$ channels into gray-code as $I_{gray_r}(x, y)$, $I_{gray_g}(x, y)$, and $I_{gray_b}(x, y)$, respectively which are combined to make one 24-bit gray-code color image, $I_{gray_t}(x, y)$, as shown in Equation (3.5). The gray-code image $I_{gray_t}(x, y)$ is then combined with the header information $I_h(w, y)$, to form $I_{gray_{rgb}}(m, n)$, as shown in Equation (3.6), for transmission through the HFR projector as binary images.

$$P = \sum_{i=0}^{n-1} b_i 2^i = b_0 2^0 + b_1 2^1 + ... + b_{n-1} 2^{n-1} \ , \tag{3.3}$$

$$g_i = \begin{cases} b_i & i = n\text{-}1 \\ b_i \oplus b_{i+1} & 0 \leq i \leq n-2 \end{cases} \ , \tag{3.4}$$

$$\begin{bmatrix} I_{gray_r}(x, y) \\ I_{gray_g}(x, y) \\ I_{gray_b}(x, y) \end{bmatrix} = I_{gray_t}(x, y) \ , \tag{3.5}$$

$$I_h(w, y) + I_{gray_t}(x, y) = I_{gray_{rgb}}(x, y) \ , \tag{3.6}$$

3.4 Receiver Decoding System

The receiver uses a monochrome HFR camera to decode the transmitted binary images of a 24-bit RGB image; its mechanism is shown in Figure 3.9. The transmitter and receiver systems are two separate systems, and they do not implement any hardware-based synchronization; therefore, software-based synchronization is used to synchronize them. After achieving synchronization, background subtraction is used to eliminate the ambient light on the projector screen in an indoor office room to extract the projected light intensity. The camera-projector alignment is corrected using camera calibration in post-processing to correct the orientation of the reconstructed image.

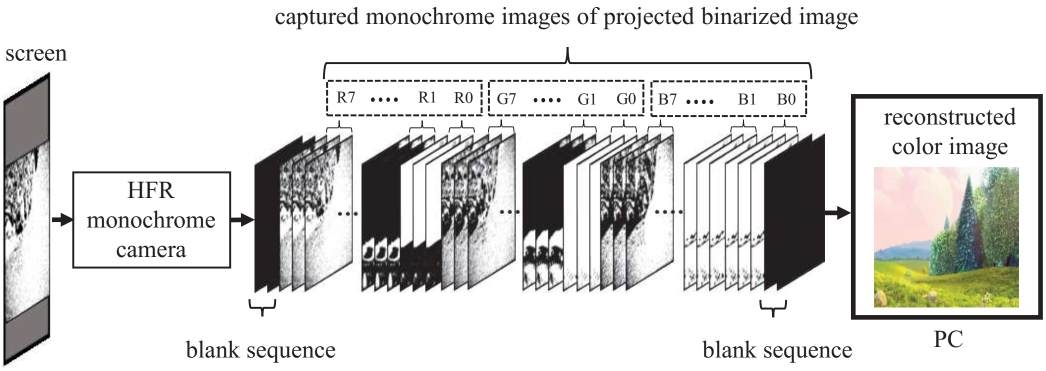

Figure 3.9: Receiver.

3.4.1 Software-Based Synchronization

For decoding and image reconstruction at the receiver, the HFR projector and HFR camera should be synchronized to capture the binary images without any loss in pixel information. The HFR projector and HFR camera operate on their respective internal system clocks and are not connected to any common hard-wired external trigger; therefore, software-based synchronization is achieved at the receiver using the HFR camera. Using the Nyquist sampling theorem, which states that a continuous-time signal can be sampled and perfectly reconstructed from its samples if the waveform is sampled over twice as fast as its highest frequency component, software-based synchronization is achieved by setting the frame rate of the HFR camera to three times that of the HFR projector. Figure

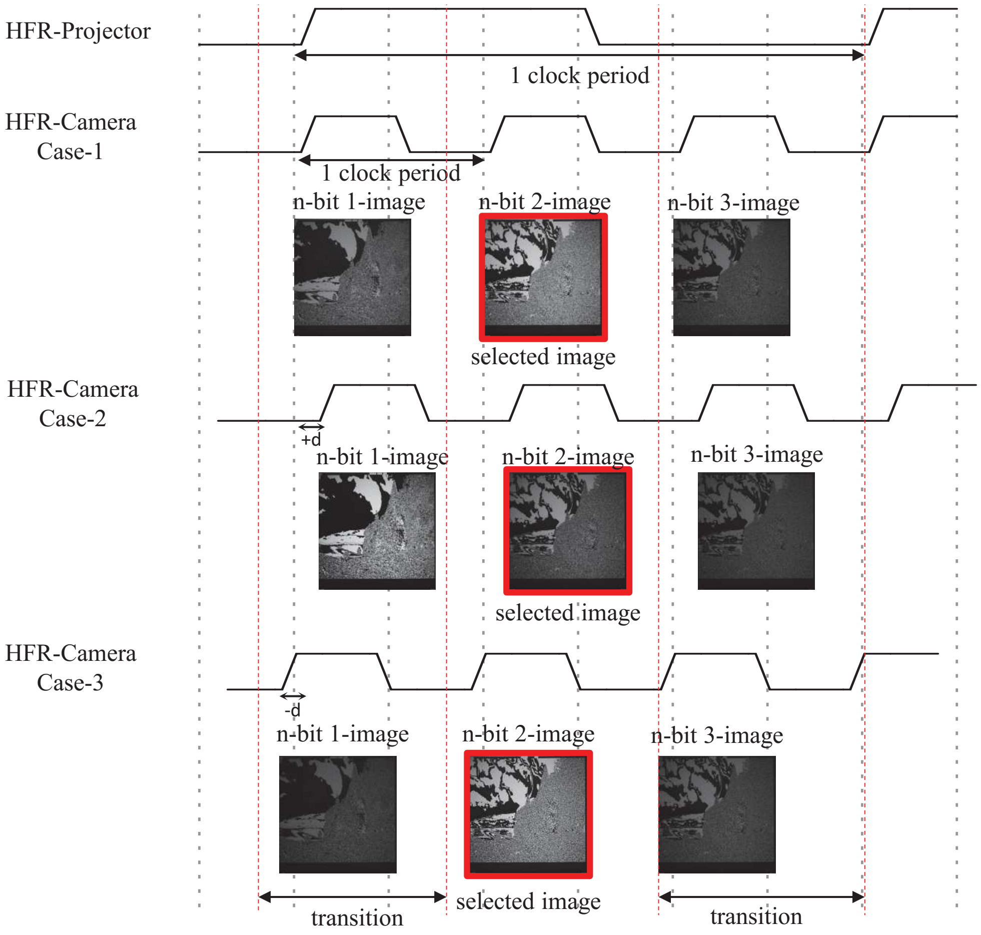

Figure 3.10: Image selection for software-based synchronization.

3.10 describes the software-based synchronization method where three images are captured for a projected binary image and a total of three cases are observed. In case-1, the HFR camera starts capturing images at the same moment as the HFR projector projects images; thus, we can observe the satisfactory brightness of the first two images. In case-2, the HFR camera starts capturing images with a delay. Consequently, we obtain good brightness in the first two images. However, in case-3, the HFR camera starts capturing images before the HFR projector starts projecting; therefore, we can observe the satisfactory brightness of the second and third images. Thus, we selected the second image to reconstruct the original image because it has significant brightness compared to the other two images that are produced during the transitional stage.

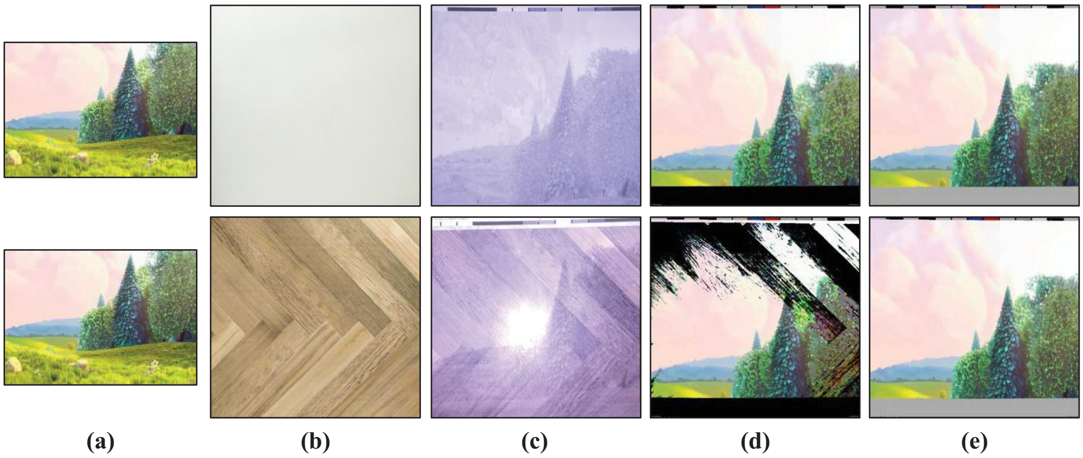

Figure 3.11: a) Original image, (b) background pattern, (c) projection on a background pattern, (d) reconstructed image without background subtraction, and (e) reconstructed image with background subtraction.

3.4.2 Background Subtraction

To eliminate the ambient light effect on the projector screen, the background subtraction with thresholding method is used. In this method, a reference image is subtracted from the input image where the reference image is estimated using the global thresholding method by projecting the maximum and minimum intensities through the HFR projector onto the screen. Let $C_{in}(u, v)$ be the input image captured by the HFR camera, $C_{thr}(u, v)$ be a reference or threshold image, and $C_{bin}(u, v)$ be the binary image obtained after background subtraction. $C_{bin}(u, v)$ is calculated using Equation (3.7), where $L(m, n)$ is the pixel value at (m, n) of $C_{in}(u, v)$ and $thr(m, n)$ is the threshold value at (m, n) of $C_{thr}(u, v)$.

$$C_{bin}(m, n) = \begin{cases} 1 & \text{for } L(m, n) \geq thr(m, n) \\ 0 & \text{for } L(m, n) < thr(m, n) \end{cases} , \tag{3.7}$$

The threshold value $thr(m, n)$ at (m, n) is calculated using Equation (3.8), where $B(m, n)$ is the pixel value at (m, n) of $C_{in}(u, v)$, captured after projecting its maximum brightness, and $D(m, n)$ is the pixel value at (m, n) of $C_{in}(u, v)$, captured after projecting a black image.

$$thr(m,n) = \frac{B(m,n)}{2} + D(m,n) \qquad , \tag{3.8}$$

To evaluate the effectiveness of background subtraction, we used plain and patterned backgrounds as the projection screens. Initially, we projected the maximum and minimum brightness onto the projection screen to evaluate the background scene, which was subtracted from the input image. Figure 3.11a shows the input image used for projection, Figure 3.11b is the background used, Figure 3.11c shows the binarized image projected onto the background surface, Figure 3.11d illustrates the reconstructed image without background subtraction, and Figure 3.11e shows the reconstructed image with background subtraction. When using a plain white background, the global threshold value does not affect the entire reconstructed image because there is uniform reflectance of light throughout the surface. However, when a colored patterned background is used the threshold limit for each pixel varies owing to the reflectance of light, depending on the color it falls on. Therefore, we cannot use a global thresholding system. Figure 3.11d shows the reconstructed image, where a global thresholding technique is used; that is, a single threshold value is used for the entire image instead of a single pixel individually. The background subtraction method described above is used at the pixel level, where the threshold value is calculated for each pixel and, then, the image is reconstructed accordingly, as shown in Figure 3.11.

3.4.3 Synthesizing 24-Bit RGB Image

To synthesize or reconstruct the original image, the images obtained after software-based synchronization are binarized using background subtraction and sequentially combined by checking the header information, which consists of the frame number, color-channel information, and bit-plane sequence of each channel. A threshold value T is required to extract data from the header information blocks which is constant and does not change dynamically as the threshold $thr(m,n)$. The threshold value T determines the ”0” and ”1” bits of the header information and is calculated using Equation (3.9), where B_{max}

is the maximum brightness of a pixel in an image when projecting white light and D_{min} defines the minimum brightness of a pixel in an image when projecting a black image.

$$T = \frac{B_{max}+D_{min}}{2} \quad , \tag{3.9}$$

To explain the process of synthesizing a 24-bit RGB color image, consider a gray-level input image $C_{in}(u,v)$ captured by the HFR camera and its corresponding binarized images of three channels as $C_{bin_{r(t)}}(u,v)$, $C_{bin_{g(t)}}(u,v)$ and $C_{bin_{b(t)}}(u,v)$ image which is then combined to form a single 24-bit RGB color image $C_{RGB}(u,v)$ as shown in Equation (3.10) where t is the bitplane number of 8-bit channels. The $C_{RGB}(u,v)$ image is an encoded gray-code-based image that is further decoded to a pure-binary-code-based image by using Equation (3.11) at the pixel level to obtain the reconstructed RGB color image $I_{RGB}(u,v)$.

$$\begin{bmatrix} C_{bin_{r(t)}}(u,v) \\ C_{bin_{g(t)}}(u,v) \\ C_{bin_{b(t)}}(u,v) \end{bmatrix} = C_{RGB}(u,v) \quad 0 \leq t \leq 7 \ , \tag{3.10}$$

$$b_i = \begin{cases} g_i & i = n{-}1 \\ b_{i+1} \oplus g_i & 0 \leq i \leq n-2 \end{cases} \quad , \tag{3.11}$$

Chapter 4

Synchronizing HFR projector-camera system at 3000 fps

4.1 Concept of Proposed Visual Feedback-based Synchronization Algorithm

A visual feedback-based synchronization algorithm is used to mitigate the complexities and stabilization issues of wire-based triggering for long-distance systems. To synchronize the HFR camera with HFR projector, the operating frequency of the HFR camera and HFR projector is kept same and the phase of HFR camera is alligned to match the phase of HFR projector. The block diagram of the concept of the visual feedback-based projector-camera synchronization system is shown in Figure 4.1. The HFR projector is triggered using an external trigger 1 source (function generator 1), whereas the HFR camera is triggered using another external trigger 2 source (function generator 2). A predefined binary pattern is projected and captured by the HFR camera to calculate the maximum brightness and generate a delay using a proportional control-based algorithm. This delay is added to the trigger signal of the HFR camera clock to match the HFR camera and projector phases. As a result, we attain maximum and minimum brightness by adding a delay to the camera clock of the HFR camera system.

To achieve this, the control logic of the timing controller was implemented on an FPGA on the external board attached to the HFR camera, as shown in Figure 4.2. The HFR camera can calculate and generate a delay with the help of an external trigger, but

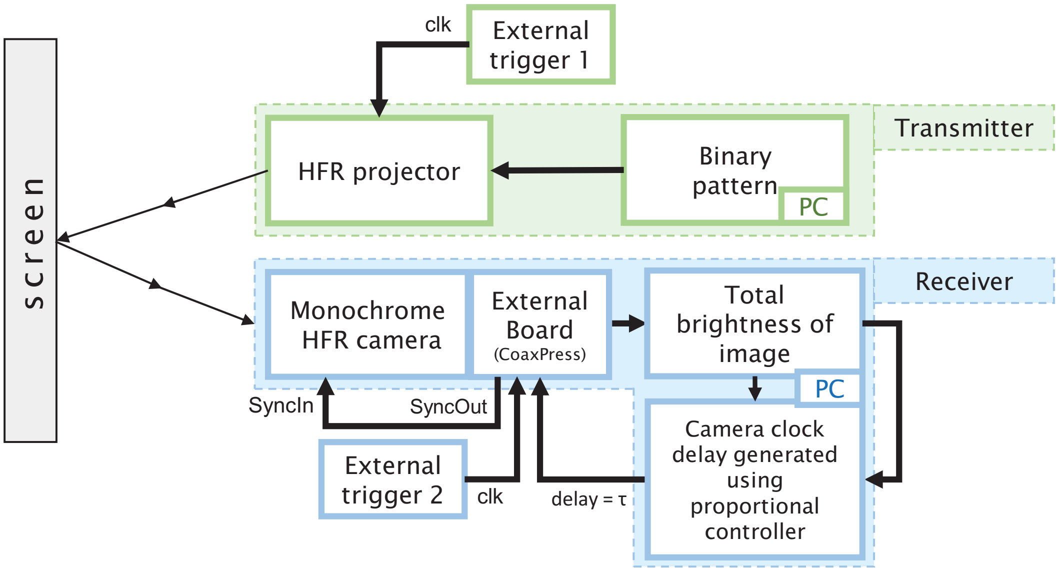

Figure 4.1: Concept diagram of visual-feedback-based HFR projector-camera synchronization.

the values of the required control parameters should be given by users according to their needs. The sync timing controller generates a delay value of τ_1, which is passed to the sync signal generator, adding a delay to the input clock, *clk*, to generate a delayed output clock signal, $SyncOut$, to match the phase of the HFR projector. The value of delay, τ_1, is the same as τ, which is calculated using our visual feedback algorithm and is given to the timing controller via register access. An external trigger clock with frequency f is given to the sync signal generator of the external board, which is then delayed by the delay value, τ_1, to provide a delayed signal to the digital input–output block. This is connected to the HFR camera that provides the required delay to the HFR camera clock to match the phase of the HFR projector.

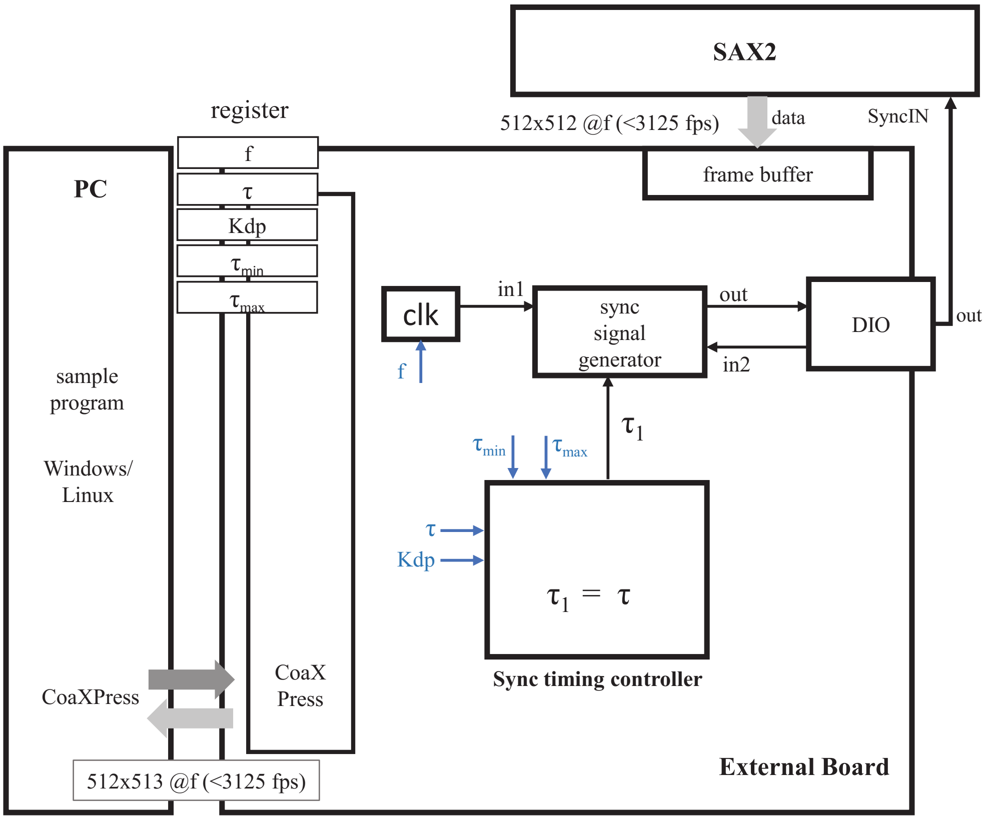

Figure 4.2: Control logic for visual-feedback-based projector-camera synchronization implemented on an external board.

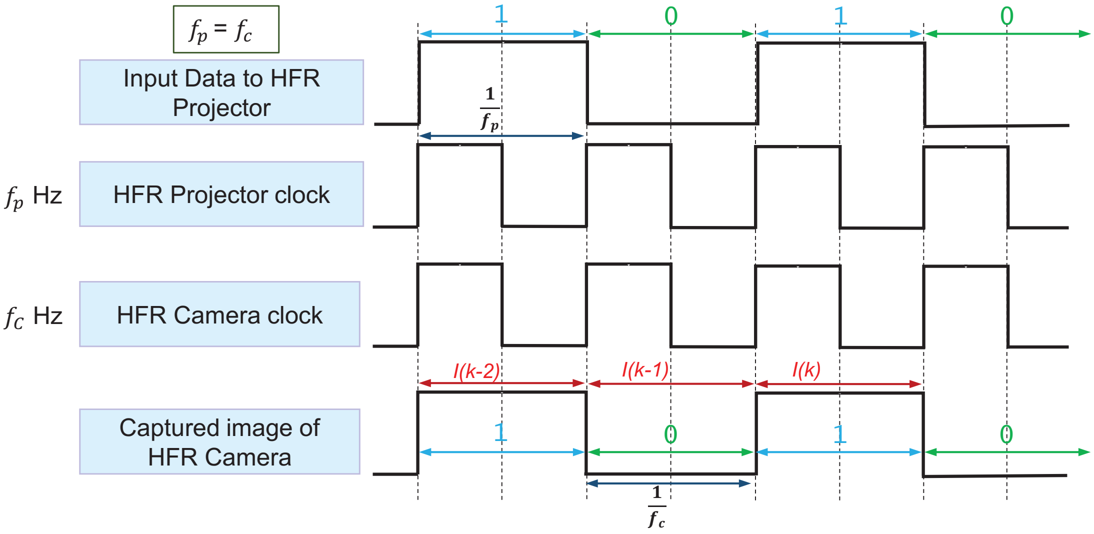

Figure 4.3: Timing diagram of visual-feedback-based projector-camera synchronization.

To calculate the delay value, τ, the projector projects a predefined pattern at a frame rate of F_p while the camera captures individual frames at a frame rate of F_c. The ideal case where the HFR camera is synchronized with the HFR projector is shown in Figure 4.3. Here, a predefined binary pattern is projected sequentially, where white and black images are represented by 1 for maximum brightness and 0 for minimum brightness, respectively.

There are three cases of phase difference as shown in Figure 4.4. In the first two cases, the phase of the HFR camera is out of phase with the HFR projector (i.e., case-1 and case-2). In case-1, there is a delay in the camera trigger compared with the projector, whereas in case-2, the camera is triggered before the projector. Thus, projector phase P_p is not equal to camera phase P_c. In case-3, the camera and projector are both triggered simultaneously, which is the desired result after synchronization.

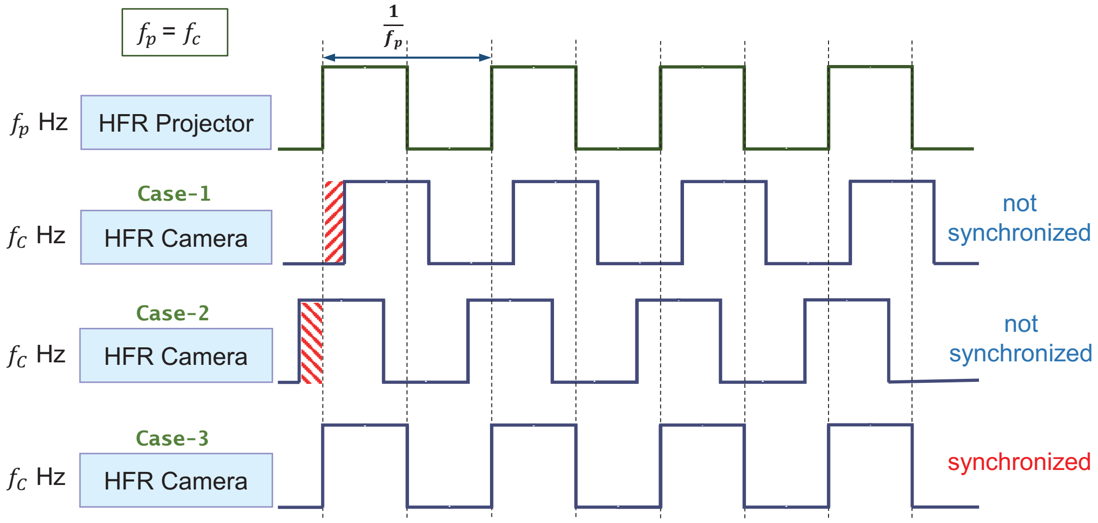

Figure 4.4: Projector-camera synchronization error.

Therefore, case-1 and case-2 can be synchronized, and the HFR camera can be triggered with the same phase as that of the HFR projector by adding a delay of τ to F_c, as shown in Figure 4.5 and Figure 4.6. As with case-1 in Figure 4.5, there is a delay in triggering F_c; therefore, to match P_c with P_p, we must generate a large delay, τ. In case-2, we require a small delay, τ, to match P_c with P_p as F_c is triggered prior to the HFR projector, as shown in Figure 4.6.

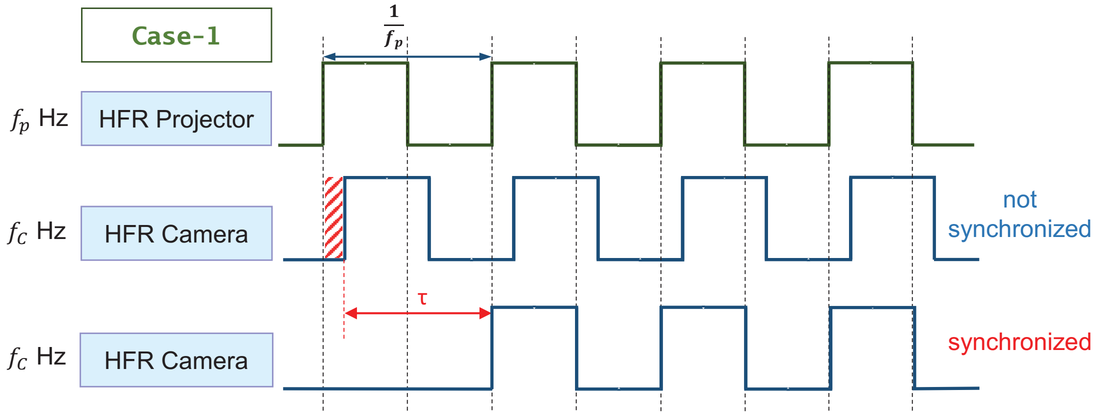

Figure 4.5: Timing control of synchronization error case-1.

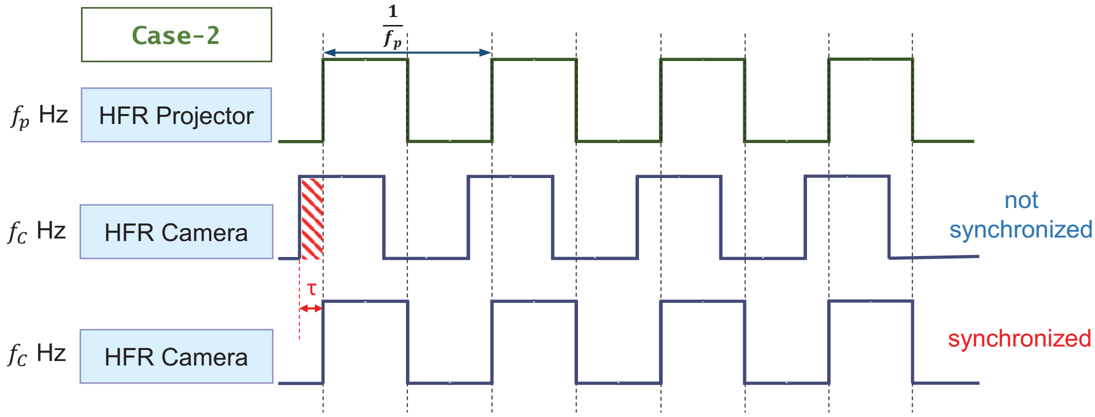

Figure 4.6: Timing control of synchronization error case-2.

To calculate the value of τ, we must initially calculate the brightness-based index, $R(k)$, which is the ratio of the total brightness of two images at consecutive frames, where $S(k)$ is the total brightness sum of the input image at the current frame, k, and $S(k-1)$ is the brightness at the previous frame, $k-1$.

$$R(k) = \frac{S(k)}{S(k-1)} \qquad , \tag{4.1}$$

$$R(k-1) = \frac{S(k-2)}{S(k-1)} \qquad . \tag{4.2}$$

Next, we evaluate the error, *C(k)*, where $R(k-1)$ is the previous brightness-based index calculated using Eq. 4.2.

$$C(k) = R(k) - R(k-1) \qquad . \tag{4.3}$$

The delay, τ, is calculated for proportional control by considering the delay, $\tau(k-1)$, at the previous frame and error, $C(k)$, multiplied by a constant proportional gain, K_{d_p}. The value of τ lies between τ_{max} and τ_{min}, τ_{max} is set to maximum exposure duration of the camera, and τ_{min} is zero.

$$\tau(k) = \tau(k-1) + K_{d_p} \cdot C(k) \qquad \tau_{max} > \tau \geq \tau_{min} \qquad . \tag{4.4}$$

4.2 Verification of Algorithm at Different Shutter Speed

Considering the above-mentioned synchronization algorithm, experiments were conducted to verify its performance at a high frame rate. The HFR projector alternately projected bit-plane images of black and white patterns through a 24-bit color image. The value of each bit plane image (black or white) is decided by the 8-bit pixel value of a single channel which was set to decimal 170 (10101010 in binary). The HFR projector frame rate was set to 3,000 fps, and the exposure of each frame was set to a maximum exposure time of 331 μs. The HFR camera was set to 3,000 fps, the exposure time of each frame was set to 1/3015 s (331 μs) to capture the black and white patterns alternately. Because the visual feedback control algorithm depends on the total brightness of an image, the black and white patterns was determined by the maximum and minimum total brightness of the captured image. The output graph of synchronization is shown in Figure 4.7, where the zoomed portion shows a pattern that the total image brightness drops after every 24 bit due to the projection of a blank image by HFR projector between two images. Figure 4.7 shows that the HFR camera phase, P_c, was initially not in sync with the HFR projector phase, P_p, due to this the blending of projected black and white patterns resulted in inaccurate total brightness of the captured images. Therefore, during the initial duration of approximately 6 s the total brightness information was inaccurate. After this, the synchronization algorithm was executed, and the value of delay, $\tau(k)$, was calculated using $S(k)$, $R(k)$, and $C(k)$. The delay, $\tau(k)$, was given as input to τ_1 of the sync timing controller on the FPGA of the external board, which generated a $SyncOut$ signal to trigger the HFR camera and match the phase (P_c) with the phase (P_p) of HFR projector. The proportional gain, K_{d_p}, was set to 0.01 to achieve synchronization in shorter duration with stability. Figure 4.7 shows that the calculated delay, $\tau(k)$, was 0.177 ms, and the HFR camera-projector system was synchronized in approximately 20 ms. As a result, in the synchronized system, the total brightness of the captured image from the HFR camera increased when a white image was projected, and decreased when a black image was projected.

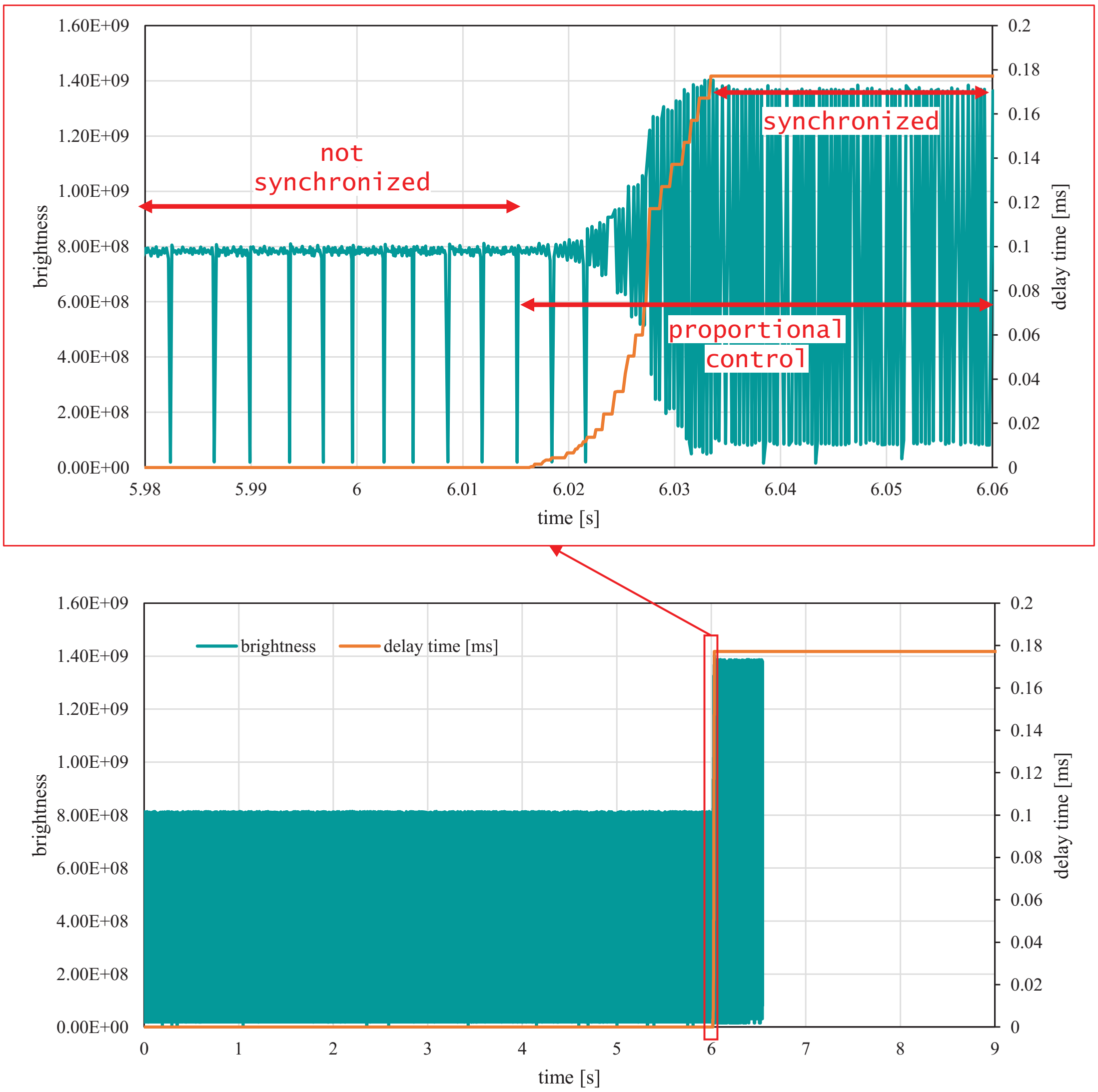

Figure 4.7: Relationship between total brightness and delay during alternative black-and-white projection at 3,000 fps.

HFR camera exposure times of 1/3,015, 1/8,000, and 1/12,500 were selected to evaluate the performance of our proposed algorithm, which can work with a very short exposure time of 1/12,500 and large exposure time of 1/3,015, as shown in Figure 4.8. The projector frame rate was set to 3,000 fps with the exposure time 331 μs and the bit-plane images of black and white patterns was projected alternately. The HFR camera frame rate was set to 3,000 fps and the exposure time was kept at 1/3,015, 1/8,000, and 1/12,500 under a constant room luminescence of 150 lx. Initially, the HFR camera and projector was not in sync for approximately 3 s, after which the synchronization algorithm was executed to calculate the delay, $\tau(k)$, depending on the total brightness of an image. Figure 4.8 shows that the HFR camera-projector is synchronized under different frame exposure times with different levels of total image brightness. The value of delay $\tau(k)$ was never constant for a particular frame exposure time and varied depending on either case-1 and case-2, as discussed above. From this experiment, we can deduce that the system works with a wider range of exposure times and provides system flexibility. Figure 4.8 shows that synchronization is achievable for all selected ranges, but the only difference is the total brightness of the image.

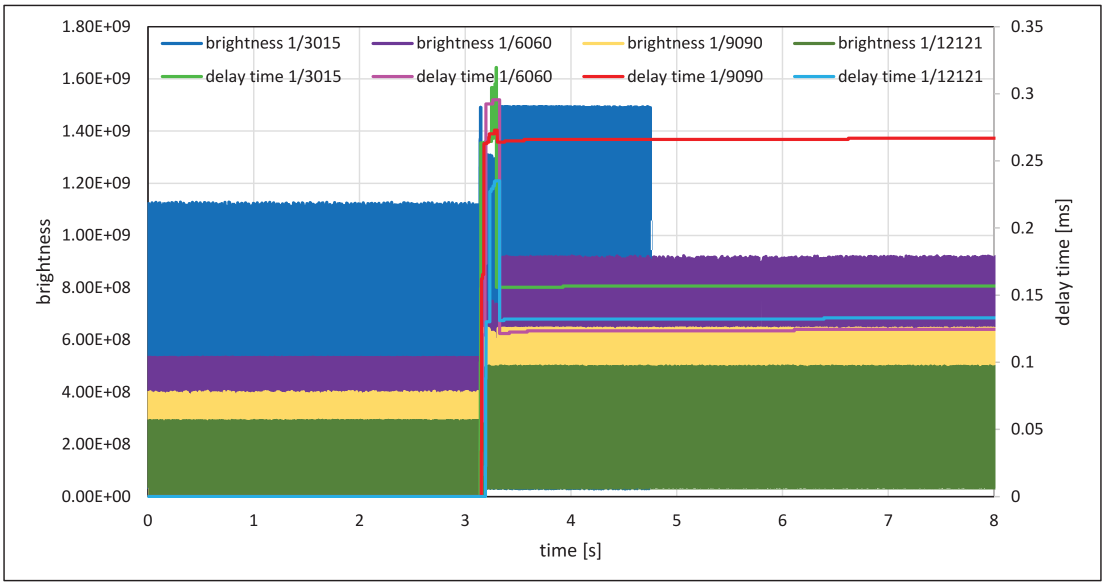

Figure 4.8: Relationship between total brightness and delay when 3,000 fps black-and-white projection is captured at different exposures.

Chapter 5

Results and Discussions

5.1 Evaluating real-time HFR projector-camera based VLC system

The HFR-projector-camera system was set up in a controlled laboratory environment, and the corresponding experiments were conducted to evaluate the performance and image quality of the proposed VLC system. The projected video 590×1,080 is a combination of 590×1,060 gray-code images and 590×20 header information, projected in a bit plane sequence using the HFR projector. The bit plane sequence used for binary projection is shown in Figure 3.6, where the green channel is projected first in a bit-plane sequence, followed by red and blue channel and the duration of exposure for each pattern is 960 μs. Therefore, the total duration for all bit-plane images is 23,040 μs, which is less than the *vsync* duration of the input video to avoid any frame loss. A 50-mm lens was mounted on the HFR camera, which was set to a maximum frame rate of 3,125 fps. Therefore, the maximum frame rate of the HFR projector that can be used for projection for our system is 1,041 fps, which is one-third of the HFR camera frame rate required for software-based synchronization. The experimental setup is shown in Figure 5.1a, where the distance between the HFR projector and screen is 950 mm and the projection display onto the screen is 448 mm × 415 mm. The distance between the HFR camera and screen is 1,130 mm to ensure that the overall area of the projected video on the screen is captured by the camera. The experiments were performed on plain and patterned backgrounds, as shown in Figure 5.1b, for the proposed system for (a) a stored video sequence and (b) live

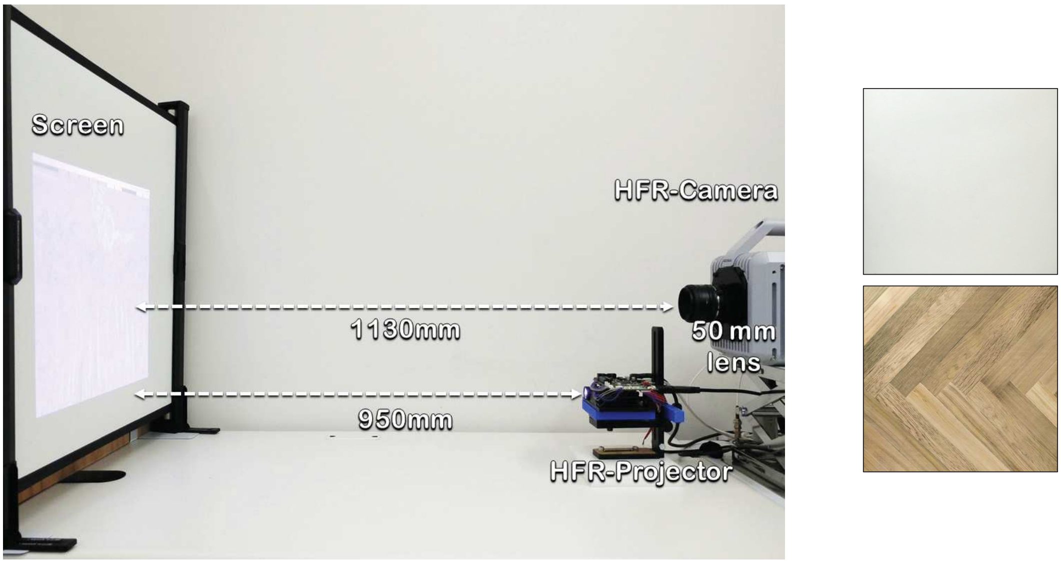

Figure 5.1: (a) Overview of the HFR projector-camera system. (b) Plain and patterned background.

video streaming from a USB camera. On the patterned background, the header information projected on a white background for the proper detection of header information. In addition, the indoor environment was illuminated with three different luminescence values (i.e., 0, 150, and 300 lux), using an external light source to evaluate the robustness of our system with respect to the ambient light.

5.1.1 Real time video reconstruction of saved video

For a real-time video streaming experiment with a stored video sequence, we used the movie ”BigBuckBunny” [92]. First, we estimated the background scene by projecting the maximum and minimum brightness for background subtraction. The pure-binary-code input images of 24-bit 1920×1,080 RGB-color video were resized to 590×1060 which was then encoded to 590×1,060 gray-code images, along with the addition of 590×20 header information, and projected using bit-plane or binary images at 1,041 fps. The HFR camera captures 512×512 images and reconstructs the output image with a resolution of 510×459 by combining all bit-planes of a 24-bit RGB image sequentially. Figure 5.26 shows the comparison of the input image with binary-code-based projection and gray-code-based projection with background subtraction on a plain background. Figure

5.26a shows the full high definition input image 1920×1,080 at 31 fps. Figures 5.26b,d depicts the reconstructed images 510×459 using pure-binary-code and gray-code respectively, without background subtraction. Figures 5.26c,e depicts the reconstructed images 510×459 using pure-binary-code and gray-code respectively, with background subtraction. Similarly, the experiments were performed for the patterned background, as shown in Figure 5.3. The images reconstructed with pure-binary-code exhibited artifacts due to the ambiguity of pixels with high spatial frequency; these artifacts were removed in the images reconstructed using gray-code-based transmission.

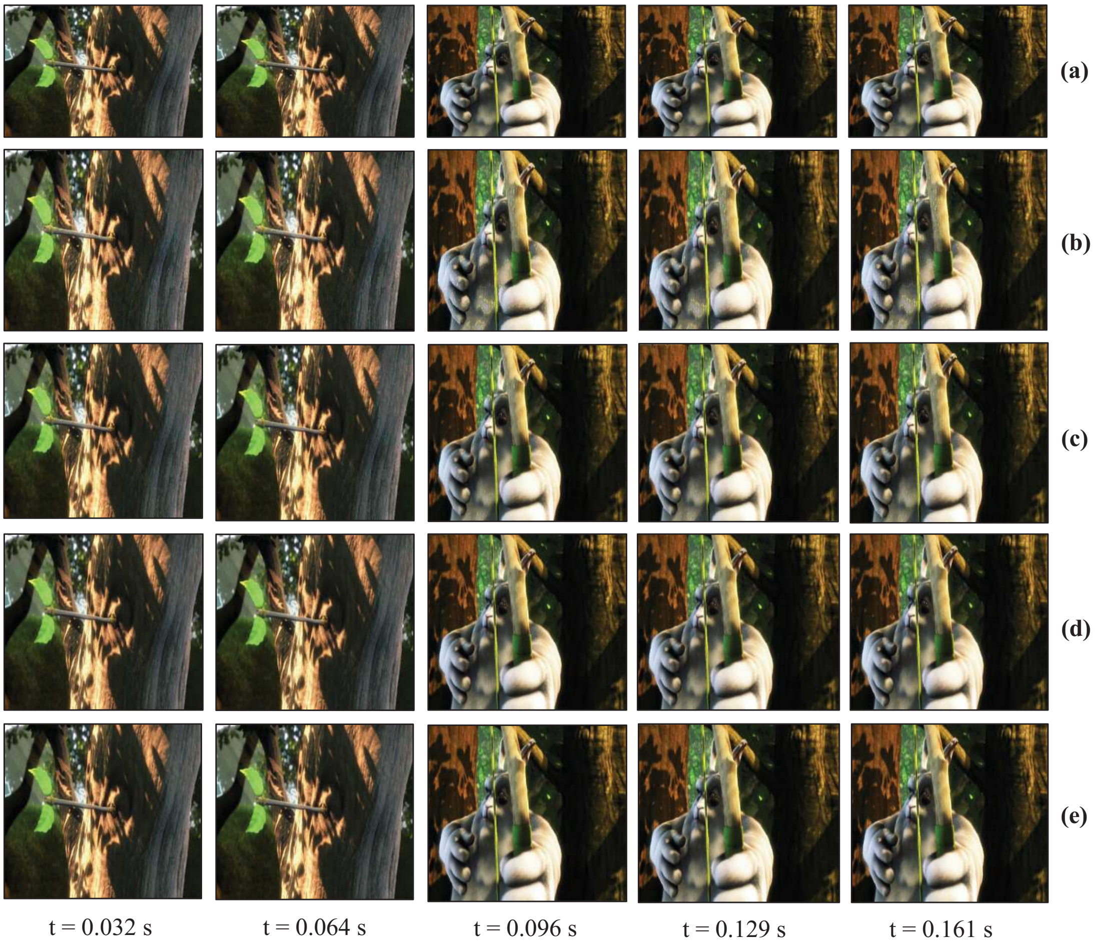

Figure 5.2: Reconstructed saved image sequence on plain background: (a) 1920×1080 input image, (b) 510×459 binary-code image without background subtraction, (c) 510×459 binary-code image with background subtraction, (d) 510×459 gray-code image without background subtraction, and (e) 510×459 gray-code image with background subtraction.

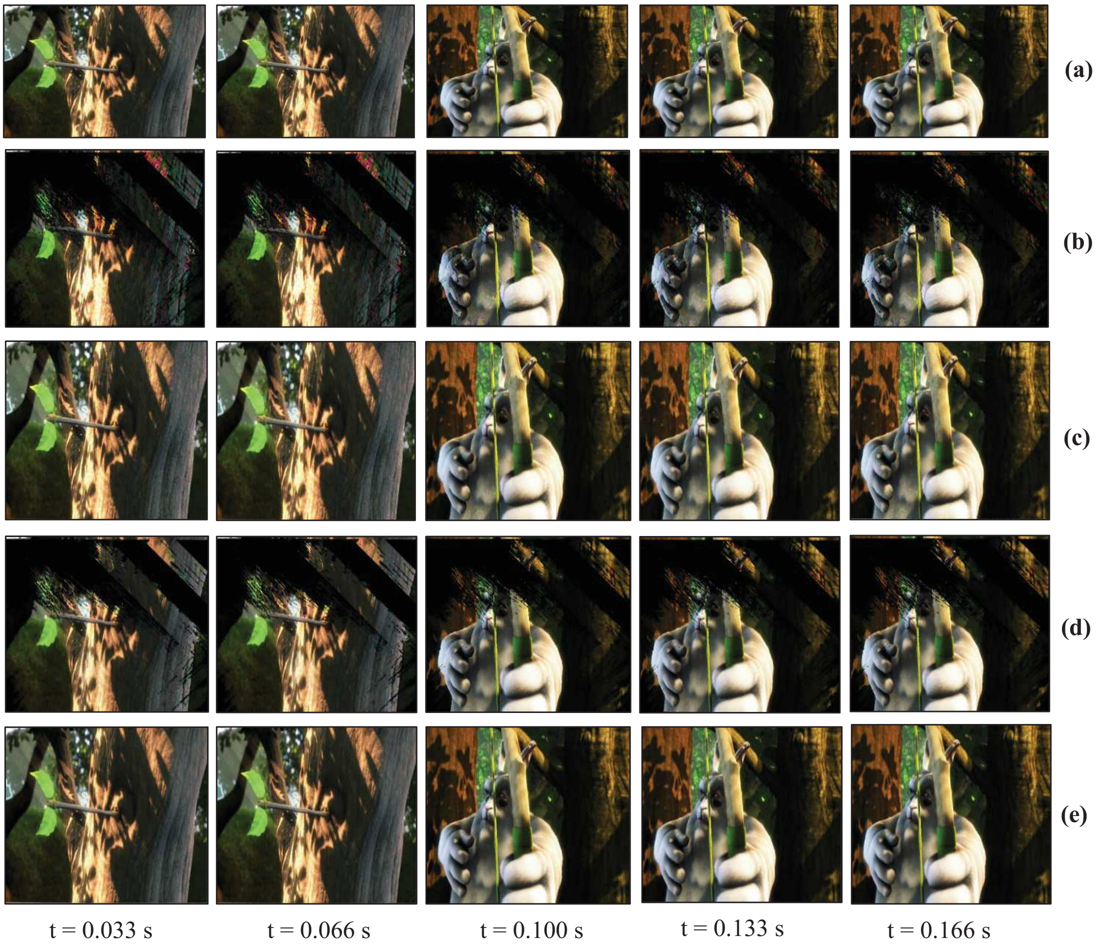

Figure 5.3: Reconstructed saved image sequence on patterned background: (a) 1920×1080 input image, (b) 510×459 binary-code image without background subtraction, (c) 510×459 binary-code image with background subtraction, (d) 510×459 gray-code image without background subtraction, and (e) 510×459 gray-code image with background subtraction.

The image quality analysis and performance evaluation of the system measured under different on-screen luminescence of 0, 150, and 300 lux for three different input frame rates 11, 21, and 31 fps, for approximately a hundred consecutive frames are shown in Figure 5.4, Figure 5.6, Figure 5.5, Figure 5.7, and Figure 5.29. Figure 5.4, Figure 5.6, Figure 5.5, and Figure 5.7 shows the image quality by measuring the PSNRs and MS-SSIMs, where gray-code-based video reconstruction with background subtraction has a better quality index in comparison to others with respect to different luminescence values.

We observed that the image quality was reduced on the patterned background compared to the plain background; however, the luminescence was increased to 300 lux, the patterned background with a slightly darker shade showed a better reconstructed image quality than the image reconstructed with gray-code on a plain background. Figure 5.29(a) and Figure 5.29(b) shows that on plain and patterned backgrounds, the reconstructed image without background subtraction slightly differs from the image reconstructed with background subtraction, and there is a marginal difference between the images reconstructed using pure-binary-code and gray-code. However, as we increase the transmission frame rate, the reconstruction frame rate also starts dropping owing to the limited transmission bandwidth. Figure 5.10 and Figure 5.11 show the images reconstructed at different luminescence values on plain and patterned backgrounds, respectively. It is evident that the background subtraction method is significantly effective even when the luminescence is increased.

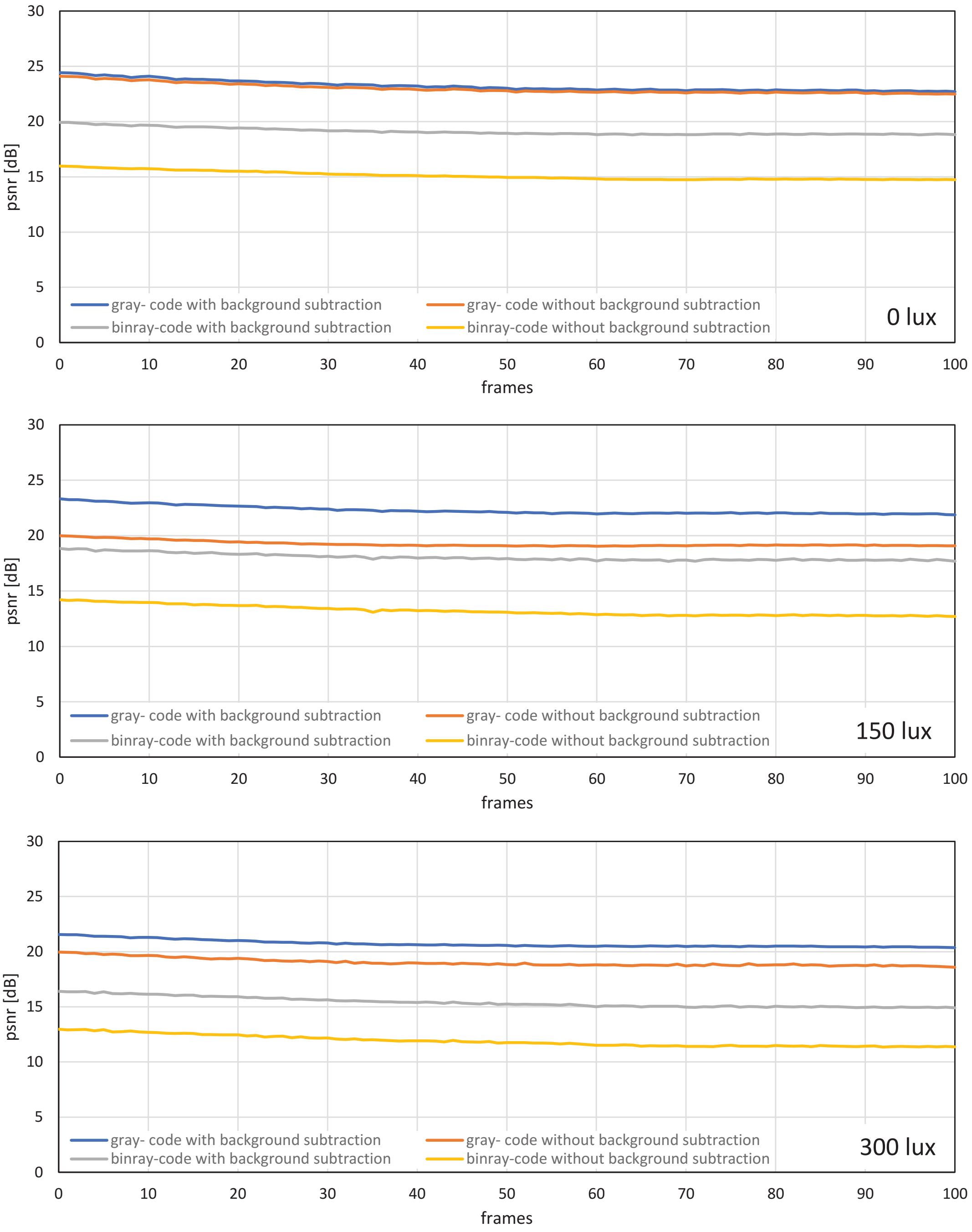

Figure 5.4: PSNRs when a stored video sequence is streamed with pure-binary-code and gray-code images on plain background.

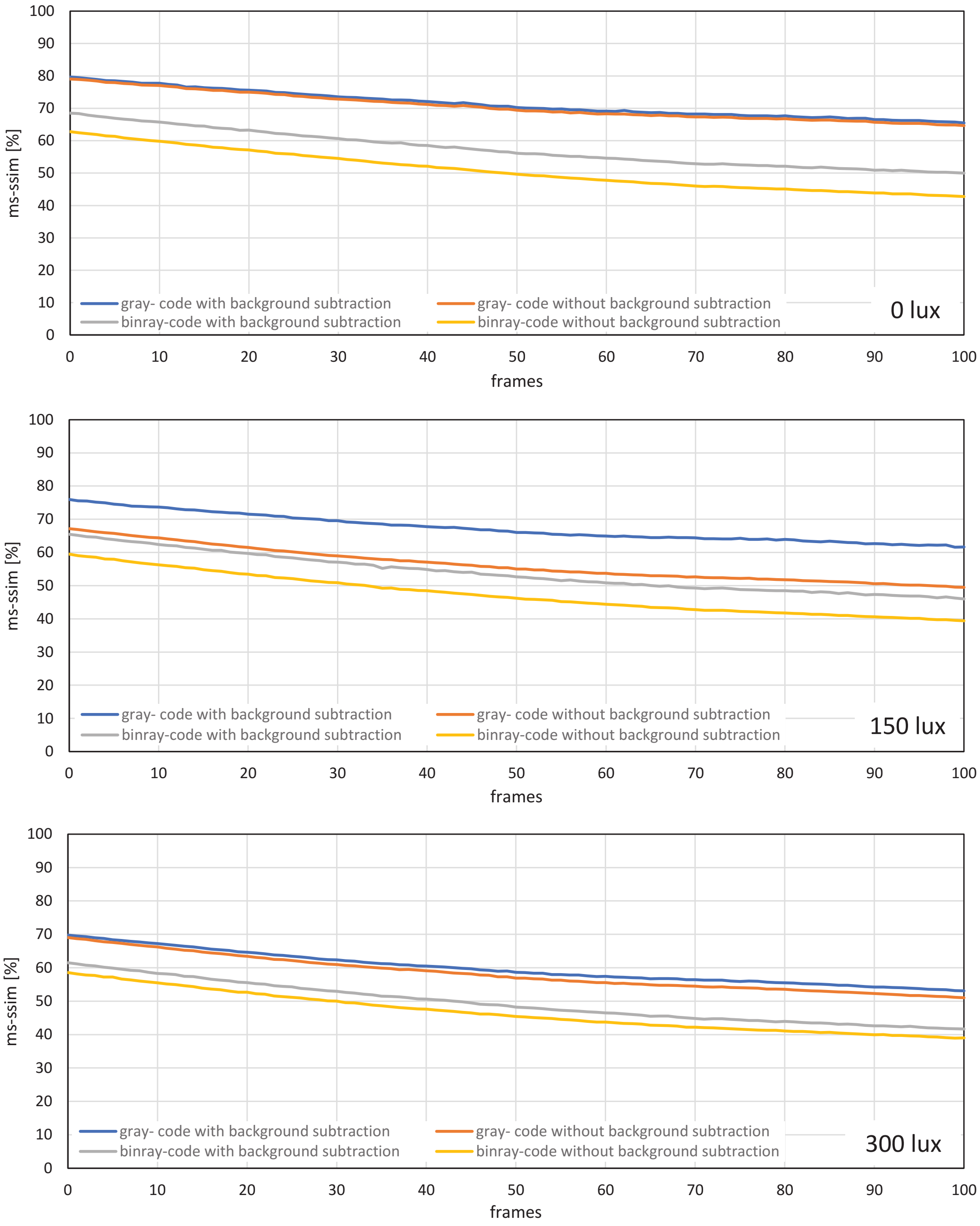

Figure 5.5: MS-SSIMs when a stored video sequence is streamed with pure-binary-code and gray-code images on plain background.

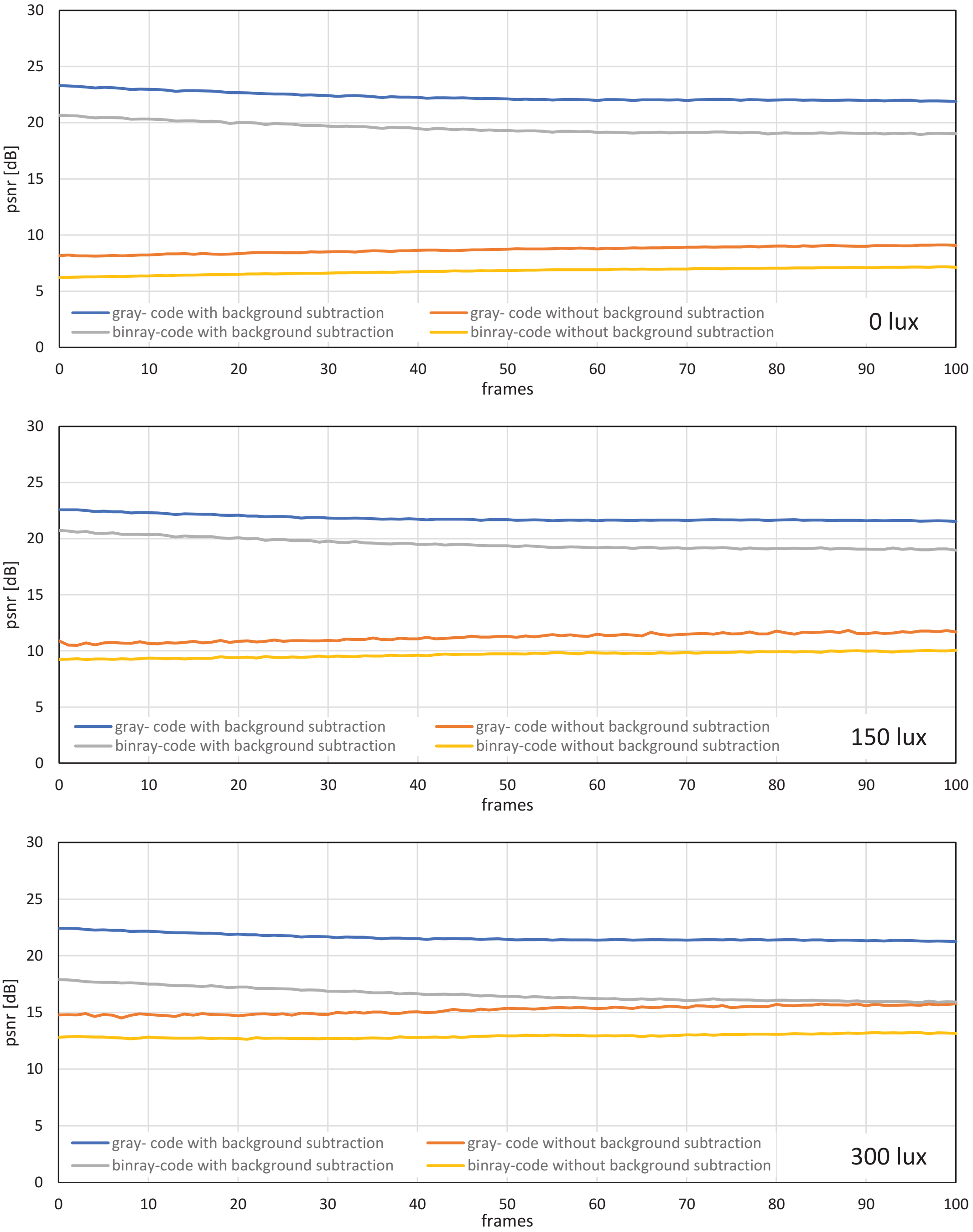

Figure 5.6: PSNRs when a stored video sequence is streamed with pure-binary-code and gray-code images on patterned background.

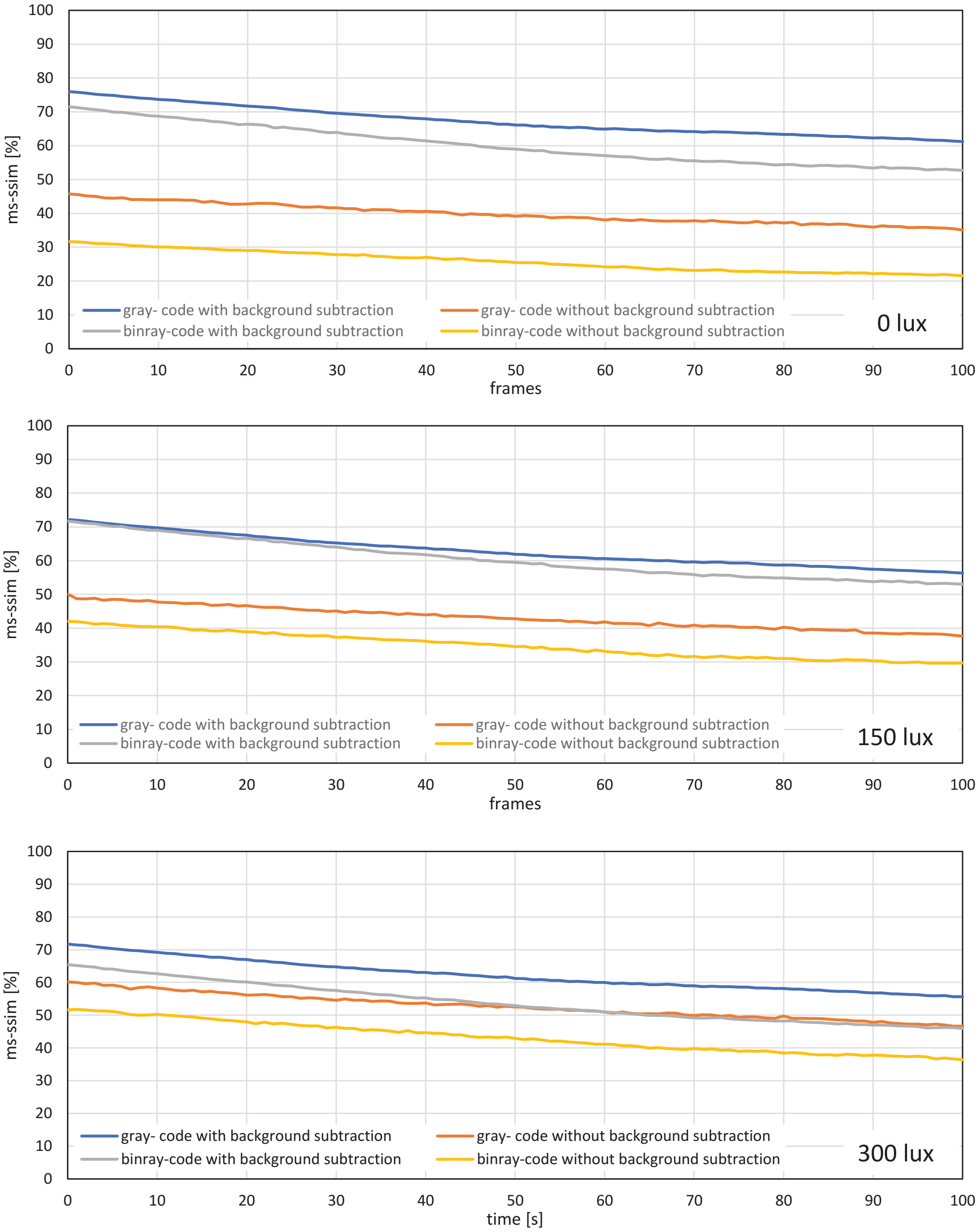

Figure 5.7: MS-SSIMs when a stored video sequence is streamed with pure-binary-code and gray-code images on patterned background.

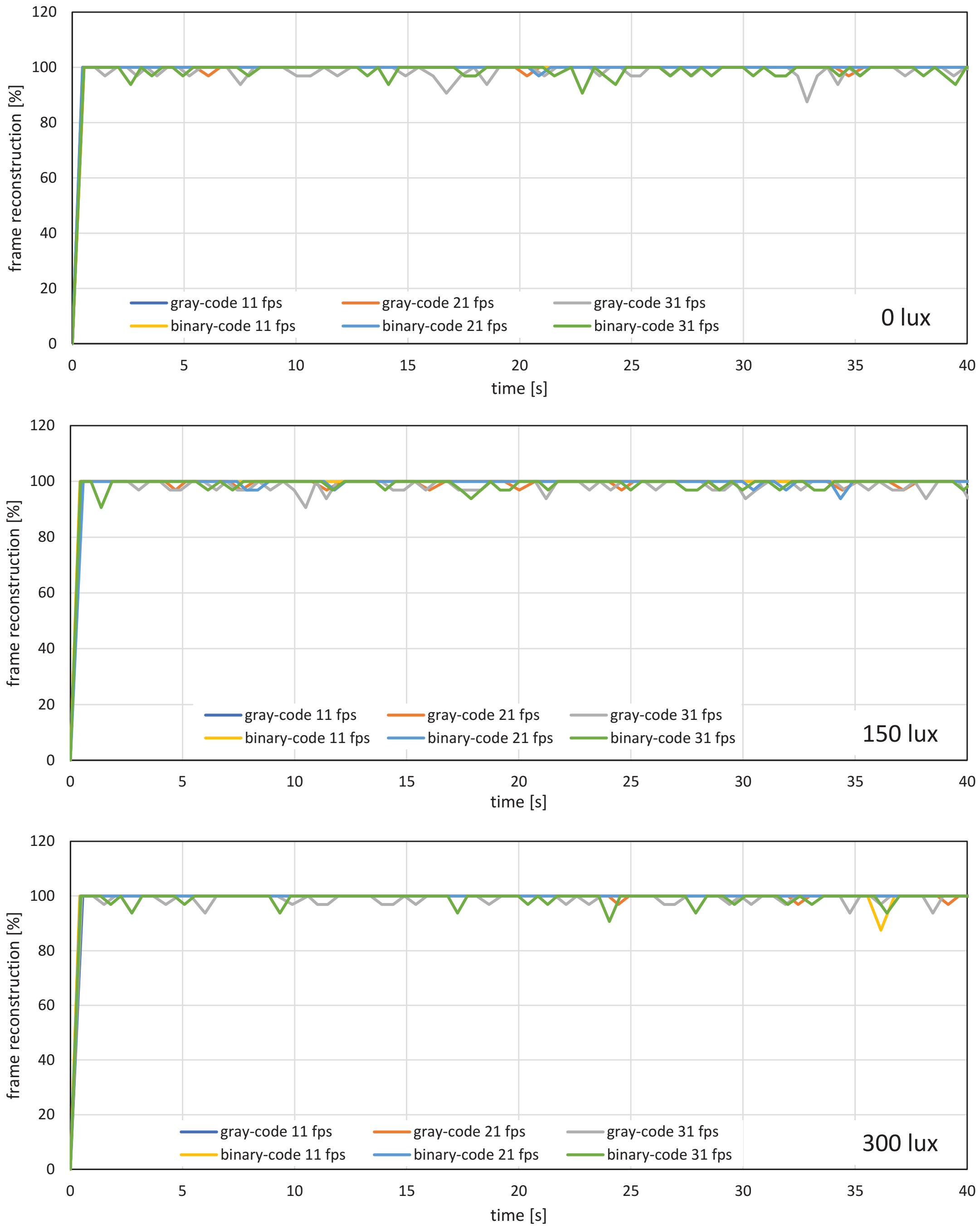

Figure 5.8: Frame reconstruction ratio when a stored movie is streaming on plain background.

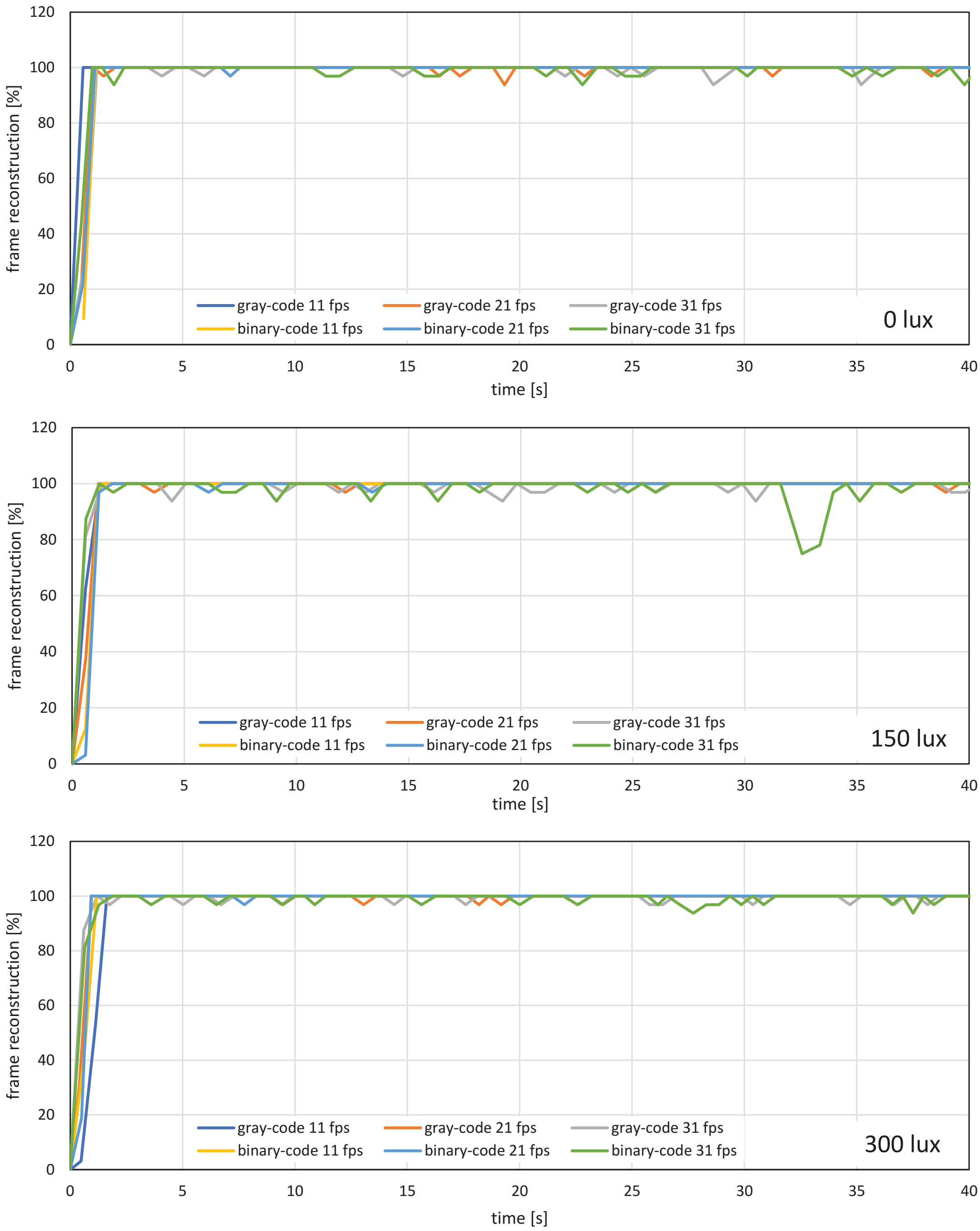

Figure 5.9: Frame reconstruction ratio when a stored movie is streaming on patterned background.

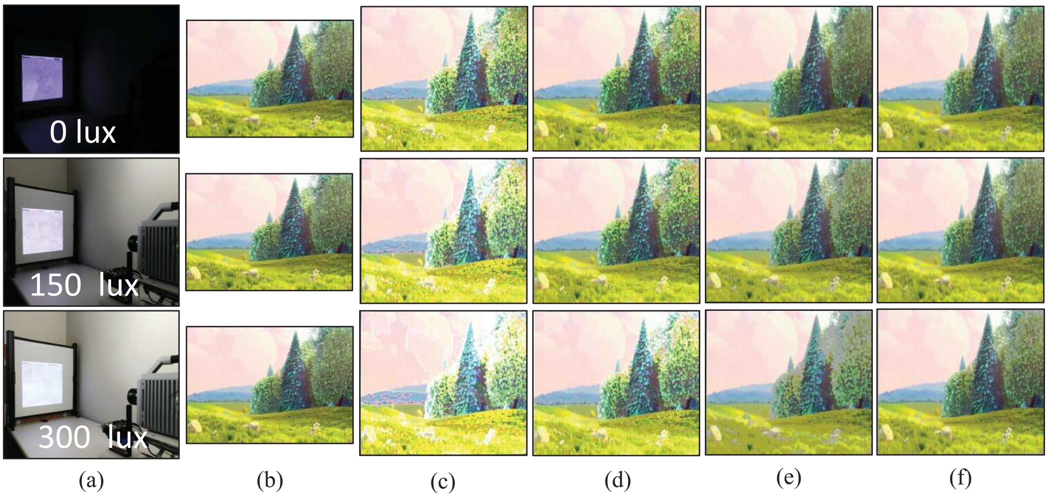

Figure 5.10: Plain background: (a) experiment scene at different illuminance levels, (b) 1920×1080 input images, (c) 510×459 images reconstructed using pure-binary-code without background subtraction, (d) 510×459 reconstructed images with pure-binary-code with background subtraction, (e) 510×459 reconstructed images using gray-code without background subtraction, and (f) 510×459 reconstructed images using gray-code with background subtraction.

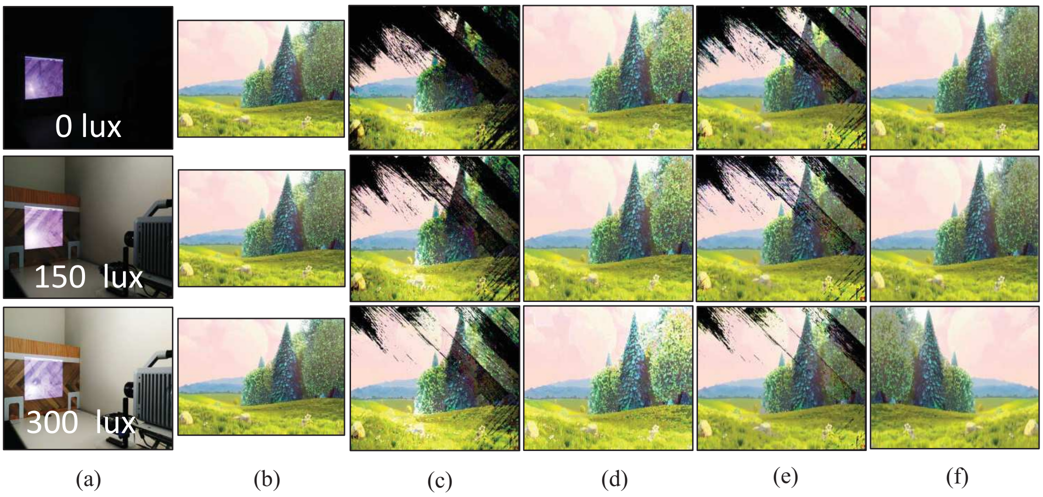

Figure 5.11: Pattern background: (a) experiment scene at different illuminance levels, (b) 1920×1080 input images, (c) 510×459 images reconstructed using pure-binary-code without background subtraction, (d) 510×459 reconstructed images with pure-binary-code with background subtraction, (e) 510×459 reconstructed images using gray-code without background subtraction, and (f) 510×459 reconstructed images using gray-code with background subtraction.

5.1.2 Real time video reconstruction of USB camera live video

The USB camera experiment was performed to verify the efficiency and performance of real-time video streaming for videos through a camera. In this experiment, the input video sequence was obtained from a USB camera(XIMEA, MQ003CG-CM), which is a 24-bit color camera, and its image resolution was set to 640×480 at 30 fps for transmission considering the conventional USB camera parameters. The experimental setup is shown in Figure 5.12. The experimental scene consists of a person throwing a football on the floor, and the HFR projector is set to 1,041 fps with the same binary projection sequence as in Figure 3.6, along with an HFR camera frame rate of 3,125 fps. Figure 5.13 and Figure 5.14 shows the comparison between pure-binary-code based and gray-code based reconstructed image sequences on the plain background, respectively. From Figures 5.13 and 5.14, we can observe the reduction in artifacts when using gray-code-based encoding to reconstruct the image. Similarly, Figures 5.15 and 5.16, show the comparison between pure-binary-code based and gray-code based reconstructed image sequences on the patterned background, respectively. The effectiveness of background subtraction method is evident from the reconstructed images in Figures 5.15 and 5.16. Figure 5.18 shows the performance evaluation for the reconstructed USB camera video with three different input frame rates 11, 21, and 31 fps for ambient luminescence of 0, 150 and 300 lux considering 100 consecutive images; their image qualities were measured using PSNR and MS-SSIM, as shown in Figure 5.20, Figure 5.21, Figure 5.22, and Figure 5.23 for the plain and patterned backgrounds, respectively. Figure 5.18 depicts that with the increase in ambient light, a slight increase in frame loss can be observed at the receiver. Overall, the images reconstructed using gray-code with background subtraction have a higher image quality compared to other methods, and almost no frame loss is observed at 0 lux.

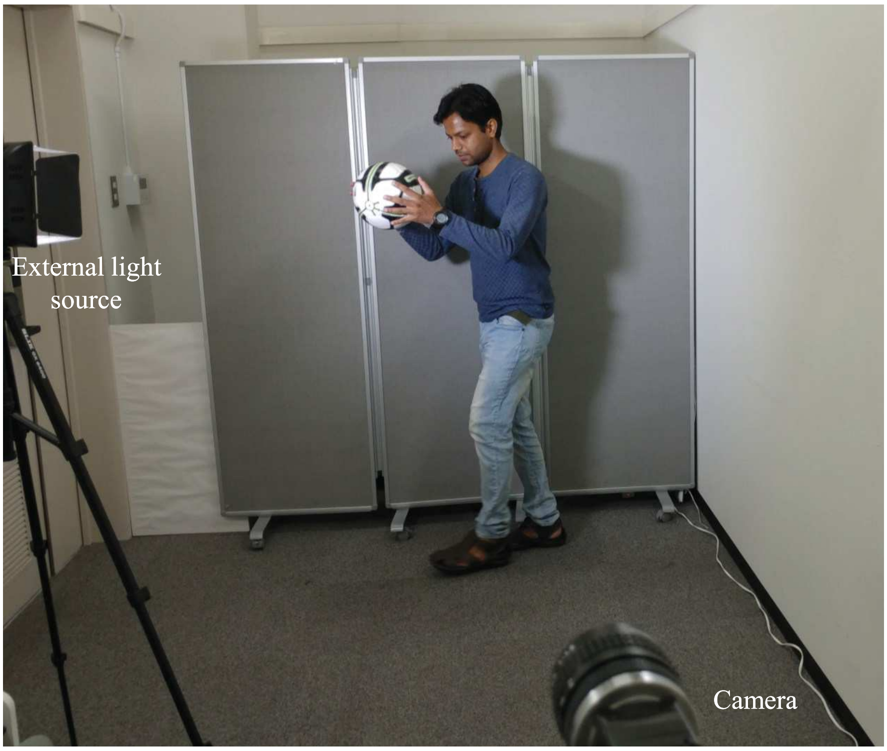

Figure 5.12: Experiment setup for HFR-projector-camera system using a USB camera as input.

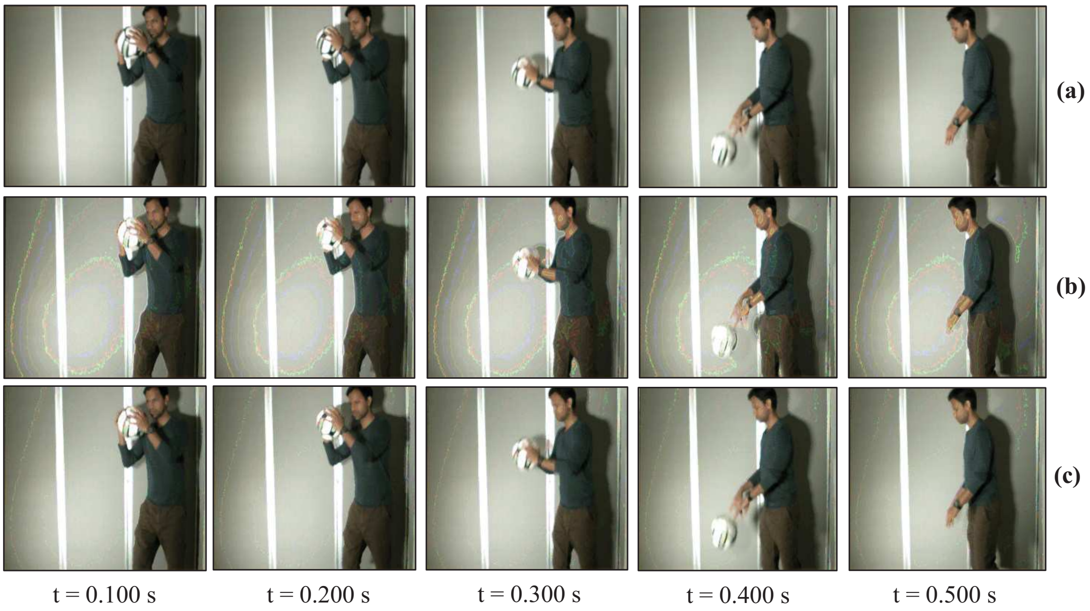

Figure 5.13: Reconstructed USB camera input image sequence on the plain background: (a) 640×480 input image, (b) 510×459 binary-code image without background subtraction, and (c) 510×459 binary-code image with background subtraction.

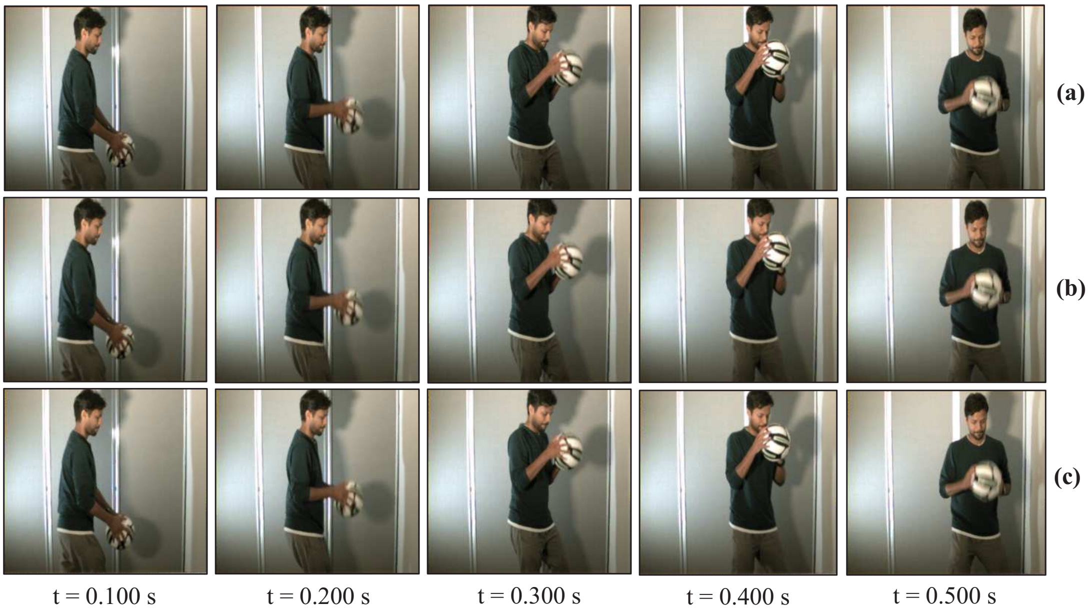

Figure 5.14: Reconstructed USB camera input image sequence on the plain background: (a) 640×480 input image, (b) 510×459 gray-code image without background subtraction, and (c) 510×459 gray-code image with background subtraction.

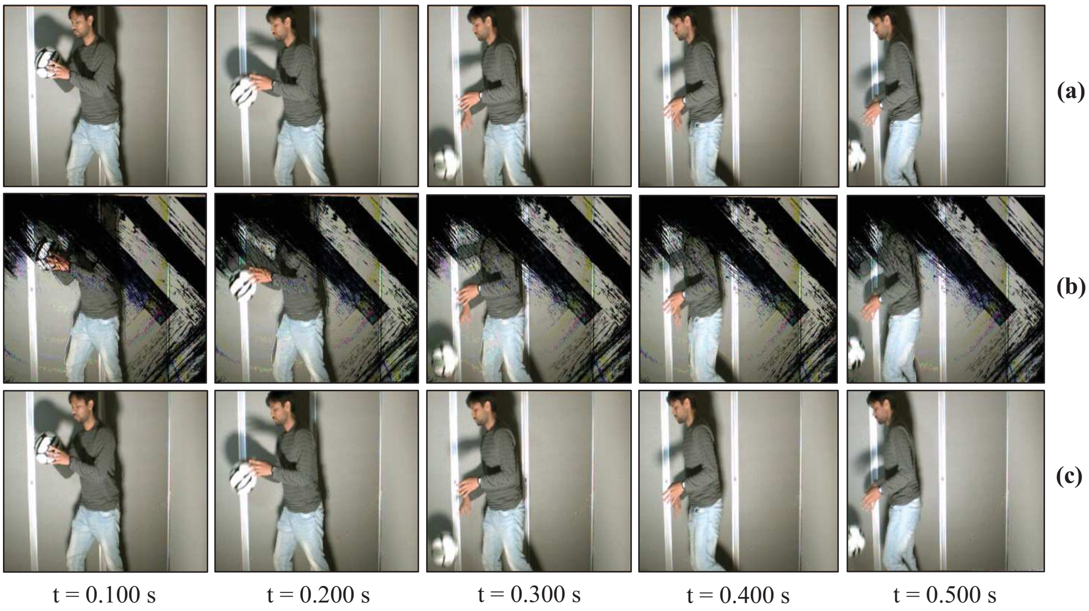

Figure 5.15: Reconstructed USB camera input image sequence on the pattern background: (a) 640×480 input image, (b) 510×459 binary-code image without background subtraction, and (c) 510×459 binary-code image with background subtraction.

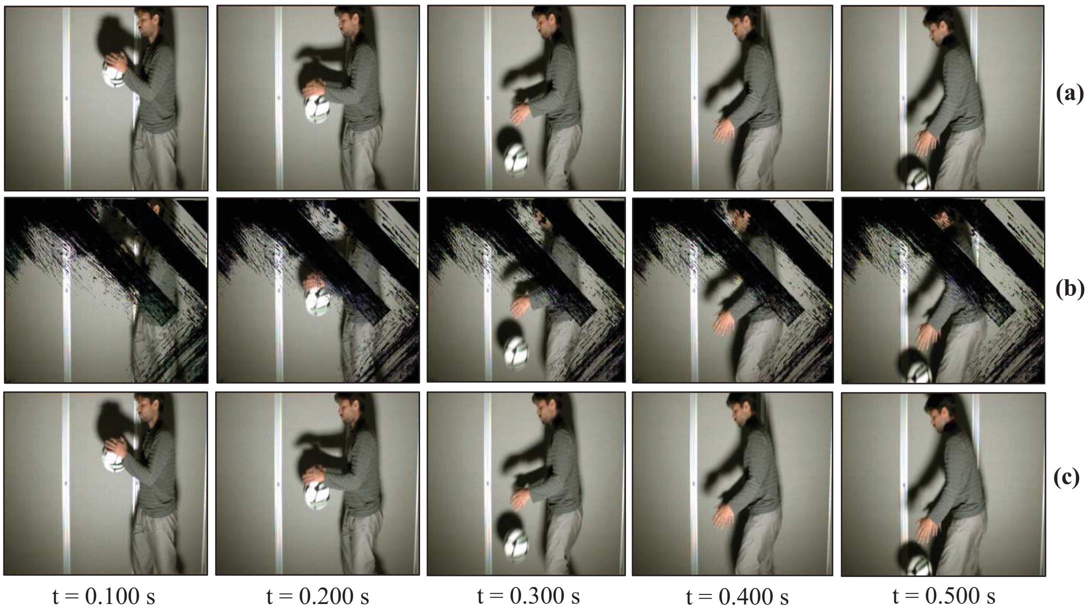

Figure 5.16: Reconstructed USB camera input image sequence on the pattern background: (a) 640×480 input image, (b) 510×459 gray-code image without background subtraction, and (c) 510×459 gray-code image with background subtraction.

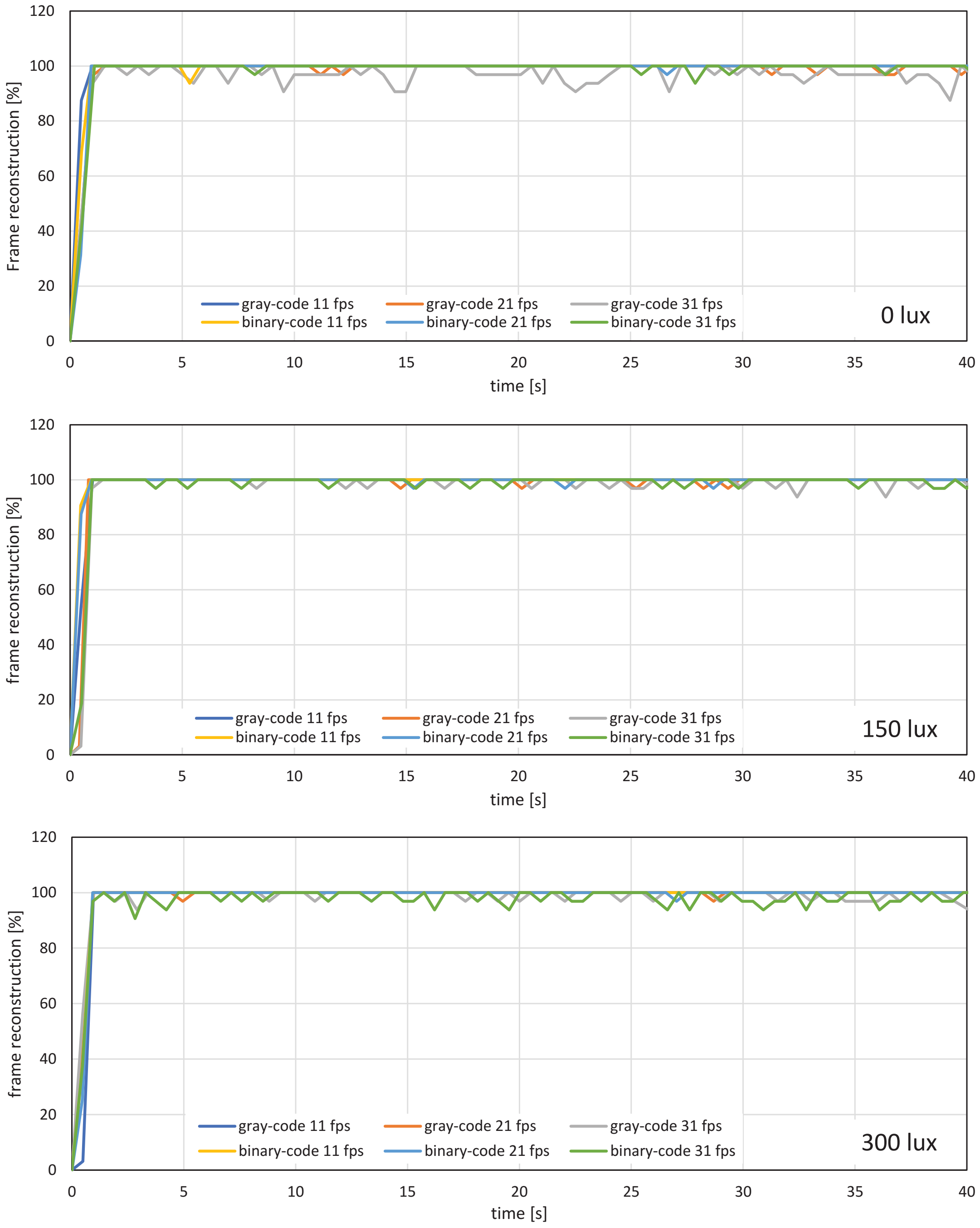

Figure 5.17: Frame reconstruction ratio when USB camera video is streaming on (a) plain background and (b) patterned background.

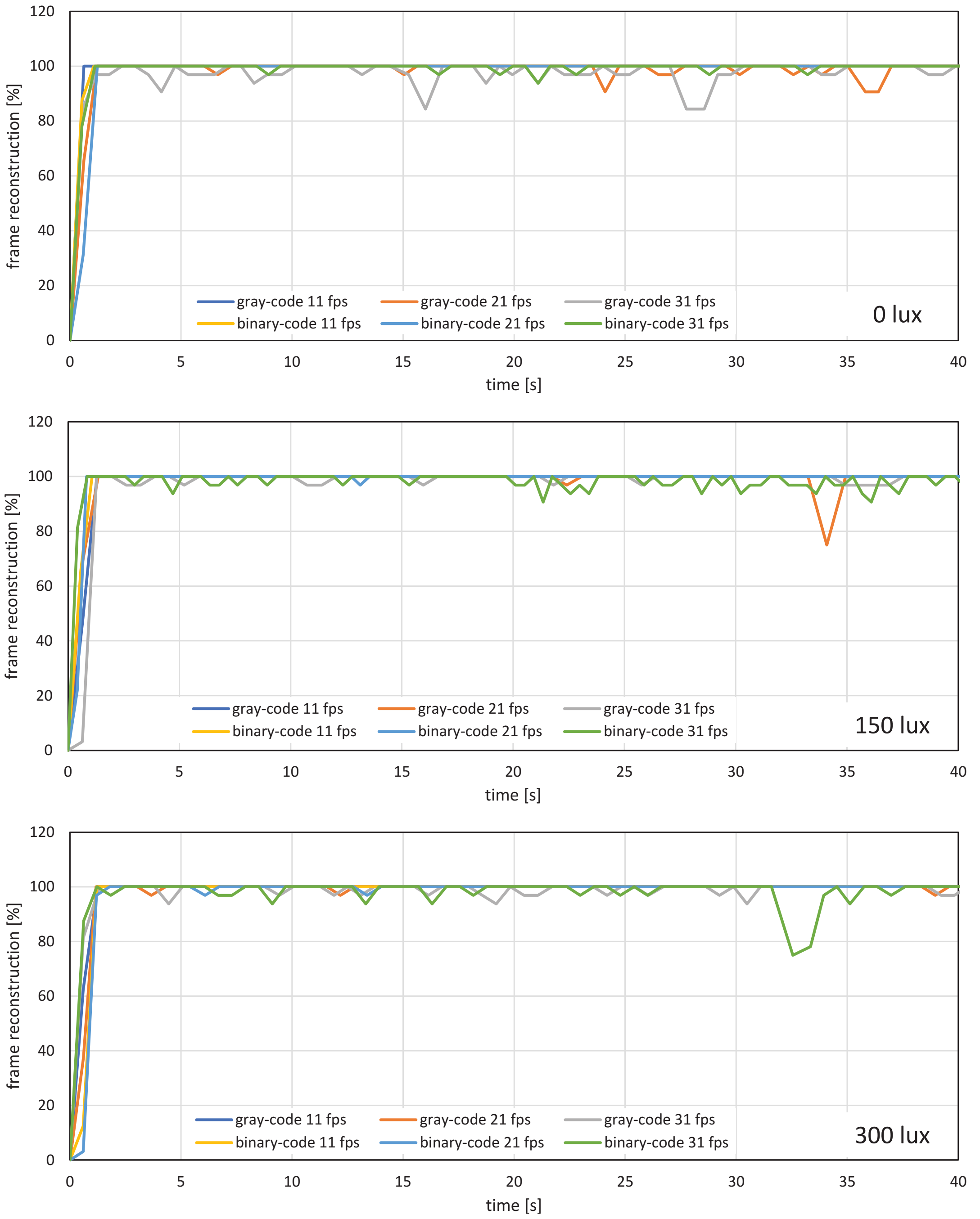

Figure 5.18: Frame reconstruction ratio when USB camera video is streaming on (a) plain background and (b) patterned background.

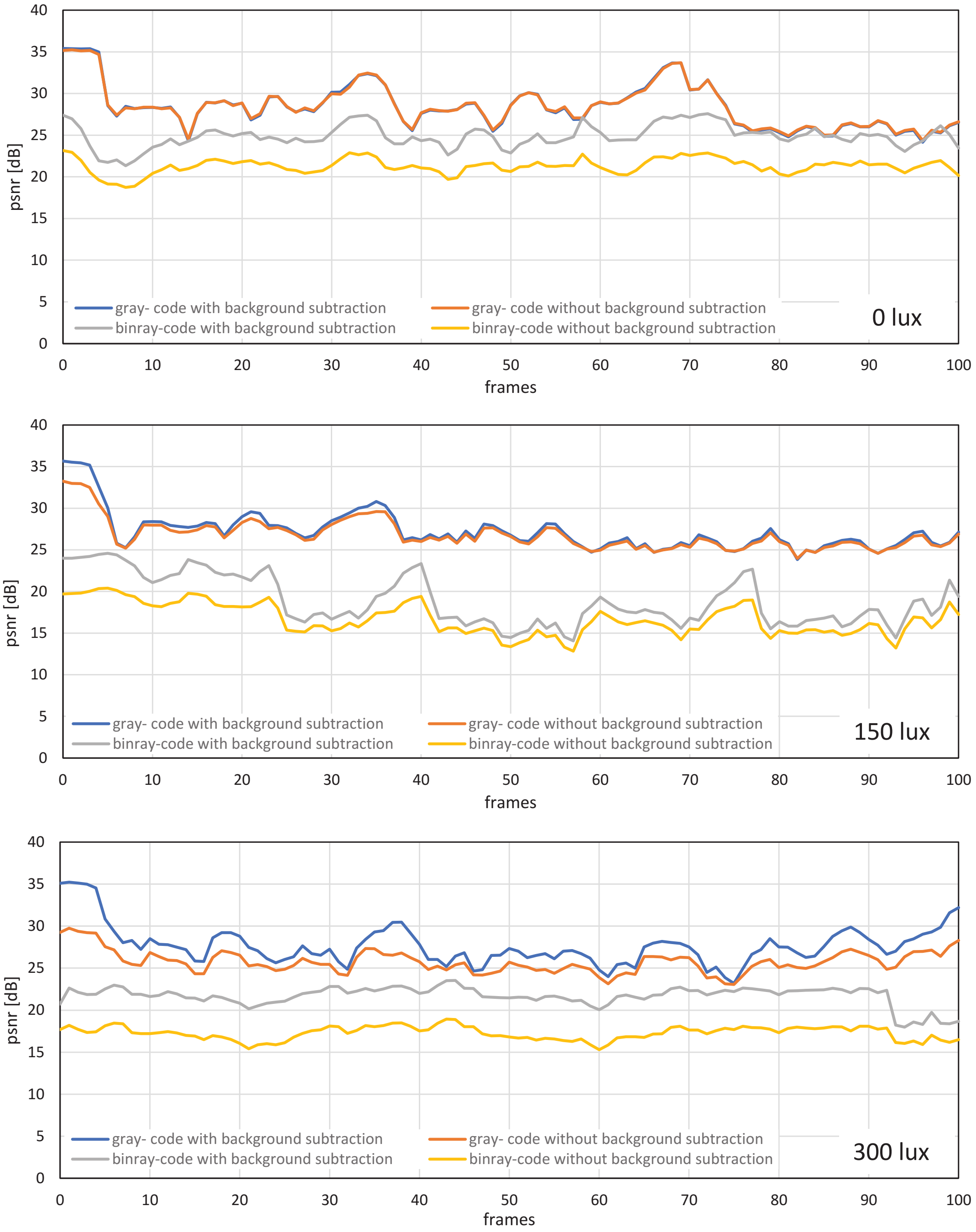

Figure 5.19

Figure 5.20: PSNRs when USB camera video sequence is streamed with pure-binary-code and gray-code images on the plain background.

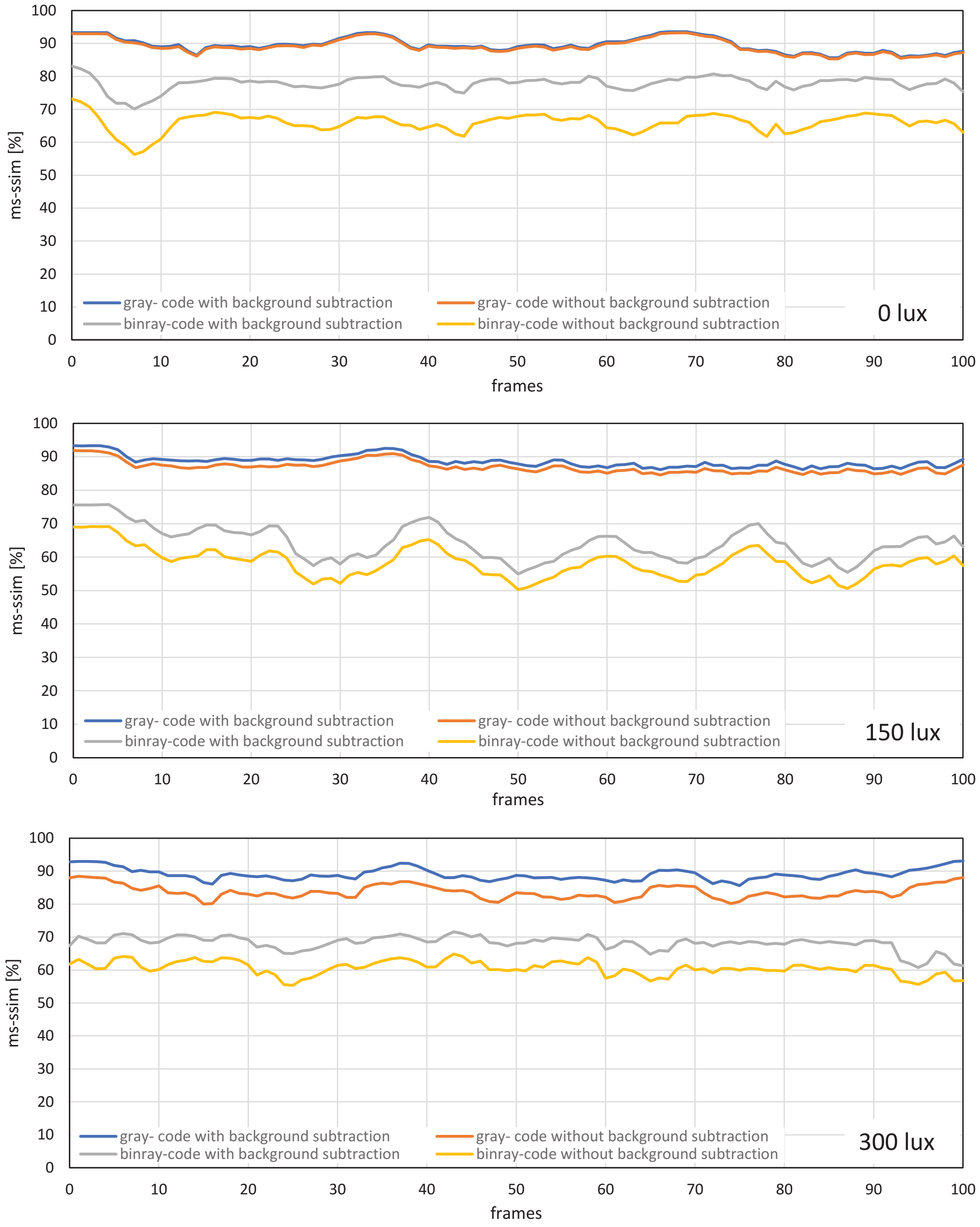

Figure 5.21: MS-SSIMs when USB camera video sequence is streamed with pure-binary-code and gray-code images on the plain background.

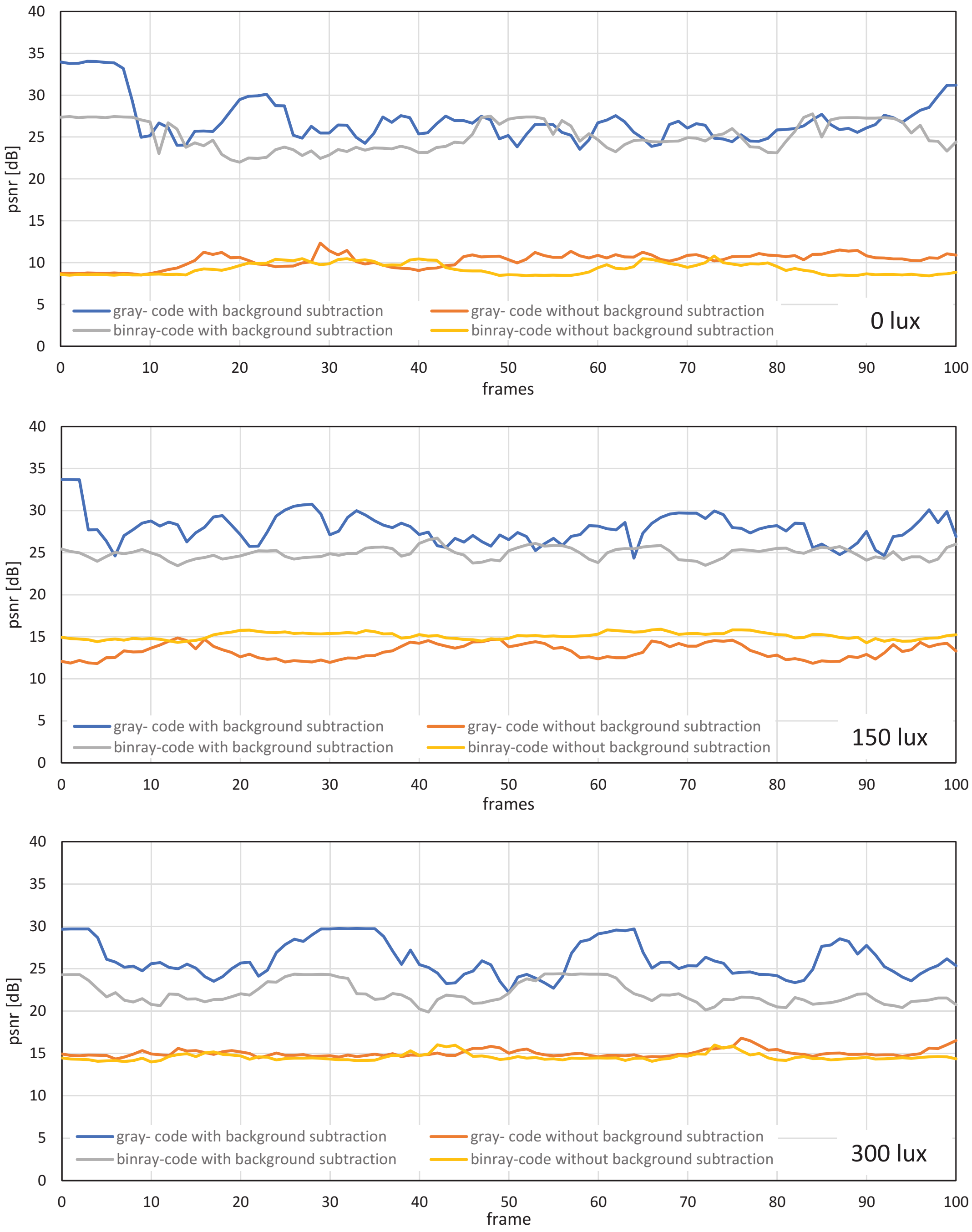

Figure 5.22: PSNR when USB camera video sequence is streamed with pure-binary-code and gray-code images on the patterned background.

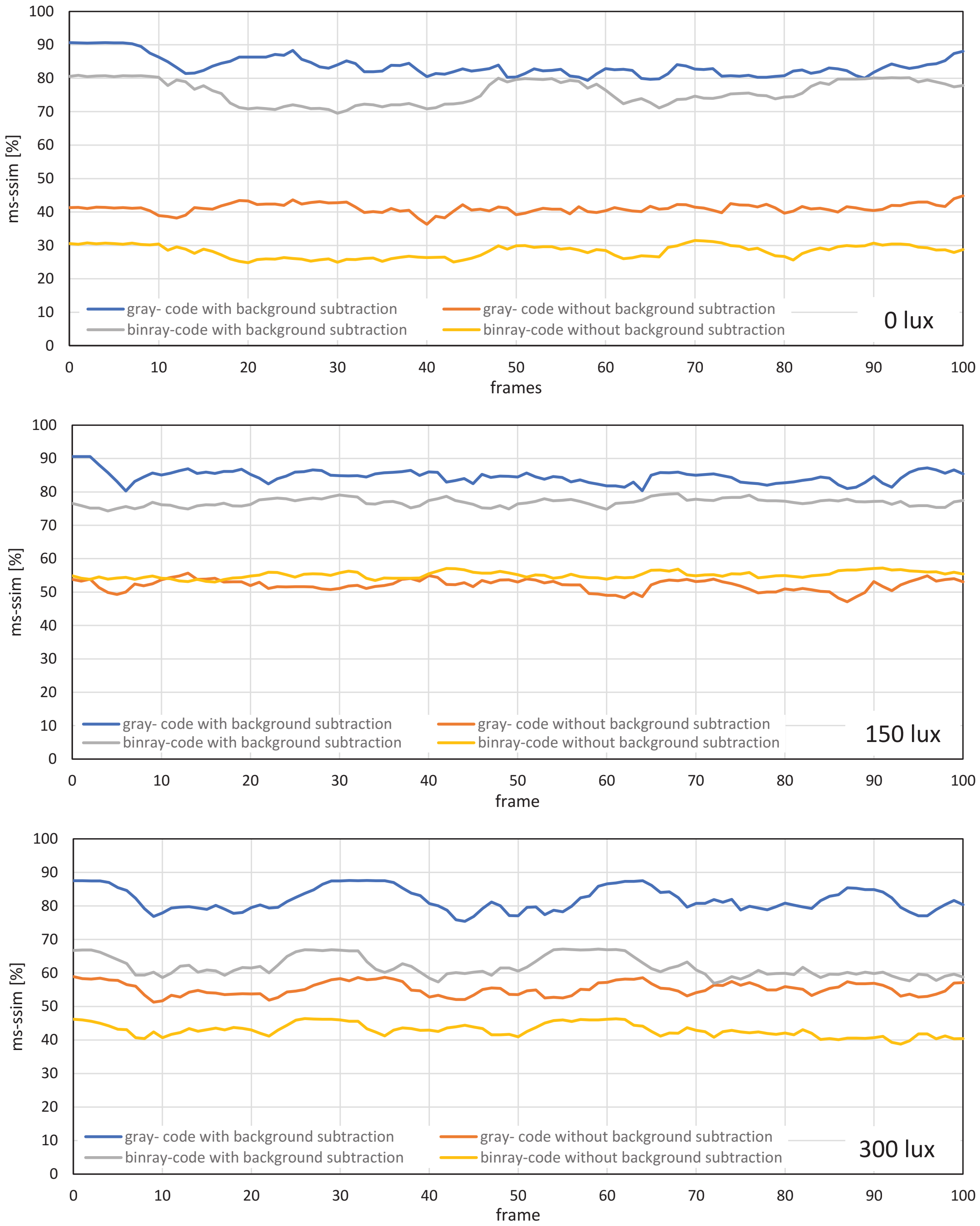

Figure 5.23: MS-SSIMs when USB camera video sequence is streamed with pure-binary-code and gray-code images on the patterned background.

5.2 Evaluating visual feedback-based synchronization HFR projector-camera VLC system

To evaluate the performance of the system we performed various experiments by streaming saved video and real-time universal serial bus (USB) camera video and reconstructing it using the VLC system. The HFR projector streamed 590×1,080 video at 60 fps, which is a combination of 590×1,060 gray-code images and 590×20 header information. This combined image is projected in a bit plane sequence as shown in Figure 5.25, where the duration of exposure for each bit-plane pattern is 331 μs. Therefore, the time required to project one frame is 24-bit × 331 μs, which is approximately 8,000 μs or 8 ms. Therefore, in 1 s, approximately 125 frames can be projected using our system; however, owing to the limitation of the HFR projector, we can transmit 590×1,080 image at maximum 60 fps. A 50-mm lens was mounted on the HFR camera, which was set to the same frame rate as that of the HFR projector (3,000 fps). The experimental setup is shown in Figure 5.24, where the distance between the HFR projector and screen was 950 mm. The projection display onto the screen was 448 × 415 mm. The distance between the HFR camera and screen was 1,130 mm to ensure that the overall area of the projected video on the screen was captured by the camera. For the proposed system: a stored video sequence was used for a single projector system, and live video streaming from two USB cameras was used to check the synchronization accuracy of the dual projector system. To check the robustness of the system, the indoor environment was illuminated with luminescence values of 0, 150, and 300 lx using an external light source. The details of the experimental hardware is specified in the Figure 5.1.

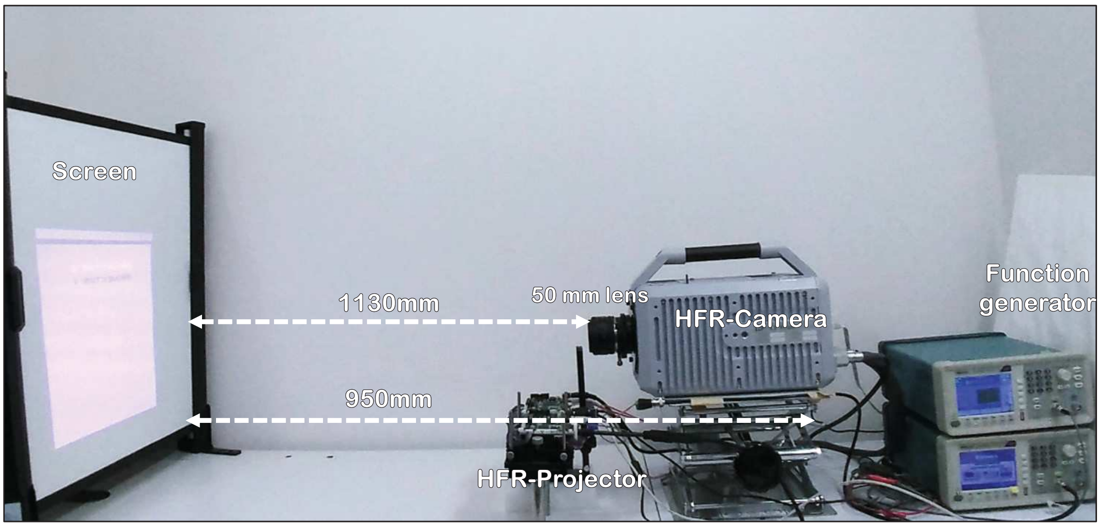

Figure 5.24: Overview of the HFR projector-camera system.

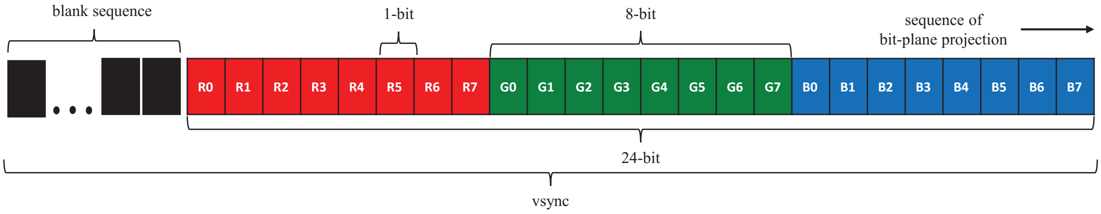

Figure 5.25: Bit-plane projection pattern for a single RGB image

Table 5.1: Experimental hardware with their specifications

Sr.No.	Equipment	Make	Specifications	Quantity
1	Receiver PC		Intel Core i7 @3.00GHz RAM : 64GB Windows 7 Enterprise Microsoft Visual 2015	1
2	Transmitter PC-1		Intel Core i3 @1.90GHz RAM : 8GB Windows 10 Home Microsoft Visual 2015	1
3	Transmitter PC-2		Intel Core i3 @1.90GHz RAM : 8GB Windows 10 Home Microsoft Visual 2015	1
4	HFR Camera	Photron SAX-2 monochrome	512x513 @ 3000 fps	1
5	HFR Projector	DLP lightcrafter 4500	Input:912x1140 @60fps, output: 912x1140 1-bit @ 3000/1500 fps	2
6	USB Camera	Ximea MQ003CG-CM	640x480 @ 60 fps	2

5.2.1 Real time video reconstruction of saved video

To evaluate the operation of the VLC system after successful synchronization using the visual feedback algorithm, an experiment was performed in which a stored video sequence was streamed in real-time. The selected video sequence was from the movie, "Big Buck Bunny" [92]. Initially, the pure-binary-code images of the 24-bit 1,920×1,080 RGB-color video sequence were gray coded and resized to 590×1,060 alongside the addition of 590×20 header information. The encoded resized image was projected in bit-plane or binary image sequences at 3,000 fps, and the HFR camera captured 512×512 images to reconstruct the output image with a resolution of 510×459 by combining all bit planes of the 24-bit RGB image sequentially. Figure 5.26a shows a high definition input image of 1,920×1,080 at 60 fps. Figure 5.26b contains the reconstructed images 510×459 using gray code without background subtraction. Figure 5.26c depicts the reconstructed images 510×459 using gray code with background subtraction. From the reconstructed images, we can deduce that there were no artifacts present when gray-code encoding was used.

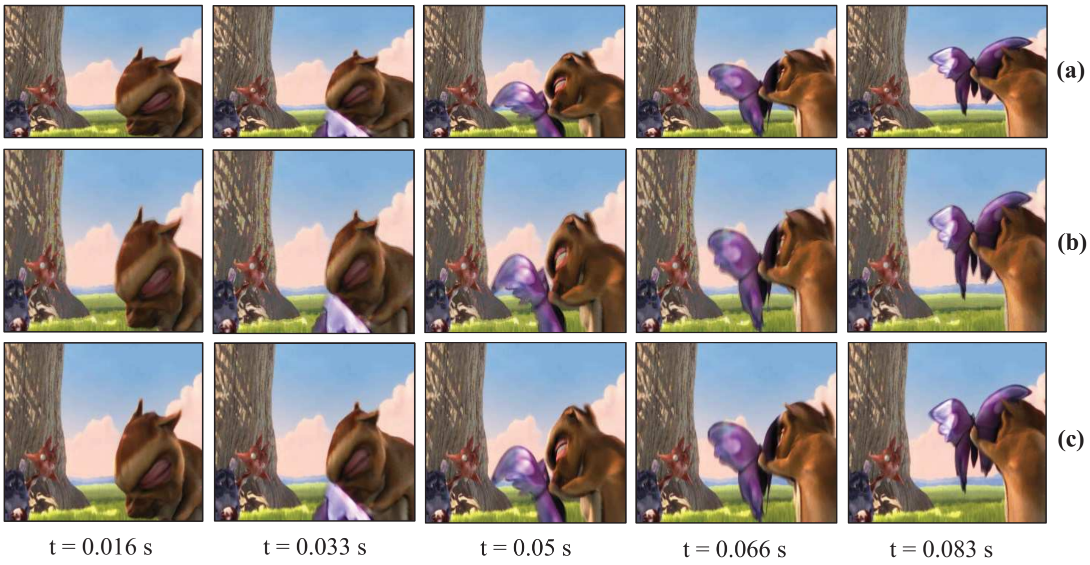

Figure 5.26: Reconstructed saved image sequence on a plain background: (a) 1,920×1,080 input image, (b) 510×459 gray-code image without background subtraction, and (c) 510×459 gray-code image with background subtraction.

Next, an experiment was conducted to measure the image quality analysis and performance of the system by sending the saved video at 60 fps, which was projected at 3,000 fps under different on-screen luminescence conditions of 0, 150, and 300 lx, and images were captured at 3,000 fps at different exposure times, i.e., 1/3,015, 1/8,000, and 1/12,500. The results of the image-quality analysis of hundred reconstructed images with respect to their original images, are shown in Figure 5.27 and Figure 5.28. From the graph shown in Figure 5.27 and Figure 5.28 the PSNR and MS-SSIM values indicate that the image quality was better when captured at an exposure of 1/8,000 than those at 1/12,500 and 1/3,015. However, the background subtraction performed at every frame helped improve the image quality at various HFR camera exposure times. Figure 5.29 shows the performance of the system based on the number of frames reconstructed at the receiver. A duration of 40 s was observed, and the number of frames was monitored, as shown in Figure 5.29. The frame reconstruction ratios were almost 100% for 0 lx, whereas for 150 and 300 lx, the frame reconstruction was nearly 100% with small losses. The experimental results indicate that the HFR projector and HFR cameras were synchronized; otherwise, the frame reconstruction would not be possible, and we would not be able to reconstruct the video sequence in real time at 60 fps.

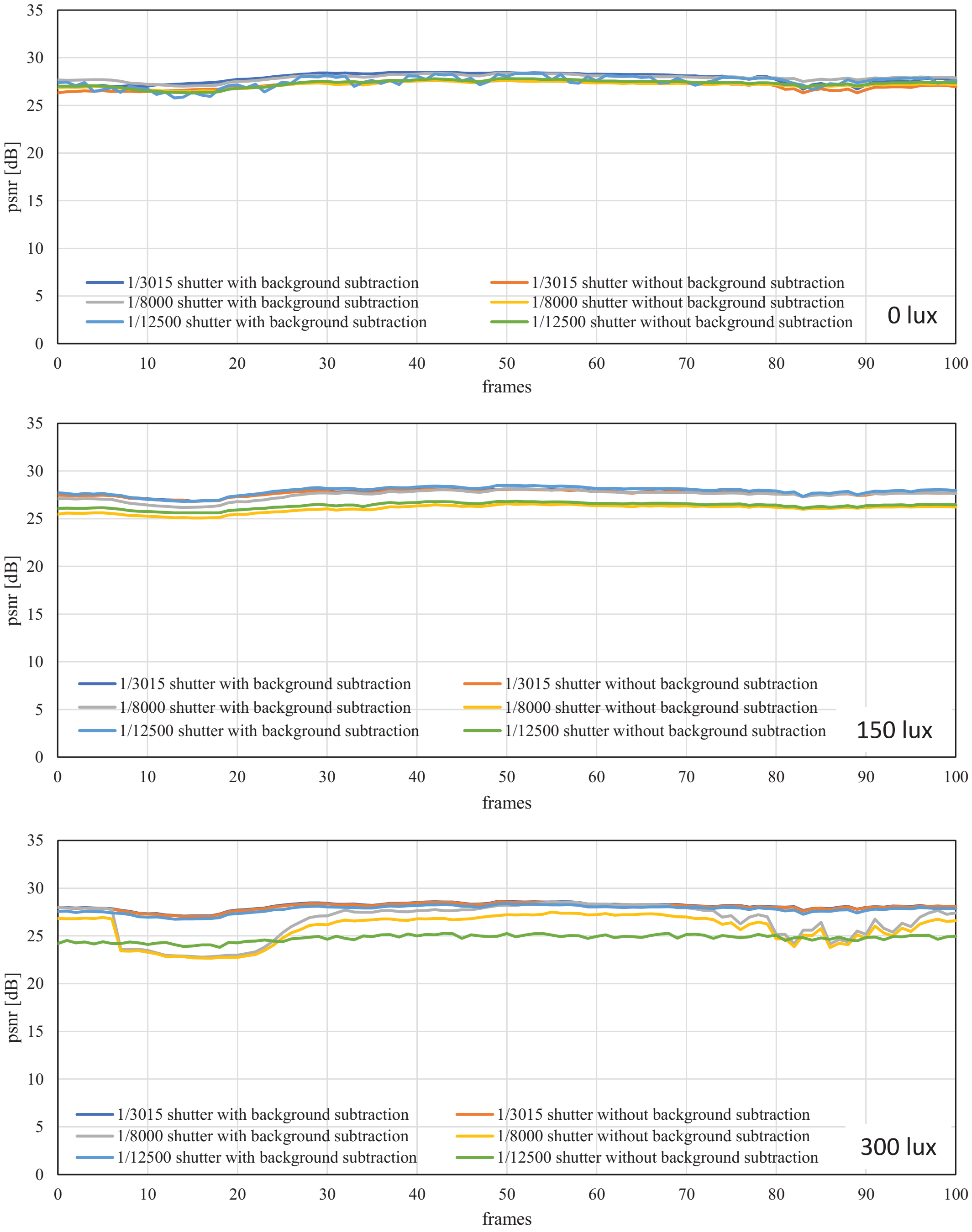

Figure 5.27: PSNRs when a stored video sequence is streamed with pure-binary-code and gray-code images on patterned background.

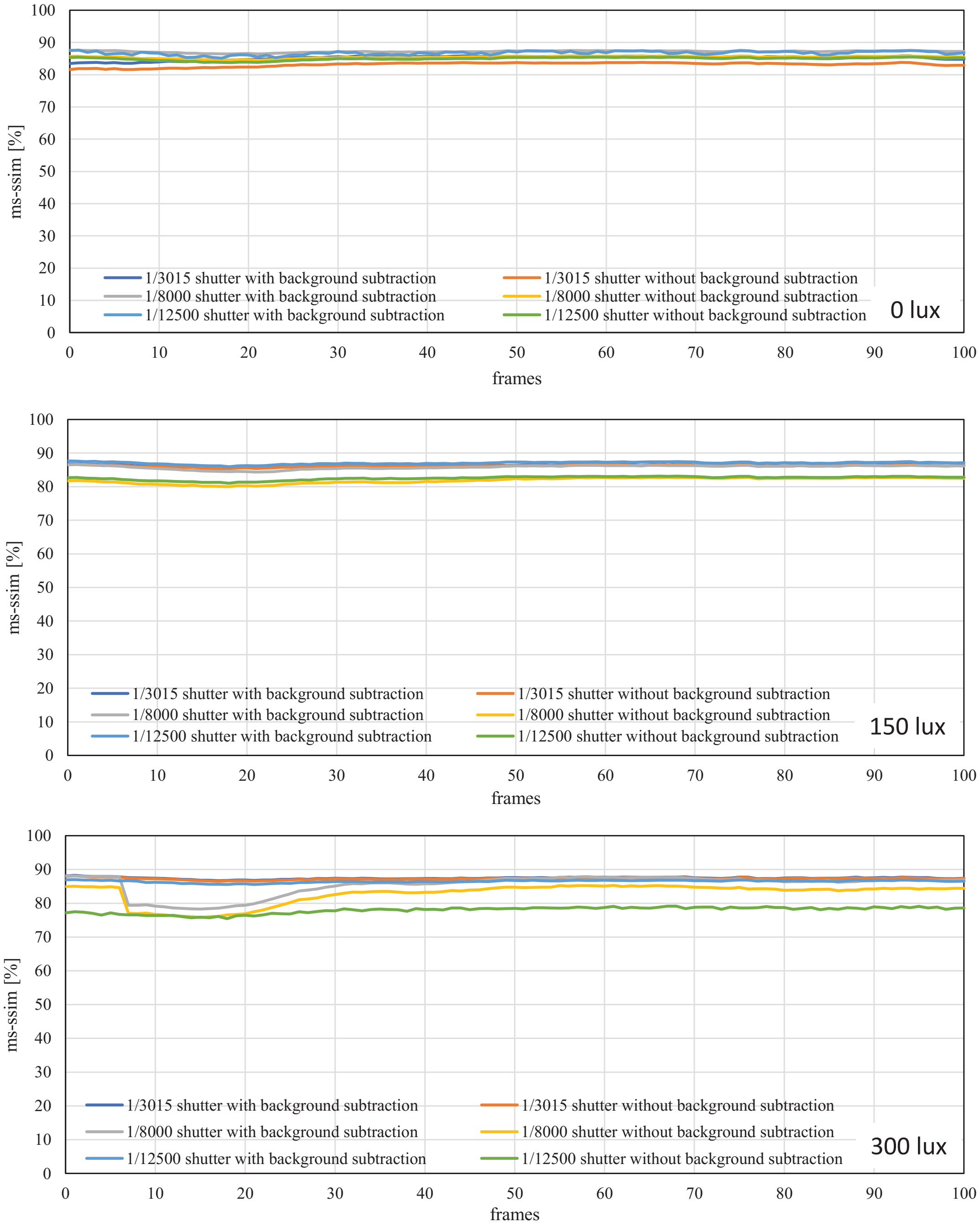

Figure 5.28: MS-SSIMs when a stored video sequence is streamed with pure-binary-code and gray-code images on patterned background.

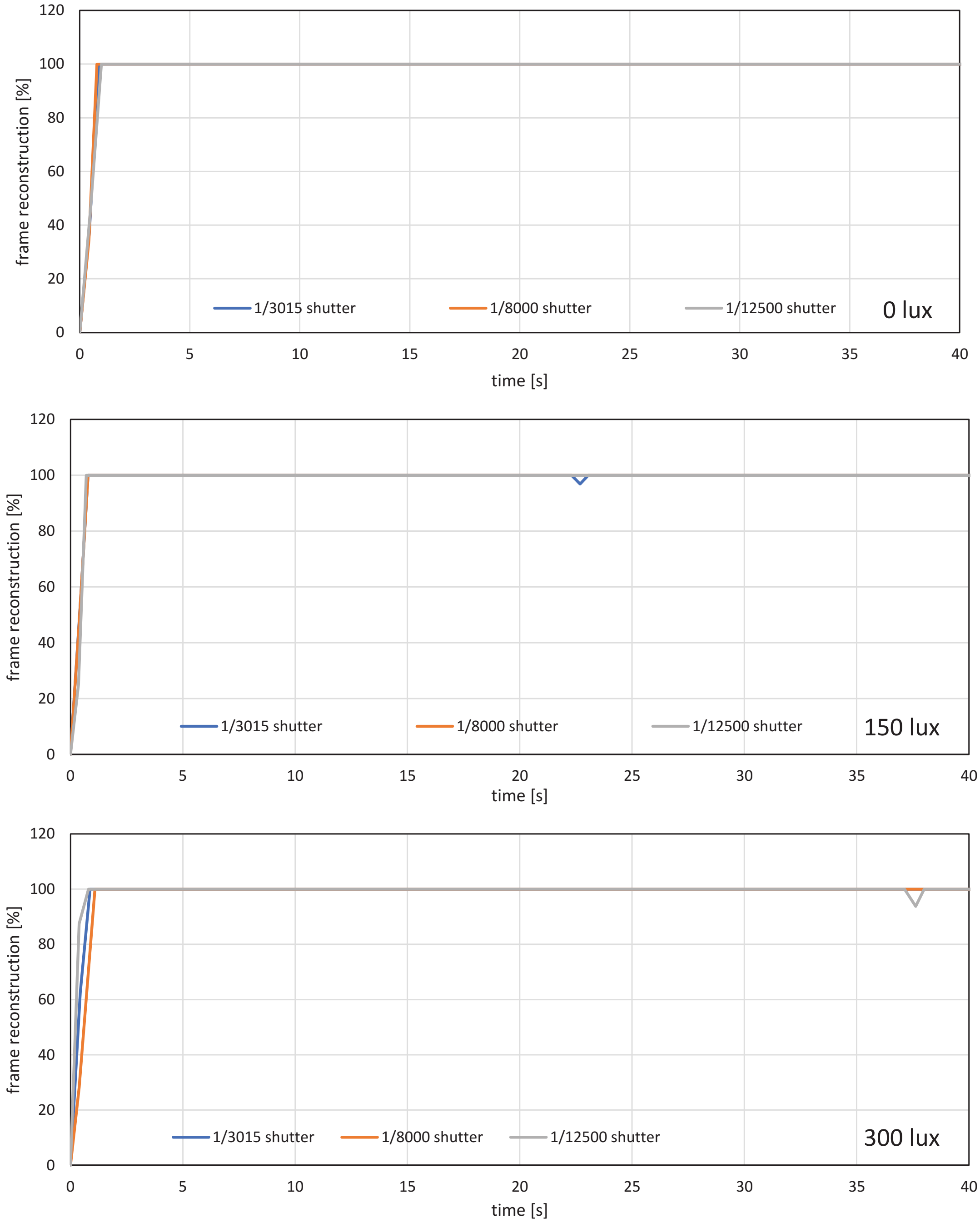

Figure 5.29: Frame reconstruction ratio when a stored movie is streaming.

5.2.2 Dual HFR projector synchronization with HFR camera and real-time video reconstruction of two USB camera live video

The experimental setup for the two projectors is shown in Figure 5.30, where the dual projectors are maintained such that the projection area overlaps. The distance between the screen and both HFR projectors was kept the same at 950 mm, and the HFR camera was set at a distance of 1,130 mm with a 50-mm mounted lens. The experiment scene is shown in Figure 5.31. In this experiment, the input video sequence was streamed from two USB cameras (XIMEA, MQ003CG-CM) in 24-bit color with a resolution of 640×480 at 60 fps for transmission, and both cameras were connected to two PCs. The experiment scene comprised a person throwing a football on the floor. In this experiment, HFR projector 2 was set to 180° out-of-phase with respect to HFR projector 1, and both were set to 1,500 fps. The bit-plane projection of the image sequence was the same as that in Figure 5.25. The HFR camera was kept at 3,000 fps that is double the projection frame rate, which captured the images of each projector alternately and reconstructed both videos at 60 fps. In Figure 5.32, the two HFR projector input image sequences of 640×480 at 60 fps are shown. Figure 5.32b depicts the reconstructed 510×459 images using gray code without background subtraction. Figure 5.32c shows the reconstructed images 510×459 using gray code with background subtraction. The sequences were reconstructed alternately from the image sequence projected using HFR projectors 1 and 2.

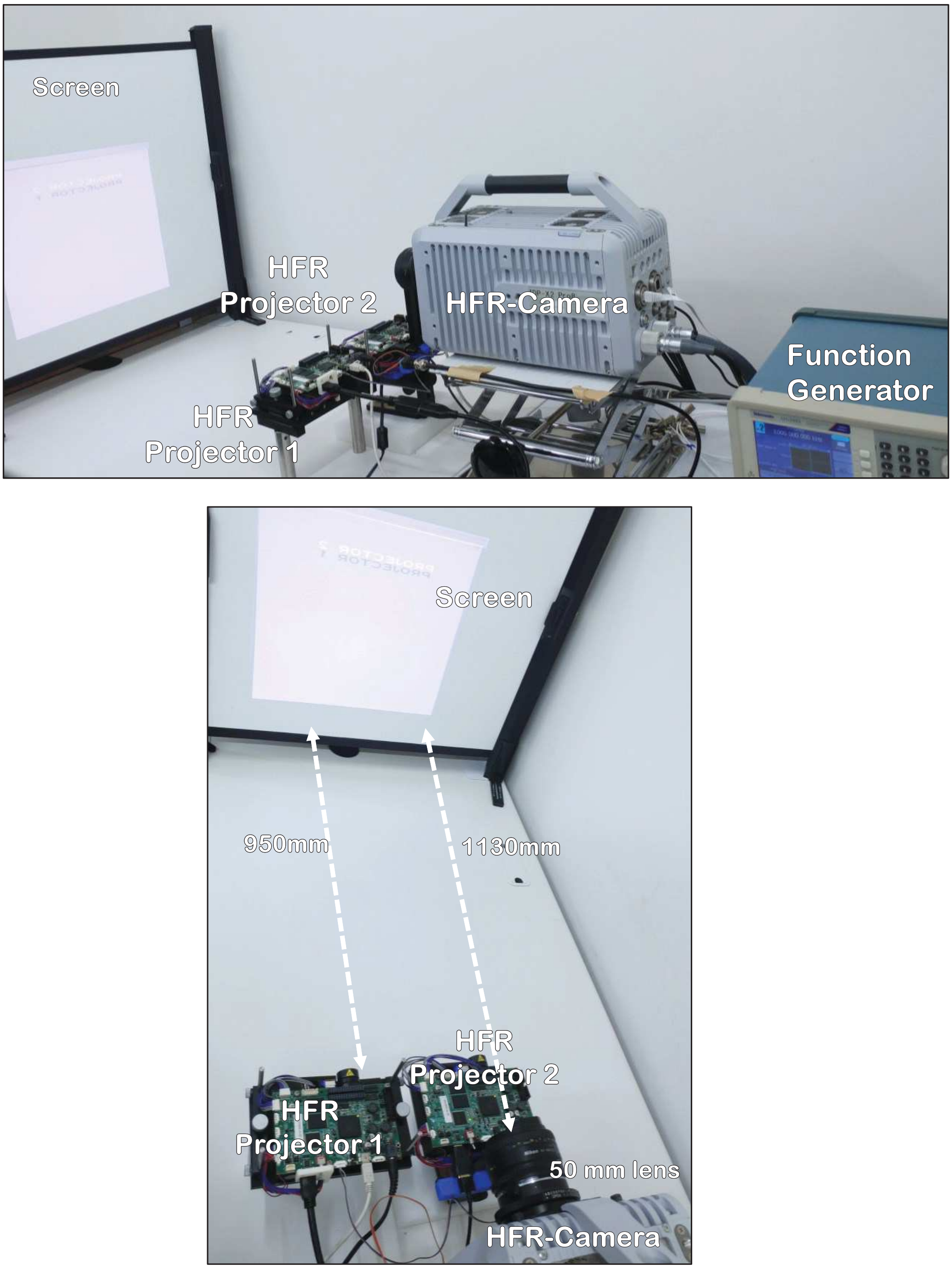

Figure 5.30: Experimental setup for two HFR projector system

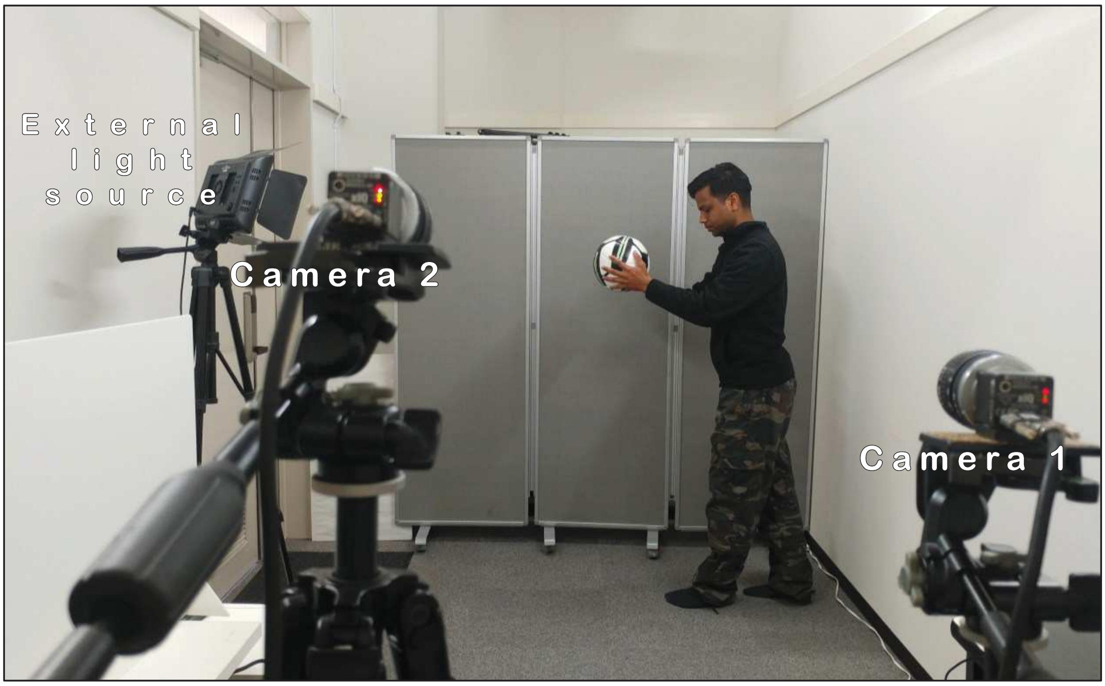

Figure 5.31: Reconstructed USB camera input image sequence : 510×459 binary-code image without background subtraction.

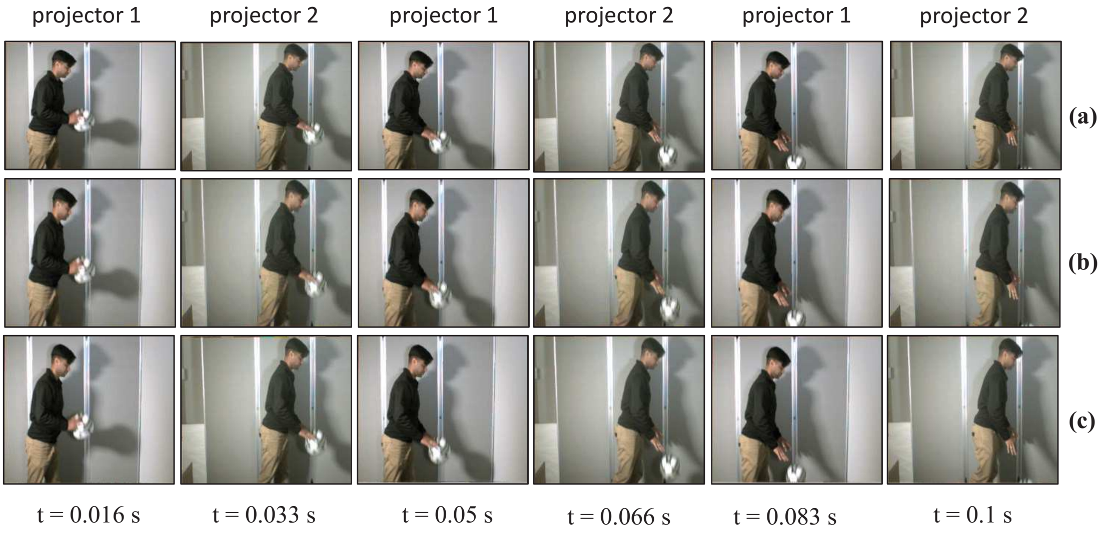

Figure 5.32: Reconstructed USB camera input image sequence : (a) 640×480 input image, (b) 510×459 binary-code image without background subtraction, and (c) 510×459 binary-code image with background subtraction.

The image quality analysis and performance of the two projector systems were evaluated by projecting a 60 fps video at 3,000 fps under different on-screen luminescence conditions, i.e., 0, 150, and 300 lx, and the images were captured at 3,000 fps with different exposure times, i.e., 1/3,015, 1/8,000, and 1/12,500. Figures 5.33, 5.35 and 5.34, 5.36 show that the values of PSNRs and MS-SSIMs were similar, but the best result was observed for exposure 1/3,015 at 0 lux. However, the values of MS-SSIM are more promising than the PSNR values because they represent the image quality of the system. Figure 5.37 and Figure 5.38 shows the performance of the frames reconstructed from each projector system reflecting the number of frames reconstructed at the receiver corresponding to each projector. Figure 5.37 and Figure 5.38 shows that the live USB streaming led to few losses in the frame during reconstruction but were not very significant, and the system could reconstruct video sequence in real-time at 60 fps. The results indicate that multiple projector synchronization was possible with the HFR camera, and the overall bandwidth of the system was utilized.

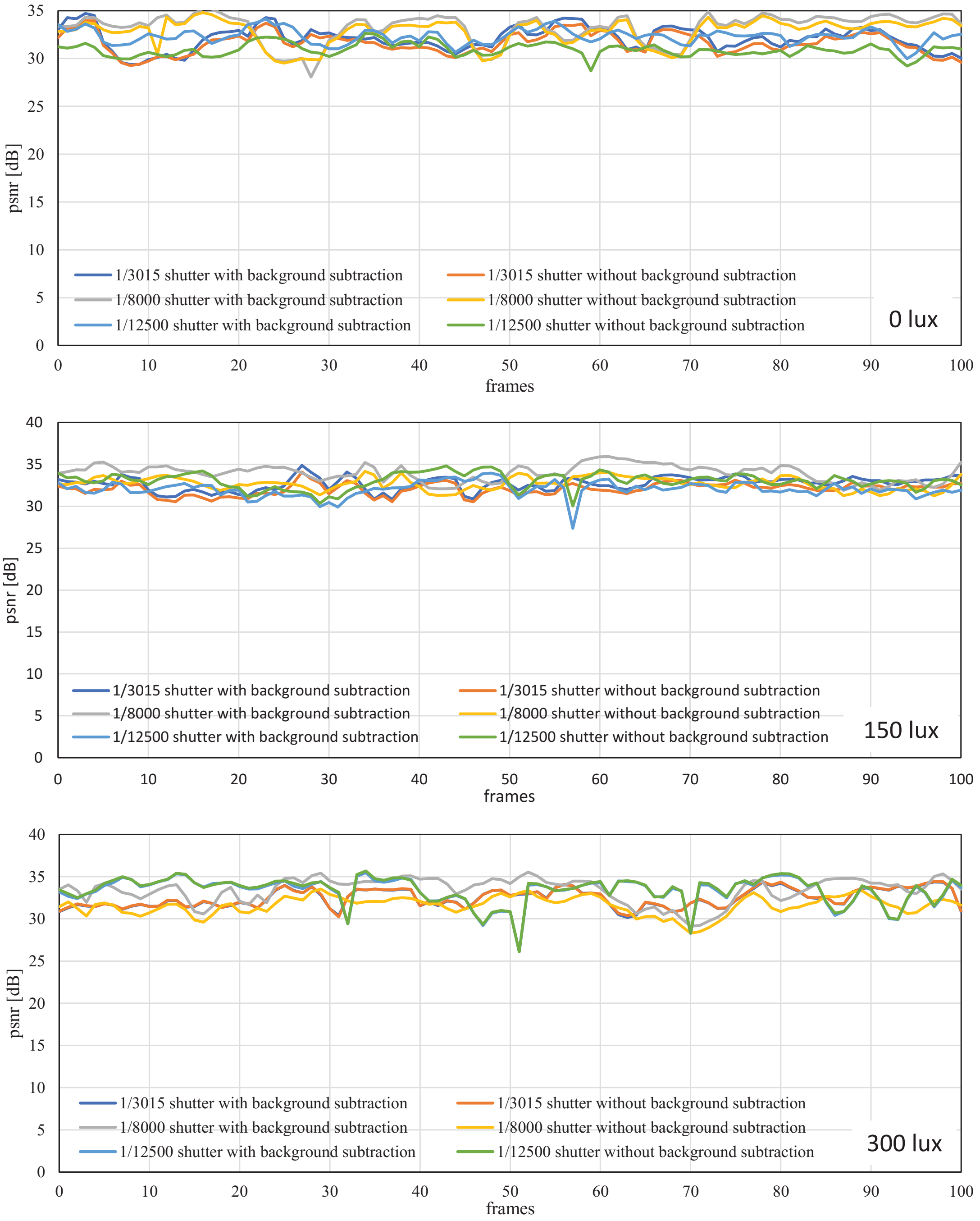

Figure 5.33: PSNRs when the USB camera video sequence is streamed through HFR projector-1.

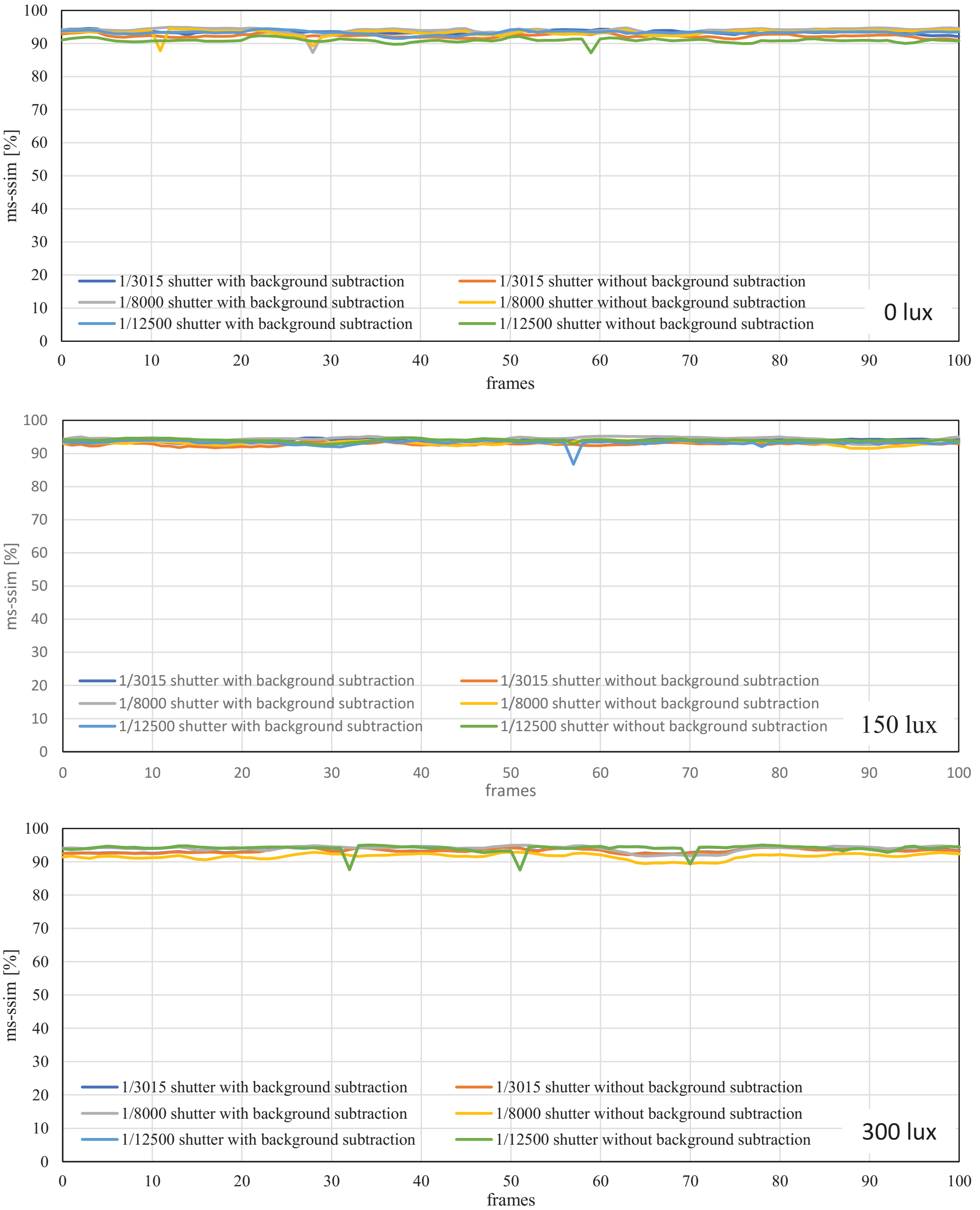

Figure 5.34: MS-SSIMs when the USB camera video sequence is streamed through HFR projector-1.

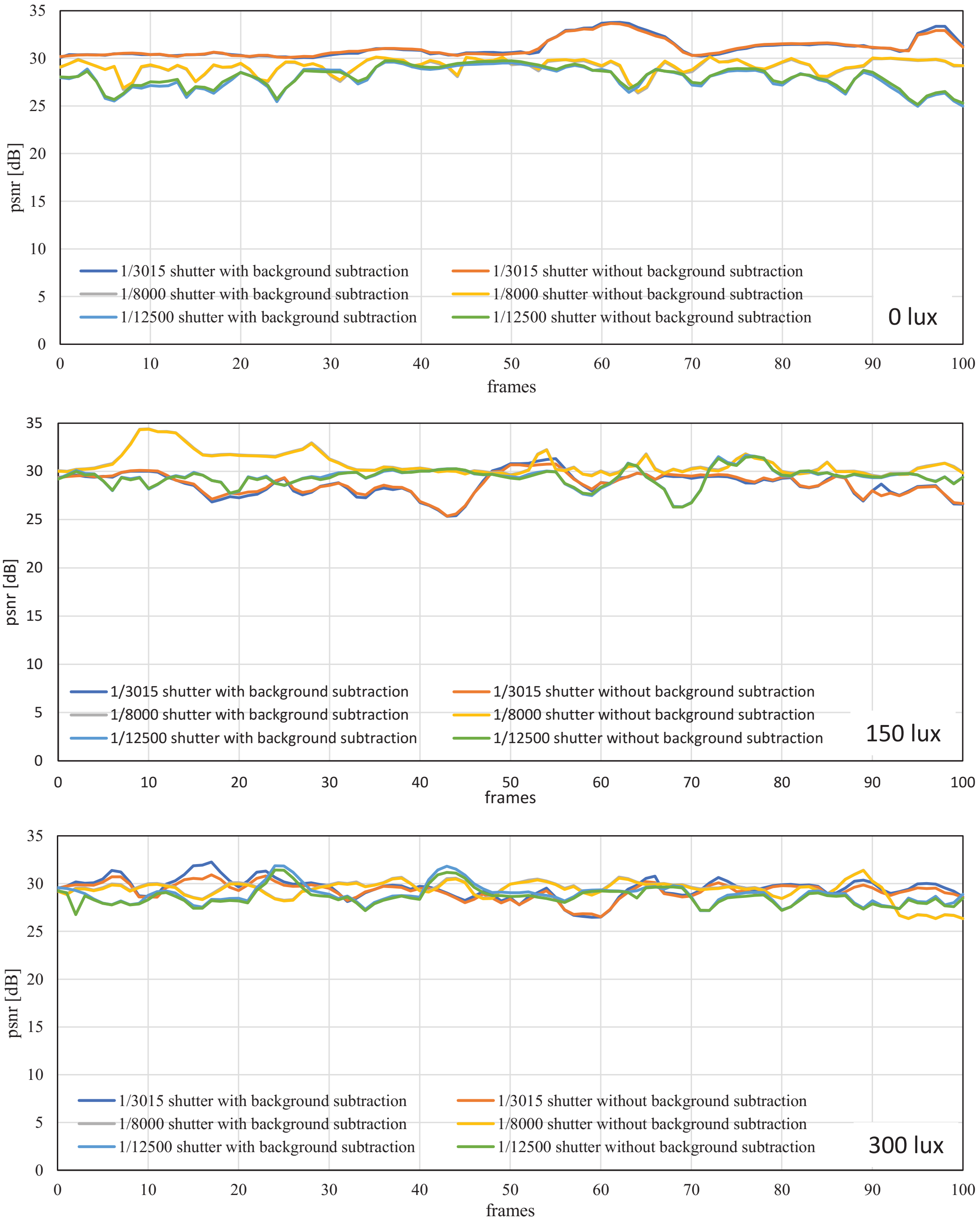

Figure 5.35: PSNRs when the USB camera video sequence is streamed through HFR projector-2.

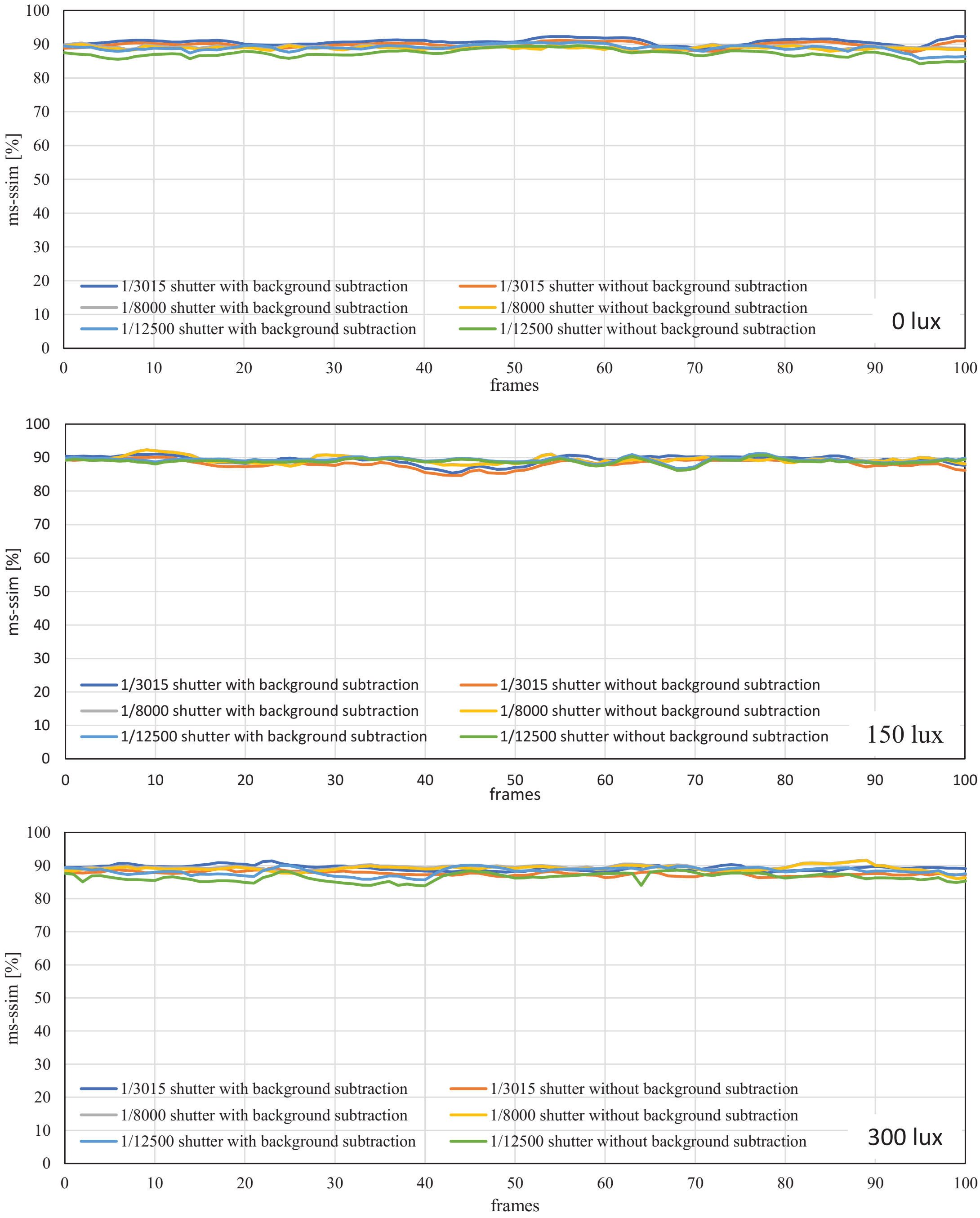

Figure 5.36: MS-SSIMs when the USB camera video sequence is streamed through HFR projector-2.

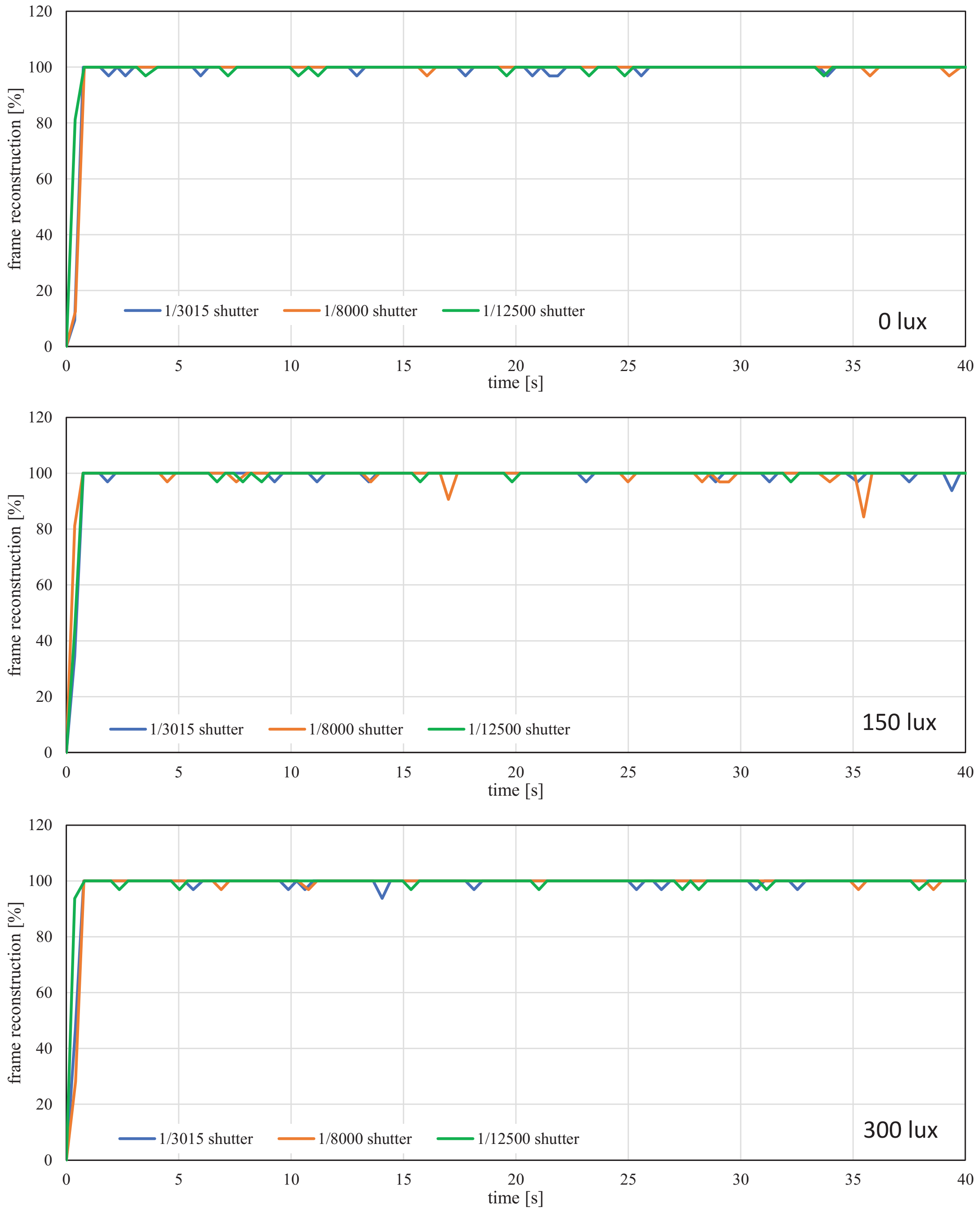

Figure 5.37: Frame reconstruction ratio from HFR projector 1.

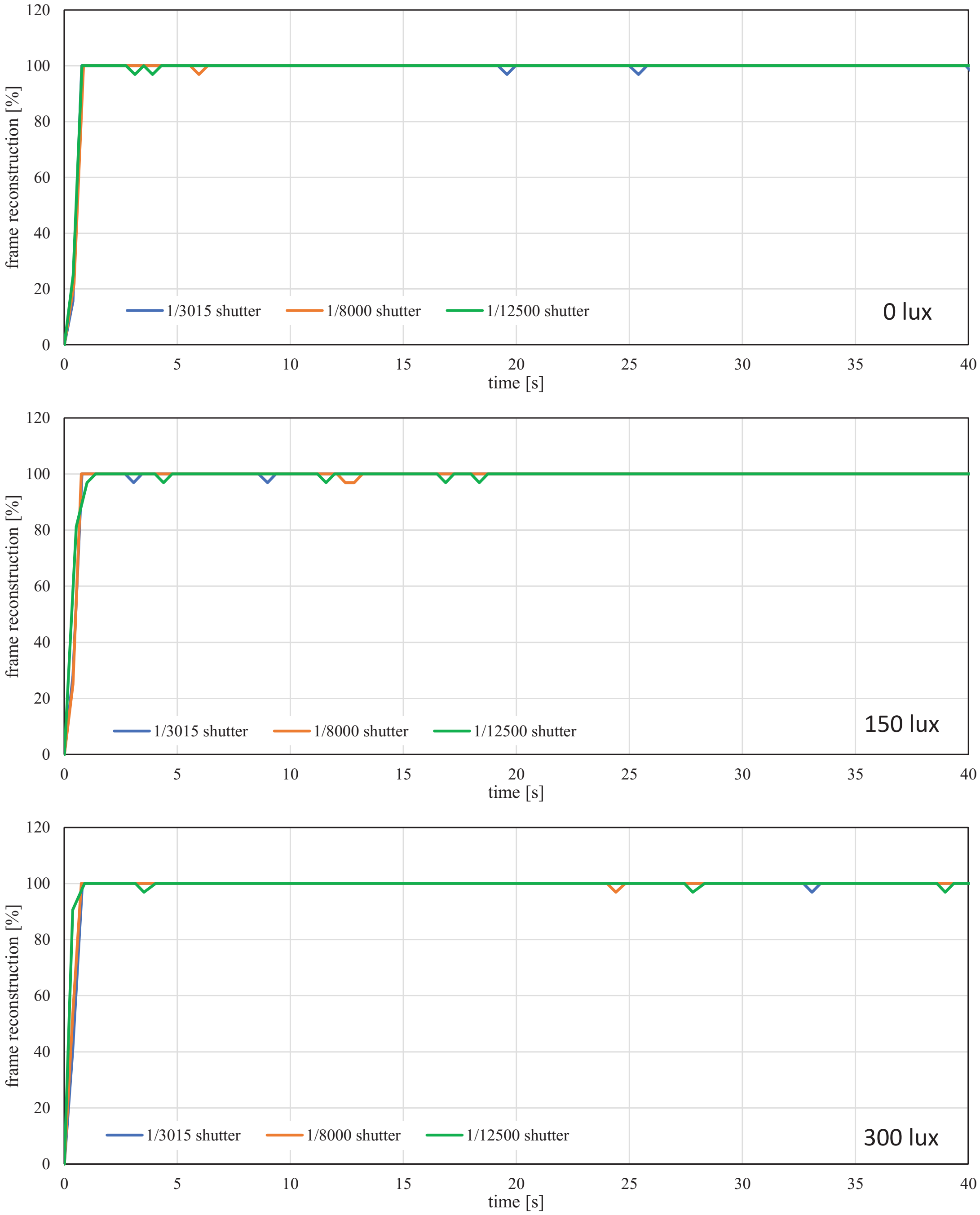

Figure 5.38: frame reconstruction ratio from HFR projector 2.

Chapter 6

Conclusion

In this study, we developed a real-time video broadcasting system using VLC that can transmit saved and real-time USB camera videos through an HFR projector, operating at 1,041 fps, and reconstruct the output color video using a monochrome HFR-camera at 3,125 fps via software-based synchronization. The ambiguity occurring at gradients with pixels having a higher frequency component was removed using gray-code-based encoding over pure-binary-code-based encoding of transmitted video was evaluated. The use of thresholding-based background subtraction is efficient for eliminating the effect of ambient light and patterned background. Software-based synchronization is used to overcome the synchronization error between the HFR projector and HFR camera by considering the Nyquist sampling theorem. Various experiments were conducted for real-time video broadcasting systems to evaluate the frame reconstruction at different fps and lux, wherein the frame loss was slightly increased with an increase in the frame rate and lux. The image quality of the reconstructed image was reduced as the luminescence of the ambient was increased, which was verified by comparing the image quality metrics, PSNR and MS-SSIM. The background subtraction method was found to be more effective for the patterned background than the plain background. However, the system has limited bandwidth due to software-based synchronization, data redundancy, and long-term inconsistency issues which can be rectified by synchronizing the phase of operating frequency of the HFR projector-camera system using a novel visual feedback-based algorithm. The performance of visual feedback-based algorithm was evaluated by streaming real-time video using the HFR projector–camera-based VLC system. The experimental results show that synchronization can be achieved at a high frame rate, and the system is robust to ambient light and can work on a wide range of exposure times. The background subtraction method increased the image quality of the reconstructed image under different ambient light conditions. It was observed that the frame loss was slightly increased with an increase in the frame rate and lux. The HFR camera and HFR projector system bandwidth were not fully utilized at 3,000 fps when a single projector system was used because the system could reconstruct a 60 fps streaming video at nearly 60 fps. Therefore, the dual projector system proved promising, and a full bandwidth of approximately 120 fps was utilized as the dual projector system distributed the computational load of one PC to two. Overall, the images reconstructed using the dual projector had better quality, and the system can be expanded to multiple projectors. The only constraint of the dual projector system is that HFR projector 2 should be triggered by HFR projector 1.

Bibliography

[1] Watanabe, Y. ; Komuro, T.; Ishikawa, M. 955-fps real-time shape measurement of a moving/deforming object using high-speed vision for numerous-point analysis. In Proceedings of the IEEE International Conference on Robotics and Automation, Roma, 2007; pp. 3192-3197.

[2] Ishii, I.; Taniguchi, T.; Sukenobe, R.; Yamamoto, K. Development of high-speed and real-time vision platform, H3 vision. In Proceedings of the IEEE/RSJ International Conference on Intelligent Robots and Systems (IROS), 2009; pp. 3671–3678.

[3] Ishii, I.; Tatebe, T.; Gu, Q.; Moriue, Y.; Takaki, T.; Tajima, K. 2000 fps real-time vision system with high-frame-rate video recording. In Proceedings of the IEEE International Conference on Robotics and Automation (ICRA), 2010; pp. 1536–1541.

[4] Sharma, A.; Shimasaki, K.; Gu, Q.; Chen, J.; Aoyama, T.; Takaki, T.; Ishii, I.; Tamura, K.; Tajima, K. Super high-speed vision platform that can process 1024x1024 images in real time at 12500 fps. In Proceedings of the IEEE/SICE International Symposium on System Integration, pp.544-549; 2016.

[5] Yamazaki, T.; Katayama, H.; Uehara, S.; Nose, A.; Kobayashi, M.; Shida, S.; Odahara, M.; Takamiya, K.; Hisamatsu, Y.; Matsumoto, S.; Miyashita, L.; Watanabe, Y.; Izawa, T.; Muramatsu, Y.; Ishikawa, M. A 1ms high-speed vision chip with 3D-stacked 140GOPS column-parallel PEs for spatio-temporal image processing. In Proceedings of the IEEE International Solid-State Circuits Conference (ISSCC), 2017; pp. 82–83.

[6] Ishii, I.; Taniguchi, T.; Yamamoto, K.; Takaki, T. High-frame-rate optical flow system. *IEEE Trans. Circ. Sys. Video Tech.*, **2012**, *22*, 105-112.

[7] Gu, Q.; Nakamura, N.; Aoyama, T.; Takaki, T.; Ishii, I. A full-pixel optical flow system using a GPU-based high-frame-rate vision. In Proceedings of the 2015 Conference on Advances In Robotics, Goa, India — 02-04 July, 2015; Article 52.

[8] Ishii, I.; Tatebe, T.; Gu, Q.; Takaki, T. Color-histogram-based tracking at 2000 fps. *J. Electronic Imaging*, **2012**, *21*, pp. 013010-1.

[9] Gu, Q.; Raut, S.; Okumura, K.; Aoyama, T.; Takaki, T.; Ishii, I. Real-time image mosaicing system using a high-frame-rate video sequence. *J. Robot. Mechat.*, **2015**, *27* , pp. 204–215.

[10] Jiang, M.; Aoyama, T.; Takaki, T.; Ishii, I. Pixel-level and robust vibration source sensing in high-frame-rate video analysis. *Sensors* **2016**, *16*.

[11] Jiang, M.; Gu, Q.; Aoyama, T.; Takaki, T.; Ishii, I. Real-time vibration source tracking using high-speed vision. *IEEE Sensors J.* **2017**, *17*, 1513–1527.

[12] Ueno, T.; Gu, Q.; Aoyama, T.; Takaki, T.; Ishii, I.; Kawahara, T. Motion-blur-free microscopic video shooting based on frame-by-frame intermittent tracking. In Proceedings of the IEEE Conference on Automation Science and Engineering, Gothenburg, Sweden, 24–28 Aug. 2015; pp. 837–842.

[13] Hayakawa, T.; Watanabe, T.; Ishikawa, M. Real-time high-speed motion blur compensation system based on back-and-forth motion control of galvanometer mirror. *Opt. Express,* **2015**, *23*, 31648–31661.

[14] Hayakawa, T.; Ishikawa, M. Development of motion-blur-compensated high-speed moving visual inspection vehicle for tunnels. *Int. J. Civ. Struct. Eng. Res.* **2016**, *5*, 151–155.

[15] Inoue, M.; Gu, Q.; Jiang, M.; Takaki, T.; Ishii, I.; Tajima, K. Motion-blur-free high-speed video shooting using a resonant mirror. *Sensors,* **2017**, *17*, 2483.

[16] Yang, H.; Gu, Q.; Aoyama, T.; Takaki, T.; Ishii, I. Dynamics-based stereo visual inspection using multidimensional modal analysis. *IEEE Sensors J.* **2013**, *13*, 4831–4843.

[17] Aoyama, T.; Li, L.; Jiang, M.; Inoue, K.; Takaki, T.; Ishii, I.; Yang, H.; Umemoto, C.; Matsuda, H.; Chikaraishi, M.; Fujiwara, A. Vibration sensing of a bridge model using a multithread active vision system. *IEEE/ASME Transactions on Mechatronics,* **2017**, *PP*.

[18] Oku, H.; Ishii, I.; Ishikawa, M. Tracking a protozoon using high-speed visual feedback. In Proceedings of the IEEE Conference on Microtechnologies in Medicine and Biology, Lyon, France, 12-14 Oct. 2000; pp. 156–159.

[19] Sakuma, S.; Kuroda, K.; Tsai, C.; Fukui, W.; Arai, F.; Kaneko, M. Red blood cell fatigue evaluation based on the close-encountering point between extensibility and recoverability. *Lab Chip* **2014**, *14*, 1135–1141.

[20] Gu, Q.; Aoyama, T.; Takaki, T.; Ishii, I. Simultaneous vision-based shape and motion analysis of cells fast-flowing in a microchannel. *IEEE Trans. Autom. Sci. Eng.* **2015**, *12*, 204–215.

[21] Gu, Q.; Kawahara, T.; Aoyama, T.; Takaki, T.; Ishii, I.; Takemoto, A.; Sakamoto, N. LOC-based high-throughput cell morphology analysis system. *IEEE Trans. Autom. Sci. Eng.* **2015**, *12*, 1346–1356.

[22] Hornbeck, L. J. Digital light processing and MEMS: timely convergence for a bright future. Plenary Session, SPIE Micromachining and Microfabrication'95, Austin, Texas, October 24, 1995.

[23] Younse, J. M. Projection display systems based on the Digital Micromirror Device (DMD). In Proceedings of the SPIE Conference on Microelectronic Structures and Microelectromechanical Devices for Optical Processing and Multimedia Applications, Austin, Texas, Oct. 24, 1995,vol. 2641, pp. 64-75.

[24] Bimber, O.; Iwai, D.; Wetzstein, G.; Grundhöfer, A. The visual computing of projector-camera systems. In Proceedings of the Proc. SIGGRAPH '08 ACM, Los Angeles, California, August 11-15, 2008.

[25] Takei, J.; Kagami, S.; Hashimoto, K. 3,000-fps 3-D shape measurement using a high-speed camera-projector system. In Proceedings of the 2007 IEEE/RSJ International Conference on Intelligent Robots and Systems, San Diego, CA, USA, Oct 29-Nov 2, 2007.

[26] Kagami, S. High-speed vision systems and projectors for real-time perception of the world. In Proceedings of the 2010 IEEE Computer Society Conference on Computer Vision and Pattern Recognition - Workshops, San Francisco, CA, 2010; pp. 100-107.

[27] Gao, H.; Aoyama, T.; Takaki, T.; Ishii, I. A Self-Projected Light-Section Method for Fast Three-Dimensional Shape Inspection. *International Journal of Optomechatronics,* **2012**, *6*, pp.289-303.

[28] Liu, Y.; Gao, H.; Gu, Q.; Aoyama, T.; Takaki, T.; Ishii, I. High-frame-rate structured light 3-D vision for fast moving objects. *Journal of Robotics and Mechatronics,* **2014**, *26*, pp.311-320.

[29] Li, B.; An, Y.; Cappelleri, D.; Xu, J.; Zhang, S. High-accuracy, high-speed 3D structured light imaging techniques and potential applications to intelligent robotics. *Int J Intell Robot Appl,* **2017**, *1*, pp 86-103.

[30] Moreno, D.; Calakli, F.; Taubin, G. Unsynchronized structured light. *ACM Transactions on Graphics,* **2015**, *34*.

[31] Chen, J.; Yamamoto, T.; Aoyama, T.; Takaki, T.; Ishii, I. Simultaneous projection mapping using high-frame-rate depth vision. In Proceedings of the IEEE Int. Conf. on Robotics and Automation, Hong Kong, China, 31 May-7 June 2014; pp.4506-4511.

[32] Watanabe, Y.; Narita, G.; Tatsuno, S.; Yuasa, T.; Sumino, K.; Ishikawa, M. High-speed 8-bit image projector at 1,000 fps with 3 ms delay. In Proceedings of the International Display Workshops (IDW2015), Shiga, Japan, 11 Dec. 2015; pp.1064-1065.

[33] Narita, G.; Watanabe, Y.; Ishikawa, M. Dynamic projection mapping onto deforming non-rigid surface using deformable dot cluster marker. *IEEE Transactions on Visualization and Computer Graphics,* **2017**, *23*, pp. 1235-1248.

[34] Fleischmann, O.; Koch, R. Fast projector-camera calibration for interactive projection mapping. In Proceedings of the 23rd International Conference on Pattern Recognition (ICPR), Cancun, 2016; pp. 3798-3803.

[35] Cevik, T.; Yilmaz, S. An overview of visible light communication systems. *IJCNC,* **2015**, *7*, pp. 139-150.

[36] Bhalerao, M.; Sonavane, S.; Kumar, V. A survey of wireless communication using visible light. *International Journal of Advances in Engineering and Technology,* **2013**, *5*, pp. 188-197.

[37] Jovicic, A.; Li, J.; Richardson, T. Visible light communication: opportunities, challenges and the path to market. *IEEE Commun. Mag.,* **2013**, *51*, pp. 26–32.

[38] Fath, T.; Haas, H. Performance comparison of mimo techniques for optical wireless communications in indoor environments. *IEEE Trans. Commun,* **2013**, *6*, pp. 733–742.

[39] Kumar, N.; Lourenco, N. R. Led-based visible light communication system: A brief survey and investigation. *Journal of Engineering and Applied Sciences,* **2010**, *5*, pp. 296-307

[40] Komine, T.; Nakagawa, M. Fundamental analysis for visible-light communication system using LED lights. *IEEE Transactions on Consumer Electronics,* **2004**, *50*, pp. 100-107.

[41] Bui, T.; Kiravittaya, S.; Sripimanwat, K.; Nguyen, N. A comprehensive lighting configuration for efficient indoor visible light communication networks. *International Journal of Optics ,* **2016**, *2016*.

[42] Sindhubala, K.; Vijayalakshmi, B. Ecofriendly data transmission in visible light communication. In Proceedings of the Third International Conference on Computer, Communication, Control and Information Technology (C3IT) , Hooghly, 2015, pp. 1-4.

[43] Zafar, F.; Karunatilaka, D.; Parthiban, R. Dimming schemes for visible light communication: the state of research. *IEEE Wireless Communications,* **2015**, *22*, pp. 29-35.

[44] Rajagopal, S.; Roberts, R. D.; Lim, S. K. IEEE 802.15.7 visible light communication: modulation schemes and dimming support. *IEEE Communications Magazine,* **2012**, *50*, pp. 72-82.

[45] Takai, I.; Ito, S.; Yasutomi, K.; Kagawa, K.; Andoh, M.; Kawahito, S. LED and CMOS image sensor based optical wireless communication system for automotive applications. *IEEE Photonics Journal ,* **2013**, *5*, pp. 6801418-6801418.

[46] Takai, I.; Harada, T.; Andoh, M.; Yasutomi, K.; Kagawa, K.; Kawahito, S. Optical vehicle-to-vehicle communication system using LED transmitter and camera receiver. *IEEE Photonics Journal ,* **2014**, *6*, pp. 1-14.

[47] Kasashima, T.; Yamazato, T.; Okada, H.; Fujii, T.; Yendo, T.; Arai, S. Interpixel interference cancellation method for road-to-vehicle visible light communication. In Proceedings of the IEEE 5th Int. Symp. Wireless Veh. Commun., Dresden, Jun. 2013; pp. 1–5.

[48] Chinthaka, H.; Premachandra, N.; Yendo, T.; Yamasato, T.; Fujii, T.; Tanimoto, M.; Kimura, Y. Detection of LED traffic light by image processing for visible light communication system. In Proceedings of the 2009 IEEE Intelligent Vehicles Symposium, Xi’an, 2009; pp. 179-184.

[49] Yamazato, T.; Takai, I.; Okada, H.; Fujii, T.; Yendo, T.; Arai, S.; Andoh, M.; Harada, T.; Yasutomi, K.; Kagawa, K.; Kawahito, S. Image-sensor-based visible light communication for automotive applications. *IEEE Commun. Mag.,* **2014**, *52*, pp. 88–97.

[50] Rajagopal, N.; Lazik, P.; Rowe, A. Visual light landmarks for mobile devices. In Proceedings of the 13th International Symposium on Information Processing in Sensor Networks,Berlin, Germany, 15–17 April 2014; pp. 249–260.

[51] Boubezari, R.; Le Minh, H.; Bouridane; Pham, A. Data detection for Smartphone visible light communications. In Proceedings of the 9th International Symposium on Communication Systems, Networks and Digital Signal Processing (CSNDSP), Manchester, UK, 23–25 July 2014; pp. 1034–1038.

[52] Corbellini, G.; Akşit, K.; Schmid, S.; Mangold, S.; Gross, T. Connecting networks of toys and smartphones with visible light communication. *Proc.IEEE Commun. Mag,* **2014**, *52*, pp. 72–78.

[53] Wang, M.; Wu, J.; Yu, W.; Wang, H.; Li, J.; Shi, J.; Luo, C. Efficient coding modulation and seamless rate adaptation for visible light communications. *IEEE Wireless Communications ,* **2015**, *22*, pp. 86-93.

[54] Li, T.; An, C.; Tian, Z.; Campbell, A.T.; Zhou, X. Human sensing using visible light communication. In Proceedings of the MobiCom'15, Paris, France, September 7–11, 2015.

[55] Danakis, C.; Afgani, M.; Povey, G.; Underwood, I.; Haas, H. Using a CMOS camera sensor for visible light communication. In Proceedings of the IEEE GlobecomWorkshops (GC Wkshps), Anaheim, CA, USA, 3–7 December 2012; pp. 1244–1248.

[56] Wang, J.; Kang, Z.; Zou, N. Research on indoor visible light communication system employing white LED lightings. In Proceedings of the IET International Conference on Communication Technology and Application (ICCTA 2011), Beijing, 2011, pp. 934-937.

[57] Bui, T. C.; Kiravittaya, S. Demonstration of using camera communication based infrared LED for uplink in indoor visible light communication. In Proceedings of the IEEE Sixth International Conference on Communications and Electronics (ICCE), Ha Long, 2016, pp. 71-76.

[58] Chow, C.; Chen, C.; Chen, S. Enhancement of signal performance in LED visible light communications using mobile phone camera. *IEEE Photonics Journal,* **2015**, *7*, pp. 1-7.

[59] Xu, Y.; Zhao, J.; Shi, J.; Chi, N. Reversed three-dimensional visible light indoor positioning utilizing annular receivers with multi-photodiodes. *Sensors,* **2016**, *16*.

[60] Kuo, Y.; Pannuto, P.; Hsiao, K.; Dutta, P. Luxapose: Indoor positioning with mobile phones and visible light. In Proceedings of the 20th Annual International Conference on Mobile Computing and Networking, Maui, HI, USA, 7–11 September 2014; pp. 447–458.

[61] Jerome, K.; Tony, V.; Vinayak, R.; Dhanaraj, K. J. Indoor navigation using visible light communication. In Proceedings of the 2014 Texas Instruments India Educators' Conference (TIIEC), Bangalore, 2014, pp. 46-52.

[62] Ganti, D.; Zhang, W.; Kavehrad, M. VLC-based indoor positioning system with tracking capability using Kalman and particle filters. In Proceedings of the 2014 IEEE International Conference on Consumer Electronics (ICCE), Las Vegas, NV, 2014, pp. 476-477.

[63] Do, T.; Yoo, M. An in-depth survey of visible light communication based positioning systems. *Sensors,* **2016**, *16*, pp. 678.

[64] Zhao, X.; Lin, J. Maximum likelihood estimation of vehicle position for outdoor image sensor-based visible light positioning system. *Optical Engineering,* **2016**, *55*.

[65] Do, T.; Yoo, M. Performance analysis of visible light communication using CMOS sensors. *Sensors,* **2016**, *16*, pp. 309.

[66] Nguyen, T.; Hong, C.H.; Le, N.T.; Jang, Y. M. High-speed asynchronous optical camera communication using LED and rolling shutter camera. In Proceedings of the Seventh International Conference on Ubiquitous and Future Networks (ICUFN), Sapporo, Japan, 7–10 July 2015; pp. 214–219.

[67] Liu, Y.F.; Chen, H.; Liang, K.J.; Hsu, C.; Chow, C.; Yeh, C. Visible light communication using receivers of camera image sensor and solar Cell. *IEEE Photonics Journal,* **2016**, *8*, pp. 1-7.

[68] Hao, T.; Zhou, R.; Xing, G. Cobra: Color barcode streaming for smartphone systems. In Proceedings of the MobiSys 2012, Low Wood Bay, Lake District, UK, June 2012; pp. 85-98.

[69] Hu, W.; Gu, H.; Pu, Q. Lightsync: Unsynchronized visual communication over screen-camera links. In Proceedings of the MobiCom 2013, Miami, USA, Sept. 2013; pp 15-26.

[70] Perli, S. D.; Ahmed, N.; Katabi, D. PixNet: LCD-Camera pairs as communication links. In Proceedings of the SIGCOMM '10, New Delhi, India, August 30-September 2, 2010.

[71] Gao, Z.; Zhai, G.; Wu, X.; Min, X.; Zhi, C. DLP based anti-piracy display system. In Proceedings of the IEEE VCIP'14, Valletta, Malta, Dec. 7 - Dec. 10, 2014.

[72] Dai, J.; Chung, R. Embedding imperceptible codes into video projection and applications in robotics. In Proceedings of the 2012 IEEE/RSJ International Conference on Intelligent Robots and Systems, Vilamoura, 2012; pp. 4399-4404.

[73] Zhang, B.; Ren, K.; Xing, G.; Fu, X.; Wang, C. SBVLC: Secure barcode-based visible light communication for smartphones. *IEEE Transactions on Mobile Computing,* **20160**, *15*, pp. 432-446.

[74] Wang, A,; Li, Z.; Peng, C,; Shen, G,; Fang, G.; Zeng, B. InFrame++: Achieve Simultaneous Screen-Human Viewing and Hidden Screen-Camera Communication.

In Proceedings of the 13th Annual International Conference on Mobile Systems, Applications, and Services (MobiSys '15). New York, NY, USA, 2015, pp. 181–195.

[75] Wang, A,; Peng, C,; Zhang, O,; Shen, G,; Zeng, B. InFrame: Multiflexing full-frame visible communication channel for humans and devices. In Proceedings of the HotNets-XIII Proceedings of the 13th ACM Workshop on Hot Topics in Networks, Los Angeles, CA, USA, October 27-28, 2014.

[76] Fujiyoshi, H.; Shimizu, S.; Nishi, T. Fast 3D Position Measurement with Two Unsynchronized Cameras. *In Proceedings of 2003 IEEE International Symposium on Computational Intelligence in Robotics and Automation,* Kobe, Japan, July 2003; pp. 1239–1244.

[77] El Asmi, C.; Roy, S. Fast Unsynchronized Unstructured Light. *In Proceedings of 2018 15th Conference on Computer and Robot Vision (CRV),* Toronto, ON, Canada, 2018; pp. 277-284.

[78] Tuytelaars, T.; Gool, L.V. Synchronizing Video Sequences. *In Proceedings of the 2004 IEEE Computer Society Conference on Computer Vision and Pattern Recognition,* Washington, DC, USA, 27 June–2 July 2004 2004; Volume 1, pp. 762–768.

[79] Wolf, L.; Zomet, A. Correspondence-Free Synchronization and Reconstruction in a Non-Rigid Scene. *In Proceedings of the Workshop on Vision and Modeling of Dynamic Scenes,* Copenhagen, Denmark, May 2002; pp. 1–19.

[80] Tresadern, P.; Reid, I. Synchronizing Image Sequences of Non-Rigid Objects. *In Proceedings of the British Machine Vision Conference,* Norwich, UK, 9–11 September 2003; Volume 2, pp. 629–638.

[81] Whitehead, A.; Laganiere, R.; Bose, P. Temporal Synchronization of Video Sequences in Theory and in Practice. *In Proceedings of the IEEE Workshop on Motion and Video Computing,* Breckenridge, CO, USA, 5–7 January 2005; pp. 132–137.

[82] Rai, P.K.; Tiwari, K.; Guha, P.; Mukerjee, A. A Cost-effective Multiple Camera Vision System Using FireWire Cameras and Software Synchronization. *In Proceedings of the 10th International Conference on High Performance Computing,* Hyderabad, India, 17–20 December 2003.

[83] Litos, G.; Zabulis, X.; Triantafyllidis, G. Synchronous Image Acquisition based on Network Synchronization. *In Proceedings of the Conference on Computer Vision and Pattern Recognition Workshop,* Washington, DC, USA, 17 June 2006; pp. 167–167.

[84] Cho H. Time Synchronization for Multi-hop Surveillance Camera Systems. *In Kyung CM. (eds) Theory and Applications of Smart Cameras. KAIST Research Series.* Springer, Dordrecht.

[85] Ansari, S.; Wadhwa, N.; Garg, R.; Chen, J. Wireless Software Synchronization of Multiple Distributed Cameras. *In 2019 IEEE International Conference on Computational Photography (ICCP),* Tokyo, Japan, 2019, pp. 1-9,

[86] Sivrikaya, F.; Yener, B. Time synchronization in sensor networks: A survey. *In IEEE Network,* July-Aug. 2004, vol. 18, no. 4, pp. 45-50.

[87] Hou, L.; Kagami, S.; Hashimoto, K. Illumination-Based Synchronization of High-Speed Vision Sensors. *Sensors,* **2010**, *10*, 5530-5547.

[88] Hornbeck, L. J. Digital light processing: A new MEMS-based display technology. Technical Digest of the IEEJ 14th Sensor Symposium, Kawasaki, Japan, 1996; pp. 297–304.

[89] Gove, R. J. DMD display systems: The impact of an all-digital display. In Proceedings of the Information Display International Symposium, 1994; pp. 1–12.

[90] Hornbeck, L. J. Digital light processing and MEMS: an overview. Digest IEEE/Leos 1996 Summer Topical Meeting. Advanced Applications of Lasers in Materials and Processing, Keystone, CO, USA, 1996, pp. 7-8.

[91] Wang, Z.; Bovik, A. C.; Simoncelli, E. P. Image quality assessment: from error visibility to structural similarity. *IEEE Trans. Image Processing,* **2004**, *13*, pp. 600-612.

[92] www.bigbuckbunny.org(c) copyright 2008, Blender Foundation.

Acknowledgment

Firstly, I would like to express my sincere gratitude to my advisor **Prof. Idaku Ishii**, for providing me an opportunity to join the Robotics laboratory, Hiroshima University and the continuous support of my Ph.D. study and related research, as well as for his patience, motivation, and immense knowledge. His advice helped me in all the time of research and writing of this thesis.

Furthermore, I would like to thank the rest of my thesis committee members, **Prof. Toru Yamamoto**, and **Prof. Takeshi Takaki**, for their perceptive comments and inspiration to widen my research from various perspectives. My sincere thanks also go to **Prof. Qingyi Gu**, **Dr. Sushil Raut**, and **Dr. Shimasaki Kohei**, who provided me an opportunity to join their team, and who gave access to the research facilities. Without their precious support, it would not be possible to conduct this research.

I would also like to thank the colleagues and friends in Hiroshima University, who help me in both my study and life, including **Ms. Yukari Kaneyuki** and **Ms. Michiko Kanzaki** (educational administrator), and **Ms. Rumi Horiuchi** (laboratory secretary) and many other dear staffs. With their presence, I had a wonderful time in Japan.

My deepest gratitude goes to my family members, my father, my mother, my wife and my son, for their kind love and encouragement, so I have a nice atmosphere to study well during my PhD study.

July, 2021

Atul Sharma